

SYNTHESIS AND REACTIVITY OF TWO-DIMENSIONAL MATERIALS: LAYERED  
TRANSITION METAL DICHALCOGENIDES AND TEMPLATED BISMUTH TUNGSTATE

by

TIMOTHY RAY POPE

(Under the Direction of Tina T. Salguero)

ABSTRACT

Nanosheets, highly ordered materials with thicknesses of a monolayer or few-layers and lateral dimensions in the micrometer range, can be made by either bottom up or top down approaches. In the bottom up approach, nanosheets are formed directly. Chapters II and III outline a bottom down approach to create the metal oxide bismuth tungstate ( $\text{Bi}_2\text{WO}_6$ ) using reactive nanosheet precursors that provide a templating effect to produce  $\text{Bi}_2\text{WO}_6$  nanosheets with lateral dimensions in the micrometer range. Alternatively, in the top down approach, large pristine crystals of a bulk material are reduced to nanosheets by delamination or exfoliation. This is the method of choice discussed in Chapter IV for transition metal dichalcogenides, whose van der Waals structure allows for easy separation into mono- or few-layer nanosheets. Chapter IV focuses on a top down approach for forming tantalum diselenide nanosheets, along with the material's structure, oxidation effects, characterization, and novel applications.

INDEX WORDS: nanosheets, two-dimensional materials, transition metal dichalcogenides, metal oxides, tantalum diselenide, bismuth tungstate

SYNTHESIS AND REACTIVITY OF TWO-DIMENSIONAL MATERIALS: LAYERED  
TRANSITION METAL DICHALCOGENIDES AND TEMPLATED BISMUTH TUNGSTATE

by

TIMOTHY RAY POPE

B.S., University of West Florida, 2010

A Dissertation Submitted to the Graduate Faculty of the University of Georgia in Partial  
Fulfillment of the Requirements for the Degree

DOCTOR OF PHILOSOPHY

ATHENS, GEORGIA

2015

© 2015

Timothy Ray Pope

All Rights Reserved

SYNTHESIS AND REACTIVITY OF TWO-DIMENSIONAL MATERIALS: LAYERED  
TRANSITION METAL DICHALCOGENIDES AND TEMPLATED BISMUTH TUNGSTATE

by

TIMOTHY RAY POPE

Major Professor: Tina T. Salguero

Committee: Jason Locklin

John Stickney

Electronic Version Approved:

Suzanna Barbour

Dean of the Graduate School

The University of Georgia

August 2015

## DEDICATION

For my wonderful wife and family.

## ACKNOWLEDGEMENTS

I would like to acknowledge all of my fellow graduate students who helped me throughout my graduate years. Dr. Chris Barrett taught me a lot about nanomaterials and microscopy during my first two years. Melissa Lassig, Greg Neher, and Richard Weimar were excellent coworkers that aided in the projects discussed in this thesis. Darrah Johnson-McDaniel helped me immensely with presentations and writing. Matt Davidson and Dan Sexton joined the Salguero lab together with me and were of great help in the early years of the lab. I'd also like to thank Roshini Ramachandran, Matt Bloodgood, and Asma Sharafi for their fruitful discussions and help in the lab.

I would also like to thank my committee members, Professor John Stickney and Professor Jason Locklin, for their assistance. Finally, I am thankful for my research advisor Professor Tina Salguero for her mentorship and guidance throughout my graduate career.

## TABLE OF CONTENTS

	Page
<b>ACKNOWLEDGEMENTS</b>	<b>v</b>
<b>CHAPTERS</b>	
<b>1 INTRODUCTION AND LITERATURE REVIEW</b>	<b>1</b>
Nanosheets	1
Metal Oxide Nanosheets	3
Transition Metal Dichalcogenides	8
Research Goals	14
References	17
<b>2 CHROMISM OF Bi<sub>2</sub>WO<sub>6</sub> IN SINGLE CRYSTAL AND NANOSHEET FORMS</b>	<b>23</b>
Abstract	24
Introduction	25
Results and Discussion	27
Conclusions	40
Experimental	41
References	43
<b>3 BISMUTH METAL OXIDE NANOSHEETS FROM A BISMUTH BORATE NANOSHEET TEMPLATE</b>	<b>47</b>
Abstract	48
Introduction	49

Results and Discussion	52
Conclusions	68
References	69
<b>4 NANOSCALE TRANSITION METAL DICHALCOGENIDES: FORMATION AND APPLICATIONS OF TANTALUM DISELENIDE</b>	<b>72</b>
Abstract	73
Introduction	74
Results and Discussion	79
Nanoscale Properties and Electrical Devices	97
Conclusions	102
References	105
<b>5 CONCLUSIONS</b>	<b>111</b>
Conclusions	112
References	117

## CHAPTER 1

### INTRODUCTION AND LITERATURE REVIEW

#### **Nanosheets**

In 2010 the Nobel Prize in Physics was given to Andre Geim and Konstantin Novoselov for the discovery of the two-dimensional material graphene. Since then, research into other two-dimensional materials has greatly expanded. Highly ordered films with thicknesses of a single monolayer to a few layers and lateral dimensions reaching tens of micrometers are called nanosheets. Because of the high atomic order, nanosheets can be considered crystalline materials. Also, nanosheets can be thought of as two dimensional structures due to their anisotropic nature thus electron motion in these materials is restricted to the nanosheet plane. Moreover, it is possible to use solution-based methods to isolate nanosheets as free standing structures which do not need a substrate to exist. Inherently, nanosheets have large surface areas, leading to numerous active sites for catalysis or energy storage.<sup>1, 2</sup> When these materials are constrained to two dimensions, exotic condensed matter phenomena can arise. In some two dimensional materials, electrons and their corresponding holes are confined to a space similar in size to the exciton Bohr radius, which generates quantum confinement effects as seen in some materials where the bandgap increases as the physical dimensions of the nanostructure decrease.<sup>3</sup>

In particular, graphene (the nanosheet form of a two-dimensional monolayer of conjugated carbon atoms) shows vastly different electronic behavior than its bulk counterpart, graphite.<sup>4, 5</sup> For instance, graphene has a remarkably high electron mobility where electrons can travel micrometers

without scattering<sup>6</sup> and also displays a strong room temperature quantum Hall effect.<sup>7</sup> Graphene is often obtained from bulk by the Scotch tape method, where adhesive tape is used to peel graphite into thin flakes,<sup>8</sup> but can also be obtained through solution exfoliation methods using ultrasonication or high-shear mixing.<sup>9,10</sup>

Graphene is a zero-bandgap semiconductor, which inhibits its potential in switching applications. Bandgaps can be artificially engineered by functionalizing the graphene surface or forming nanostructures,<sup>11,12</sup> but such methods tend to limit electron mobility. Alternative layered van der Waals materials, such as transition metal dichalcogenides, have bandgaps of 1–2 eV and favorable electronic properties that allow their application in a variety of electronic devices.<sup>13</sup> Interestingly, transition metal dichalcogenides are transformed from indirect to direct-bandgap semiconductors when reduced to the nanosheet-regime.<sup>14</sup> Furthermore, metal oxide nanosheets are often light sensitive, opening up applications in photocatalysis and optoelectronics, and can have a wide variety of bandgaps.<sup>1,15</sup> For example, tantalum- and titanium-based metal oxides often have large bandgaps of 3–5 eV.<sup>3</sup> Metal oxides are a large class of materials that encompass a wide variety of properties due to the diverse chemical compositions and crystal structures that are possible.<sup>1,3,16</sup>

Additionally, inorganic nanosheets provide high chemical and thermal stability over carbon nanosheets.<sup>1</sup> Some layered inorganic materials can be converted to nanosheet form through exfoliation into few-layers or down to a monolayer in a similar manner to graphene, as shown in Figure 1.1. Other layered inorganic materials are not so easily separated into monolayers because the layers are interspersed by ion layers or held together with van der Waals forces. Therefore, “bottom up” approaches must be developed to produce nanosheets without first starting with the bulk material.

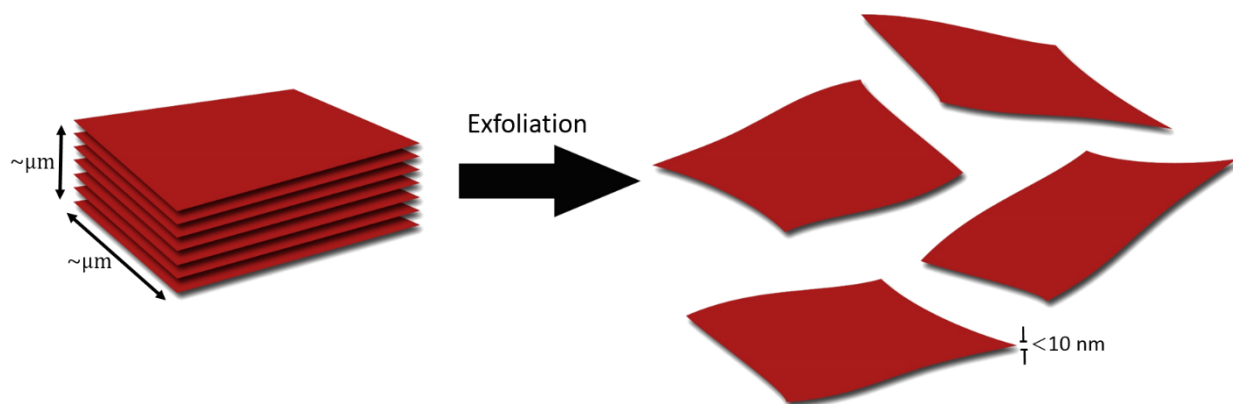


**Figure 1.1.** General scheme for exfoliation of a bulk sample of a layered material into monolayer nanosheets. In ion-interspaced layered metal oxides, the bulk material is swelled through ion exchange which induces spontaneous exfoliation. In transition metal dichalcogenides, exfoliation methods disrupt the van der Waals forces that hold separate  $\text{MX}_2$  layers together to result in free-standing, isolable nanosheets.

Transition metal dichalcogenides can successfully be delaminated or exfoliated into nanosheets, and a number of reports have examined the preparation and unique electronic properties of transition metal dichalcogenides.<sup>13, 17-20</sup> The preparation of metal oxide nanosheets is a much more recent research topic than the preparation of transition metal dichalcogenide nanosheets.<sup>15, 21</sup> Thus far, a large portion of the research into metal oxide nanosheets is focused on synthesis of nanosheets and thin film preparation.

### Metal Oxide Nanosheets

Metal oxide nanosheets comprise a class of ceramics with widely varying properties that can also be exploited on the nanoscale. For example, bismuth tungstate ( $\text{Bi}_2\text{WO}_6$ ), a common metal oxide and the subject of Chapters II and III, is a ferroelectric and piezoelectric material, possesses catalytic behavior, conducts oxide anions, and displays a nonlinear dielectric susceptibility.<sup>22-26</sup>

Metal oxide nanosheets have been investigated as potential photodegradation catalysts, specifically for organic pollutants, and water splitting catalysts. For example, nanosized  $\text{Bi}_2\text{WO}_6$

catalyzes the photodegradation of chloroform and acetaldehyde as well as Rhodamine B, while avoiding the carcinogenic aromatic amines produced upon the natural degradation of Rhodamine B.<sup>26, 27</sup>

Metal oxides can also have interesting electronic properties. Barium titanate is one of the most widely used dielectric ceramics and has photorefractive and piezoelectric properties. In fact, it was the first piezoceramic used in large scale applications. Notably, barium titanate can be used as a storage material in capacitors.<sup>28</sup> Commercial use of barium titanate has been replaced by a similar ceramic, lead zirconate titanate (PZT). In commercial applications, the piezoelectric properties of PZT are tuned through doping with acceptors such as  $\text{Fe}^{3+}$  to create “hard PZT” or donors such as  $\text{La}^{3+}$  and  $\text{Nb}^{5+}$  to create “soft PZT”.<sup>29</sup> As a lead-free alternative, bismuth tungstate ( $\text{Bi}_2\text{WO}_6$ ) is a piezoelectric material that maintains piezoelectricity at temperatures approaching  $400\text{ }^\circ\text{C}$ .<sup>24</sup>

Metal oxides can have a variety of crystal structures. Barium titanate and PZT are both perovskites with a general formula of  $^{\text{XII}}\text{A}^{2+}\text{VI}^{\text{B}^{4+}}\text{X}^{2-}_3$ , or more simply  $\text{ABO}_3$  for the oxide form. Layered perovskites exist in one of three distinct phases: the Aurivillius phase, the Dion-Jacobson phase, or the Ruddlesden-Popper phase. The Aurivillius and Ruddlesden-Popper phases, in particular, are most often studied for their dielectric and ferroelectric properties. Bismuth metal oxides are perovskite-like materials which can have Aurivillius or Sillén phases. The Aurivillius phase consists of alternating layers of  $(\text{Bi}_2\text{O}_2)^{2+}$  and perovskite-like  $(\text{A}_{n-1}\text{B}_n\text{O}_{3n+1})^{2-}$ , where  $n$  corresponds to the number of corner-shared octahedra in the perovskite-like blocks. In fact,  $\text{Bi}_2\text{WO}_6$  is the simplest Aurivillius form where  $n = 1$ . The Sillén phase has a similar structure,  $[\text{Bi}_2\text{O}_2][\text{X}_m]$  ( $m = 1-3$ ), which also contains  $(\text{Bi}_2\text{O}_2)^{2+}$  layers. Figure 1.2 shows the layered Aurivillius phase of  $\text{Bi}_2\text{WO}_6$ , which consists of  $\text{WO}_4^{2-}$  layers alternating with  $[\text{Bi}_2\text{O}_2]^{2+}$  layers.

Aurivillius phase metal oxides are also good conductors of oxide ions and have use in fuel cells, oxygen pumps, and other applications that require the transport of oxygen.<sup>30</sup>

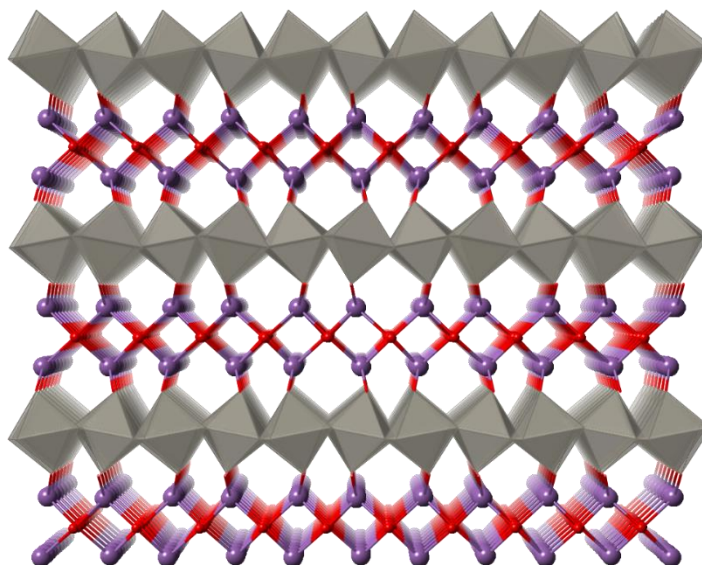


**Figure 1.2.** Crystal structure of the Aurivillius phase of Bi<sub>2</sub>WO<sub>6</sub>. The red atoms represent oxygen, the purple atoms represent boron, and the gray octahedra represent WO<sub>6</sub>.

It would be useful to have a standard method to easily produce nanosheets of bismuth tungstate in order to study the optical, piezoelectric, and other unique properties of such materials on the nanoscale. Other layered metal oxide materials with similar properties can be reduced to the nanoscale through a variety of methods. For example, the exfoliation of bulk layered metal oxides is typically induced in a multistep process through ion exchange and the intercalation of bulky organic ions. In the general process, the bulk metal oxide is submitted to an ion exchange reaction in an electrolyte solution, which causes osmotic swelling between the weakly associated layers that leads to exfoliation.<sup>31</sup> Compatible electrolyte solutions often consist of amine or ammonium ions. For example, Sasaki et al. used an aqueous solution of

tetrabutylammonium hydroxide to exfoliate smectite-like protonic titanate into nanosheets.<sup>32</sup> The intercalation and osmotic swelling phase sometimes produces structures that are swelled to 100 times their original size.<sup>33</sup> Often, exfoliation of the swollen material will be aided by ultrasonication or mechanical shaking. Exfoliation produces stable nanosheet dispersions that can be utilized in solution deposition methods. The lateral dimensions of the nanosheets depend in part on the bulk crystallite size and also on exfoliation conditions, as excessive agitation can cause fragmentation of the ceramic nanosheets.

These methods typically produce nanosheets with thicknesses of 0.5–4 nm, often to a single monolayer. However, the different methods produce a variety of lateral sizes. Exfoliation aided by mechanical shaking can fracture the nanosheets, resulting in nanosheets with lateral dimensions in the sub-micrometer range. Gentle shaking, such as by hand, can prevent such fracture and produce nanosheets with lateral dimensions of several tens of micrometers.<sup>3</sup> The concentration and type of electrolyte ions can also influence the final lateral dimensions of the metal oxide nanosheets.<sup>34</sup>

In order for this method of exfoliation to work, some metal oxides must first be altered before intercalation can occur. Layered perovskites contain interlayer cations that can be readily exchanged with protons through ion exchange reactions.<sup>35</sup> The resulting protonated solids can then react with organic bases to form swelled intercalation compounds. Fukuda et al. exfoliated a layered cesium tungstate with the formula  $\text{Cs}_{6+x}\text{W}_{11}\text{O}_{36}$  (shown in Figure 1.3) into  $\text{Cs}_4\text{W}_{11}\text{O}_{36}^{2-}$  nanosheets by exchanging interlayer cesium ions with protons, then intercalating quaternary ammonium ions into the structure and shaking intermittently for 10 days.<sup>36</sup>

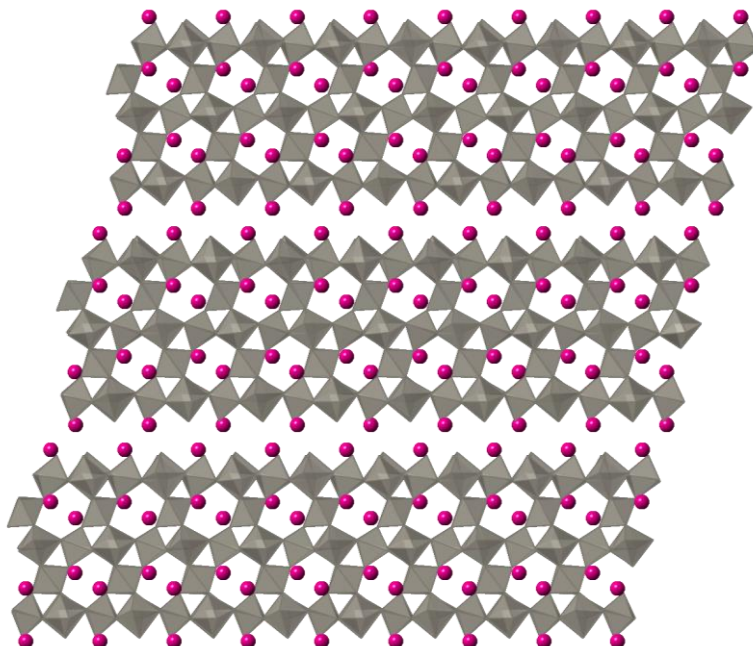


**Figure 1.3.** Crystal structure of  $\text{Cs}_{6+x}\text{W}_{11}\text{O}_{36}$  (shown down the b-axis), which can be exfoliated along the cesium ion layer plane by ion exchange.

Other methods for exfoliation have also been discussed in the literature. Sasaki and Kim et al. exfoliated Aurivillius-type bismuth titanate nanoplatelets by lithium ion intercalation and subsequent reaction with water.<sup>37</sup> In addition, exfoliated sheets can be restacked to form interesting structures. Fang et al. used layer-by-layer deposition to form high quality multilayer films of exfoliated niobate and titanoniobate (both perovskite-type oxides).<sup>38</sup>

Nanoscale metal oxides have also been synthesized directly. Zhang et al. produced square nanoplates of  $\text{Bi}_2\text{WO}_6$  with maximum lengths of 200 nm by hydrothermal treatment at temperatures above 160 °C.<sup>39</sup> Amano et al. produced  $\text{Bi}_2\text{WO}_6$  with a “flake-ball” morphology composed of rectangular platelets by hydrothermal synthesis with excess tungstate precursor under acidic conditions.<sup>40</sup> “Flower-like”  $\text{Bi}_2\text{WO}_6$  morphologies of aggregated nanoplatelets have also been produced by hydrothermal synthesis under acidic conditions.<sup>41</sup> Sun et al. synthesized oriented

$\text{Bi}_2\text{WO}_6$  with by lateral dimensions of  $\sim 100$  nm by slightly increasing the pH of the hydrothermal solution to 4.8.<sup>42</sup>

In Chapters II and III, a nanosheet precursor is used in the hydrothermal synthesis of nanoscale bismuth tungstate ( $\text{Bi}_2\text{WO}_6$ ). The mechanism behind such templating effect of a cesium tungstate nanosheet precursor is discussed in detail in Chapter II, while Chapter III discusses using a bismuth hydroxyl borate nanosheet template.

### **Transition Metal Dichalcogenides**

Transition metal dichalcogenides are another interesting class of inorganic materials that can be reduced to nanosheets. These materials have the general structural formula of  $\text{MX}_2$ , where M is a transition metal in group 4-10 and X is a chalcogenide (S, Se, or Te).  $\text{MX}_2$  materials containing group 4-7 transition metals have a layered, two-dimensional structure similar to graphene. Each  $\text{MX}_2$  layer has a sandwich structure with the transition metal covalently bound to an upper and lower layer of chalcogenide. The metal center has either octahedral or trigonal prismatic coordination geometry. These X-M-X layer typically has a thickness between 6 and 7 Å and is held together by van der Waals forces, making exfoliation into two-dimensional nanosheets relatively easy.

One major difference between  $\text{MX}_2$  materials and graphene is that they can occur in different crystal polymorphs, or more specifically polytypes (Figure 1.4).  $\text{MX}_2$  materials can be synthesized in a variety of polytypes depending on the reaction conditions. The most common polytypes are  $1T$ ,  $2H$ , and  $3R$ . In this nomenclature, the number denotes the total number of X-M-X layers in the unit cell and the letter represents the overall lattice structure. For example, in the  $3R$  polytype there are three  $\text{MX}_2$  layers per unit cell and has a rhombohedral crystal structure. The  $1T$

polytype has octahedral coordination about the metal center, while the  $2H$  and  $3R$  polytypes have trigonal prismatic coordination about the metal center.

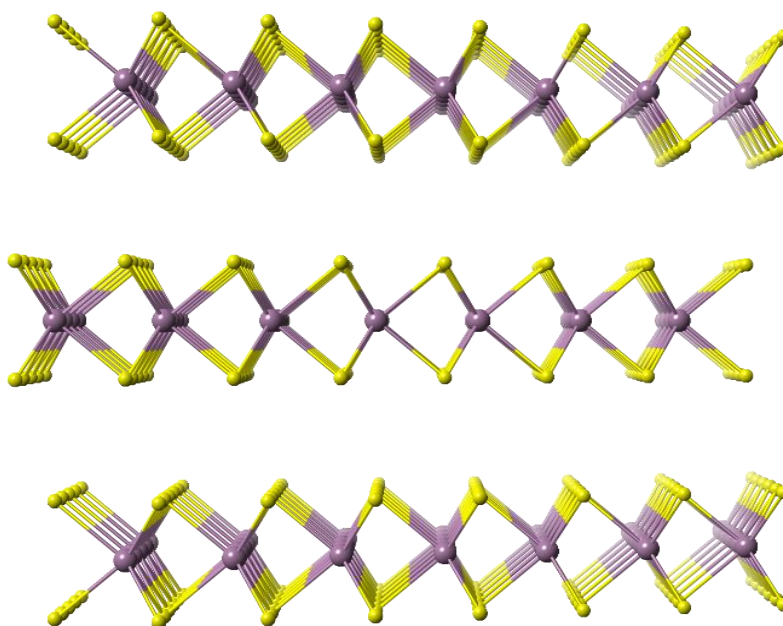


**Figure 1.4.** Structural representation of  $2H$ - $\text{MoS}_2$  as viewed down the  $a$ -axis, showing the layered van der Waals structure and trigonal prismatic coordination about the metal center.

The only  $\text{MX}_2$  material used industrially, thus far, is  $\text{MoS}_2$ . Bulk  $\text{MoS}_2$  powders have served as a dry lubricant and also a catalyst for hydrodesulfurization, where organosulfur functionalities are removed from organic materials, notably petroleum streams. Recently, however, researchers have discovered that  $\text{MX}_2$  have novel electronic properties when reduced into nanosheets. These properties largely depend on the composition of the  $\text{MX}_2$ . For example,  $\text{HfS}_2$  is an insulator,  $\text{MoS}_2$  and  $\text{WS}_2$  are semiconductors,  $\text{TiSe}_2$  is a semi-metal with charge density wave (CDW) properties, and  $\text{NbS}_2$  is metallic and superconducting (see Table 1.1 for a summary of some  $\text{MX}_2$  materials and their properties).<sup>43</sup> The metal center plays a more significant role than the chalcogenide for determining the electronic properties of the material, depending on the filling

of the non-bonding d orbital of the metal; however, the structure, composition, and dimensionality all play a role in controlling the bandgap energy and carrier type.<sup>43</sup>

**Table 1.1. Electronic Properties of Layered Transition Metal Dichalcogenides Varying with Chalcogenide and Metal**

Chalcogenide	Metallic	Semiconducting	CDW	Superconducting
S <sub>2</sub>	Nb, Ta	Ti, Mo, W	Nb, Ta	Nb, Ta
Se <sub>2</sub>	Nb, Ta	Mo, W	Ti, Nb, Ta	Nb, Ta
Te <sub>2</sub>	Nb, Ta	Mo, W	Ti	—

Some bulk MX<sub>2</sub> have interesting electronic phenomena, such as charge density waves and Mott transitions (metal to non-metal transitions), which are preserved when reduced to two dimensions.<sup>44, 45</sup> However, not all electronic properties are preserved upon reduction from bulk to two dimensions. For example, bulk MoS<sub>2</sub> is an indirect-gap semiconductor, while monolayer MoS<sub>2</sub> is a direct-gap semiconductor.<sup>43</sup> This transition leads to enhanced photoluminescence in MoS<sub>2</sub> monolayers as compared with its bulk or multilayer counterpart.<sup>14, 46</sup>

When these materials are restricted to the two-dimensional nanoscale regime, quantum confinement effects give rise to a variety of additional electronic phenomena, such as on/off switching, ultrahigh current density, and temperature-dependent conductivity.<sup>47-49</sup> By harnessing this phenomena, MX<sub>2</sub> nanosheets can be used in field effect transistors as logic switches.<sup>17, 50</sup> Another unique application is the potential for “valleytronics” in devices made from two-dimensional MoS<sub>2</sub>.<sup>51, 52</sup> When a material has two or more minima in the conduction band, it becomes possible to confine charges to a specific minimum, or valley. In this way, traditional computing information (zeros and ones) could be transferred based on the momentum of electrons traveling through the crystal lattice.

Few-layer  $\text{MX}_2$  nanosheets can be synthesized directly using reactive precursors via the “bottom up” approach of chemical vapor deposition (CVD). CVD includes a variety of chemical methods, but as it relates to  $\text{MX}_2$  the most noteworthy methods are (1) a vapor-phase reaction of an elemental transition metal and chalcogenide that deposits on a substrate, (2) sulfurization on a metal film (this method produces  $\text{MS}_2$ ), and (3) sulfurization of a metal oxide (again, producing  $\text{MS}_2$ ).<sup>43</sup> For example, Liu et al. successfully grew three-layer  $\text{MoS}_2$  by heating a thin film of ammonium thiomolybdate to 500 °C in an argon/hydrogen atmosphere.<sup>53</sup> A second heating to 1000 °C in a sulfur atmosphere enhanced the film crystallinity so that electronic applications could be pursued. Zhan et al. followed a similar strategy to create monolayer  $\text{MoS}_2$  films by heating thin molybdenum films in the presence of elemental sulfur.<sup>54</sup> Wafer-scale few-layer  $\text{MoS}_2$  films have been fabricated by sulfurization of molybdenum oxide thin films.<sup>53</sup> Though initial success has been achieved with  $\text{MoS}_2$ , there have been some reports of other  $\text{MX}_2$  nanosheets grown by CVD, such as  $\text{MoSe}_2$ ,  $\text{WS}_2$ ,  $\text{WSe}_2$ , and  $\text{TiS}_2$ .<sup>55-57</sup>

Another bottom up approach to nanoscale  $\text{MX}_2$  is using solvothermal synthesis. Yan et al. synthesized  $\text{MoS}_2$  clusters of nanoplatelets by dispersing ammonium thiomolybdate in a 2:1 mixture of *N,N*-dimethylformamide and water and heating in an autoclave at 210 °C for 18 h.<sup>58</sup> The platelets had lateral dimensions in the 200–300 nm range and consisted of 7–10  $\text{MoS}_2$  layers.

Alternatively, a top down approach can be used to obtain nanosheets by first synthesizing large single crystals of  $\text{MX}_2$ , which can then be delaminated or exfoliated into nanosheets. Synthesizing large, pristine single crystals of  $\text{MX}_2$ , which are ideal for delamination and exfoliation, can be obtained by a multistep process involving solid state synthesis and chemical vapor transport (CVT). First, a microcrystalline  $\text{MX}_2$  precursor is prepared by heating stoichiometric amounts of elemental transition metal and chalcogenide at high temperatures.<sup>59</sup>

Then using CVT large pristine single crystals with lateral dimensions up to a millimeter are produced from the precursor, however the growth process can require several weeks of transport.

Bulk  $\text{MX}_2$  samples can be exfoliated (or delaminated) into mono- or few-layers using a variety of methods. The simplest among them being the Scotch tape method, where adhesive tape is used to delaminate the bulk material into thin flakes, which was principally used to obtain graphene.<sup>8</sup> However, this method is not easily scaled to large batches and is also unsuitable for obtaining large nanosheets. Therefore, alternative methods for obtaining nanosheets have been developed. A generalized scheme for exfoliation is presented in Figure 1.1. To exfoliate  $\text{MX}_2$  materials, the van der Waals forces holding the adjacent  $\text{MX}_2$  layers are overcome, which results in free-standing, isolable nanosheets. In some cases, nanosheets can have similar lateral dimensions to the source crystal. In general, these are solution-based methods that have the potential to be scaled to handle large quantities of material and result in stable dispersion of nanosheets for simple solution processing.

Because small molecules can be intercalated between the  $\text{MX}_2$  layers, organolithium compounds can be used to drive chemical exfoliation.<sup>60</sup> Upon exposure to *N*-butyllithium, the weakly bound  $\text{MX}_2$  layers are intercalated (or interdigitated) with lithium ions. Once lithiated, bath sonicating  $\text{LiMX}_2$  in water hastens the removal of the lithium ions from the interlayers; the reaction of lithium with water, to form lithium hydroxide and hydrogen gas, provides enough energy to overcome the weak interlayer van der Waals forces and exfoliates the material into an aqueous nanosheet dispersion.<sup>21</sup> Additionally, lithium ions can be used in electrochemical exfoliation methods. Here, electrochemistry is used to drive lithium ions from a lithium hexafluorophosphate electrolyte solution into  $\text{MX}_2$  layers simply by applying a negative potential to the material. As with the previously mentioned  $\text{LiMX}_2$  material, mild bath sonication in water then generates  $\text{MX}_2$

nanosheet exfoliation. Recently, electrochemical exfoliation has been used to exfoliate various  $\text{MX}_2$  materials, including  $\text{MoS}_2$ .<sup>61</sup> In addition, lithium intercalation can alter the polytype of the material. For example, when  $2H\text{-MoS}_2$  is intercalated with lithium, the structure transforms to the  $1T\text{-MoS}_2$  polytype.<sup>62</sup> However, different materials undergo different polytype transformations. In  $\text{TaS}_2$ , the opposite transition occurs:  $1T\text{-TaS}_2$  becomes  $2H\text{-TaS}_2$  upon lithium intercalation.<sup>63</sup>

Other small molecules, such as sodium naphthalenide, have also been used in intercalation methods to drive exfoliation.<sup>64</sup> In this recent method, hydrazine is intercalated into bulk  $\text{MX}_2$  crystals under hydrothermal conditions to expand the crystals by up to 100 times its original volume. Subsequently, sodium naphthalenide is intercalated between the  $\text{MX}_2$  layers in order to further expand the crystal lattice. Finally, the intercalated structure is sonicated in water at low power to fully exfoliate nanosheets into a nanosheet dispersion. This method has been shown to produce  $\text{MoS}_2$  nanosheets with surface areas up to  $400 \mu\text{m}^2$ .

$\text{MX}_2$  nanosheets can also be exfoliated without intercalation by ultrasonication in a coordinating solvent.<sup>65</sup> In this procedure, the bulk material is dispersed in a solvent with a surface energy similar to that of the material, such as *N*-methylpyrrolidone or *N*-vinylpyrrolidone then exposed to ultrasonication for at least 1 hour.<sup>66</sup> Conditions such as sonication time and material concentration must be optimized for each material in order to avoid fracturing the nanosheets. Any remaining bulk crystals can be isolated from solution by centrifugation at low rpm. After centrifugation, the supernatant contains a dispersion of nanosheets. This method produces nanosheets with large lateral dimensions sometimes reaching up to hundreds of nanometers. For example, O'Neill et al. have optimized the liquid exfoliation conditions for  $\text{MoS}_2$  to obtain nanosheets  $\sim 2 \mu\text{m}$  in lateral dimension by carefully controlling the sonication time.<sup>67</sup>

Recently, Paton et al. developed a high-throughput method for obtaining nanosheets using high-shear mixing.<sup>10</sup> Essentially, an industrial-sized blender was used to exfoliate a dispersion of layered material, either graphene or  $\text{MX}_2$ . In fact, a conventional kitchen blender was able to achieve exfoliation because of the high turbulent shear rates generated in localized regions near the rotating blades. Similar to samples prepared by sonication, the nanosheets produced by this method are of high quality. Chapter IV goes into further detail about the properties, synthesis, and applications of nanoscale  $\text{MX}_2$ , with a focus on tantalum diselenide ( $\text{TaSe}_2$ ). This material's synthesis, characterization, and exfoliation are discussed in further detail along with surface oxidation studies.

## **Research Goals**

The work presented in this dissertation aims to develop further insight into the synthesis and properties of two dimensional materials with a focus on a metal oxide, bismuth tungstate ( $\text{Bi}_2\text{WO}_6$ ), and a transition metal dichalcogenide, tantalum diselenide ( $\text{TaSe}_2$ ). Chapters II and III discuss the bottom up formation of  $\text{Bi}_2\text{WO}_6$  nanosheets by hydrothermal synthesis using reactive nanosheet templates. Chapter IV discusses the top down formation of  $\text{TaSe}_2$  nanosheets by forming large, pristine crystals of  $\text{TaSe}_2$  by chemical vapor transport (CVT) then delaminating the material into nanosheets. In addition, Chapter IV discusses properties, such as oxidation, and applications of  $\text{TaSe}_2$  nanosheets.

The hydrothermal synthesis of nanoscale  $\text{Bi}_2\text{WO}_6$  using soluble precursors results in a variety of nano-morphologies;<sup>40, 41, 68, 69</sup> however, soluble precursors do not produce  $\text{Bi}_2\text{WO}_6$  nanosheets. Therefore, we developed a method to use reactive nanosheet precursors which create a templating effect during the formation of  $\text{Bi}_2\text{WO}_6$  that results in nanosheet morphologies (see

Figure 1.5). Chapter II discusses the direct synthesis of  $\text{Bi}_2\text{WO}_6$  nanosheets using a nanosheet cesium tungstate precursor ( $\text{Cs}_4\text{W}_{11}\text{O}_{36}^{2-}$ ) which acts as a template for the growth of  $\text{Bi}_2\text{WO}_6$  nanosheets with thicknesses of 5–15 nm and lateral dimensions of 1–2  $\mu\text{m}$ .<sup>70</sup>  $\text{Bi}_2\text{WO}_6$  nanosheets displayed chromism upon UV irradiation and lithium ion intercalation; moreover, the UV-induced, reversible photochromism of dispersed  $\text{Bi}_2\text{WO}_6$  nanosheets was found to be dependent on the solvent.<sup>70</sup> Chapter III also discusses the direct synthesis of  $\text{Bi}_2\text{WO}_6$  nanosheets, this time using a nanosheet bismuth hydroxyl borate precursor ( $\text{Bi}_2\text{O}_2[\text{BO}_2(\text{OH})]$ ). When reacted with a soluble tungsten precursor,  $\text{Bi}_2\text{O}_2[\text{BO}_2(\text{OH})]$  produced aggregates of large nanoplatelets; however, when reacted with the same nanosheet cesium tungstate precursor as in Chapter II,  $\text{Bi}_2\text{O}_2[\text{BO}_2(\text{OH})]$  produced nanosheets with lateral dimensions in the micrometer range and thicknesses of 5–40 nm.

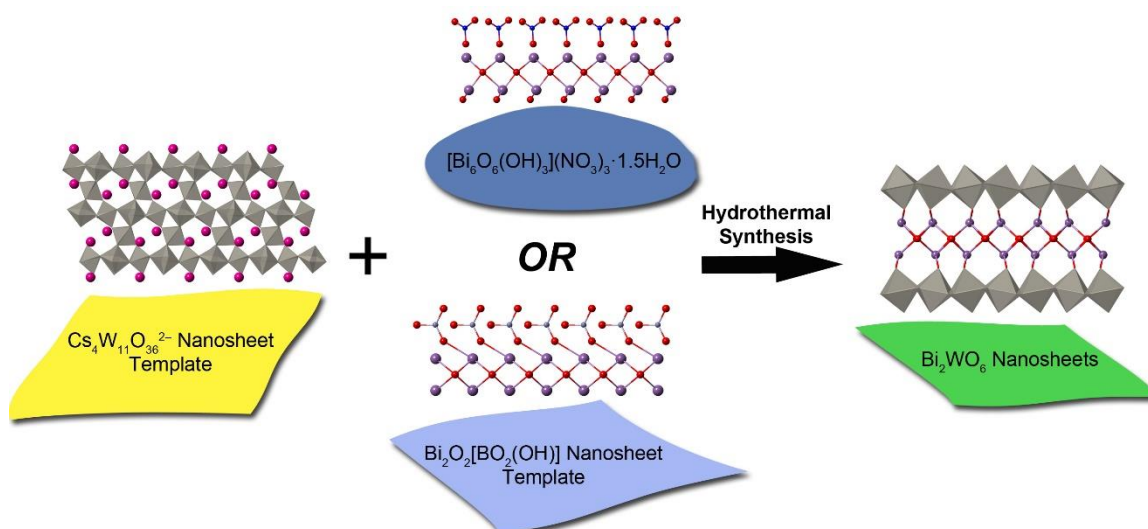


**Figure 1.5.** Schematic for the formation of  $\text{Bi}_2\text{WO}_6$  nanosheets using a templating effect, along with the crystal structures of the reactants and final product.

Alternatively, in the synthesis of  $\text{TaSe}_2$  nanosheets (see scheme in Figure 1.6), we are focused on gaining a further understanding of the synthesis, properties, and surface reactivity of the material to better create pristine nanosheets for device implementation. Chapter IV discusses the synthesis of  $\text{TaSe}_2$  nanosheets in several different polytypes ( $1T$ ,  $2H$ , and  $3R$ ). Bulk  $\text{TaSe}_2$  is

synthesized by chemical vapor transport (CVT), where the CVT temperature and cooling rate dictates the polytype produced. TaSe<sub>2</sub> nanosheets are formed by solution exfoliation of bulk TaSe<sub>2</sub> of the same polytype. Bulk 1*T*- and 2*H*,3*R*-TaSe<sub>2</sub> was found to be susceptible to surface oxidation at elevated temperatures. In addition, if 1*T*-TaSe<sub>2</sub> is stored under ambient atmospheric conditions for several months, the surface layer is transformed to 2*H*-TaSe<sub>2</sub>. Both of these phenomena are confined to the surface and can be removed by delaminating the top layer using the Scotch tape method. Finally, the material produced in our lab was used by collaborators at the University of California, Riverside, who developed a technique to measure sheet thickness using Raman spectroscopy, studied the transition from commensurate to incommensurate charge density wave, and created all-metallic transistors.<sup>17-19</sup>

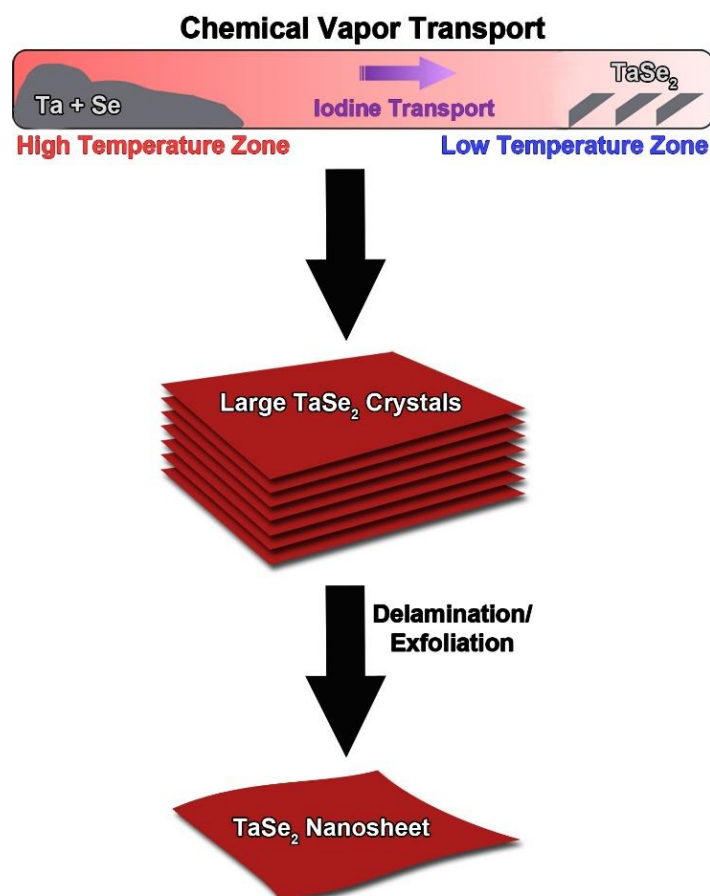


**Figure 1.6.** Schematic for the formation of TaSe<sub>2</sub> nanosheets by first forming large TaSe<sub>2</sub> crystals by chemical vapor transport then delaminating or exfoliating the bulk crystals into nanosheets.

## References

1. Osada, M.; Sasaki, T. *Adv. Mater.* **2012**, 24, (2), 210-228.
2. Chhowalla, M.; Shin, H. S.; Eda, G.; Li, L. J.; Loh, K. P.; Zhang, H. *Nat. Chem.* **2013**, 5, (4), 263.
3. Ma, R.; Sasaki, T. *Adv. Mater.* **2010**, 22, (45), 5082-5104.
4. Novoselov, K. S.; Geim, A. K.; Morozov, S. V.; Jiang, D.; Zhang, Y.; Dubonos, S. V.; Grigorieva, I. V.; Firsov, A. A. *Science* **2004**, 306, (5696), 666-669.
5. Geim, A. K. *Science* **2009**, 324, (5934), 1530-1534.
6. Geim, A. K.; Novoselov, K. S. *Nature Materials* **2007**, 6, (3), 183-191.
7. Novoselov, K. S.; Jiang, Z.; Zhang, Y.; Morozov, S. V.; Stormer, H. L.; Zeitler, U.; Maan, J. C.; Boebinger, G. S.; Kim, P.; Geim, A. K. *Science* **2007**, 315, (5817), 1379-1379.
8. Novoselov, K. S.; Jiang, D.; Schedin, F.; Booth, T. J.; Khotkevich, V. V.; Morozov, S. V.; Geim, A. K. *Proc. Natl. Acad. Sci. U.S.A.* **2005**, 102, 10451.
9. Coleman, J. N. *Acc. Chem. Res.* **2013**, 46, (1), 14-22.
10. Paton, K. R.; Varrla, E.; Backes, C.; Smith, R. J.; Khan, U.; O'Neill, A.; Boland, C.; Lotya, M.; Istrate, O. M.; King, P.; Higgins, T.; Barwich, S.; May, P.; Puczkarski, P.; Ahmed, I.; Moebius, M.; Pettersson, H.; Long, E.; Coelho, J.; O'Brien, S. E.; McGuire, E. K.; Sanchez, B. M.; Duesberg, G. S.; McEvoy, N.; Pennycook, T. J.; Downing, C.; Crossley, A.; Nicolosi, V.; Coleman, J. N. *Nat Mater* **2014**.
11. Balog, R.; Jorgensen, B.; Nilsson, L.; Andersen, M.; Rienks, E.; Bianchi, M.; Fanetti, M.; Laegsgaard, E.; Baraldi, A.; Lizzit, S.; Sljivancanin, Z.; Besenbacher, F.; Hammer, B.; Pedersen, T. G.; Hofmann, P.; Hornekaer, L. *Nat Mater* **2010**, 9, (4), 315-319.

12. Ming-Wei, L.; Cheng, L.; Yiyang, Z.; Hyeun Joong, Y.; Mark Ming-Cheng, C.; Luis, A. A.; Nicholas, K.; Noppi, W.; Zhixian, Z. *Nanotechnology* **2011**, 22, (26), 265201.
13. Wang, Q. H.; Kalantar-Zadeh, K.; Kis, A.; Coleman, J. N.; Strano, M. S. *Nature Nanotechnology* **2012**, 7, (11), 699-712.
14. Mak, K. F.; Lee, C.; Hone, J.; Shan, J.; Heinz, T. F. *Phys. Rev. Lett.* **2010**, 105, (13).
15. Osada, M.; Sasaki, T. *J. Mater. Chem.* **2009**, 19, 2503.
16. Osada, M.; Sasaki, T. *Adv. Mater.* **2012**, 24, 210.
17. Renteria, J.; Samnakay, R.; Jiang, C.; Pope, T. R.; Goli, P.; Yan, Z.; Wickramaratne, D.; Salguero, T. T.; Khitun, A. G.; Lake, R. K.; Balandin, A. A. *J. Appl. Phys.* **2014**, 115, (3), 034305.
18. Yan, Z.; Jiang, C.; Pope, T. R.; Tsang, C. F.; Stickney, J. L.; Goli, P.; Renteria, J.; Salguero, T. T.; Balandin, A. A. *J. Appl. Phys.* **2013**, 114, (20), 204301.
19. Samnakay, R.; Wickramaratne, D.; Pope, T. R.; Lake, R. K.; Salguero, T. T.; Balandin, A. A. *Nano Lett.* **2015**.
20. Lembke, D.; Bertolazzi, S.; Kis, A. *Acc. Chem. Res.* **2015**, 48, (1), 100-110.
21. Joensen, P.; Frindt, R. F.; Morrison, S. R. *Mater. Res. Bull.* **1986**, 21, (4), 457-461.
22. Zhang, L.; Zhu, Y. *Catalysis Science & Technology* **2012**, 2, (4), 694-706.
23. Noguchi, Y.; Miyayama, M., Defect Control and Properties in Bismuth Layer Structured Ferroelectric Single Crystals. In *Lead-Free Piezoelectrics*, Priya, S.; Nahm, S., Eds. Springer New York: 2012; pp 405-459.
24. Takeda, H.; Han, J. S.; Nishida, M.; Shiosaki, T.; Hoshina, T.; Tsurumi, T. *Solid State Commun.* **2010**, 150, (17-18), 836-839.

25. Mączka, M.; Macalik, L.; Hermanowicz, K.; Kępiński, L.; Tomaszewski, P. *Journal of Raman Spectroscopy* **2010**, 41, (9), 1059-1066.
26. Tang, J.; Zou, Z.; Ye, J. *Catal. Lett.* **2004**, 92, (1), 53-56.
27. Fu, H.; Pan, C.; Yao, W.; Zhu, Y. *J. Phys. Chem. B* **2005**, 109, (47), 22432-22439.
28. Shi, Z. Q.; Jia, Q. X.; Anderson, W. A. *J. Electron. Mater.* **1991**, 20, (11), 939-944.
29. Chung, D. D. L., *Composite Materials: Functional Materials for Modern Technologies*. Springer: 2003.
30. Kendall, K. R.; Navas, C.; Thomas, J. K.; zur Loye, H.-C. *Chem. Mater.* **1996**, 8, (3), 642-649.
31. Ma, R.; Sasaki, T. *Acc. Chem. Res.* **2015**, 48, (1), 136-143.
32. Sasaki, T.; Watanabe, M. *J. Am. Chem. Soc.* **1998**, 120, (19), 4682-4689.
33. Geng, F.; Ma, R.; Nakamura, A.; Akatsuka, K.; Ebina, Y.; Yamauchi, Y.; Miyamoto, N.; Tateyama, Y.; Sasaki, T. *Nat. Commun.* **2013**, 4, 1632.
34. Maluangnont, T.; Matsuba, K.; Geng, F.; Ma, R.; Yamauchi, Y.; Sasaki, T. *Chem. Mater.* **2013**, 25, (15), 3137.
35. Treacy, M. M. J.; Rice, S. B.; Jacobson, A. J.; Lewandowski, J. T. *Chem. Mater.* **1990**, 2, (3), 279-286.
36. Fukuda, K.; Akatsuka, K.; Ebina, Y.; Ma, R.; Takada, K.; Nakai, I.; Sasaki, T. *ACS Nano* **2008**, 2, (8), 1689-1695.
37. Kim, J.-Y.; Chung, I.; Choy, J.-H.; Park, G.-S. *Chem. Mater.* **2001**, 13, (9), 2759-2761.
38. Fang, M.; Kim, C. H.; Saupe, G. B.; Kim, H.-N.; Waraksa, C. C.; Miwa, T.; Fujishima, A.; Mallouk, T. E. *Chem. Mater.* **1999**, 11, (6), 1526-1532.
39. Zhang, C.; Zhu, Y. *Chem. Mater.* **2005**, 17, (13), 3537-3545.

40. Amano, F.; Nogami, K.; Abe, R.; Ohtani, B. *The Journal of Physical Chemistry C* **2008**, 112, (25), 9320-9326.
41. Zhang, L.; Wang, W.; Chen, Z.; Zhou, L.; Xu, H.; Zhu, W. *J. Mater. Chem.* **2007**, 17, (24), 2526-2532.
42. Sun, S.; Wang, W.; Zhang, L.; Gao, E.; Jiang, D.; Sun, Y.; Xie, Y. *ChemSusChem* **2013**, 6, (10), 1873-1877.
43. Chhowalla, M.; Shin, H. S.; Eda, G.; Li, L.-J.; Loh, K. P.; Zhang, H. *Nat Chem* **2013**, 5, (4), 263-275.
44. Sipos, B.; Kusmartseva, A. F.; Akrap, A.; Berger, H.; Forro, L.; Tutis, E. *Nat Mater* **2008**, 7, (12), 960-965.
45. Kuc, A.; Zibouche, N.; Heine, T. *Physical Review B* **2011**, 83, (24), 245213.
46. Splendiani, A.; Sun, L.; Zhang, Y.; Li, T.; Kim, J.; Chim, C.-Y.; Galli, G.; Wang, F. *Nano Lett.* **2010**, 10, (4), 1271-1275.
47. Radisavljevic, B.; Radenovic, A.; Brivio, J.; Giacometti, V.; Kis, A. *Nature Nanotechnology* **2011**, 6, (3), 147-150.
48. Lembke, D.; Kis, A. *ACS Nano* **2012**, 6, 10070.
49. Radisavljevic, B.; Kis, A. *Nat. Mater.* **2013**, 12, 815.
50. Radisavljevic, B.; Whitwick, M. B.; Kis, A. *ACS Nano* **2011**, 5, 9934.
51. Mak, K. F.; He, K.; Shan, J.; Heinz, T. F. *Nat Nano* **2012**, 7, (8), 494-498.
52. Zeng, H.; Dai, J.; Yao, W.; Xiao, D.; Cui, X. *Nat Nano* **2012**, 7, (8), 490-493.
53. Lin, Y.-C.; Zhang, W.; Huang, J.-K.; Liu, K.-K.; Lee, Y.-H.; Liang, C.-T.; Chu, C.-W.; Li, L.-J. *Nanoscale* **2012**, 4, (20), 6637-6641.

54. Lee, H. S.; Min, S.-W.; Chang, Y.-G.; Park, M. K.; Nam, T.; Kim, H.; Kim, J. H.; Ryu, S.; Im, S. *Nano Lett.* **2012**, 12, (7), 3695-3700.
55. Boscher, N. D.; Blackman, C. S.; Carmalt, C. J.; Parkin, I. P.; Prieto, A. G. *Appl. Surf. Sci.* **2007**, 253, (14), 6041-6046.
56. Boscher, N. D.; Carmalt, C. J.; Palgrave, R. G.; Gil-Tomas, J. J.; Parkin, I. P. *Chem. Vap. Deposition* **2006**, 12, (11), 692-698.
57. Boscher, N. D.; Carmalt, C. J.; Parkin, I. P. *J. Mater. Chem.* **2006**, 16, (1), 122-127.
58. Yan, Y.; Xia, B.; Ge, X.; Liu, Z.; Wang, J.-Y.; Wang, X. *ACS Applied Materials & Interfaces* **2013**, 5, (24), 12794-12798.
59. *Preparation and crystal growth of materials with layered structures*. D. Reidel Publishing Company: Dordrecht, Holland, 1977; Vol. 1, p 280.
60. Ambrosi, A.; Sofer, Z.; Pumera, M. *Small* **2015**, 11, (5), 605-612.
61. Zeng, Z.; Yin, Z.; Huang, X.; Li, H.; He, Q.; Lu, G.; Boey, F.; Zhang, H. *Angew. Chem. Int. Ed.* **2011**, 50, (47), 11093-11097.
62. Py, M. A.; Haering, R. R. *Can. J. Phys.* **1983**, 61, (1), 76-84.
63. Ganal, P.; Olberding, W.; Butz, T.; Ouvrard, G. *Solid State Ionics* **1993**, 59, (3-4), 313-319.
64. Zheng, J.; Zhang, H.; Dong, S.; Liu, Y.; Tai Nai, C.; Suk Shin, H.; Young Jeong, H.; Liu, B.; Ping Loh, K. *Nat Commun* **2014**, 5.
65. Coleman, J. N.; Lotya, M.; O'Neill, A.; Bergin, S. D.; King, P. J.; Khan, U.; Young, K.; Gaucher, A.; De, S.; Smith, R. J.; Shvets, I. V.; Arora, S. K.; Stanton, G.; Kim, H.-Y.; Lee, K.; Kim, G. T.; Duesberg, G. S.; Hallam, T.; Boland, J. J.; Wang, J. J.; Donegan, J. F.; Grunlan, J.

- C.; Moriarty, G.; Shmeliov, A.; Nicholls, R. J.; Perkins, J. M.; Grieveson, E. M.; Theuwissen, K.; McComb, D. W.; Nellist, P. D.; Nicolosi, V. *Science* **2011**, 331, (6017), 568-571.
66. Cunningham, G.; Lotya, M.; Cucinotta, C. S.; Sanvito, S.; Bergin, S. D.; Menzel, R.; Shaffer, M. S. P.; Coleman, J. N. *ACS Nano* **2012**, 6, (4), 3468-3480.
67. O'Neill, A.; Khan, U.; Coleman, J. N. *Chem. Mater.* **2012**, 24, (12), 2414-2421.
68. Xia, J.; Li, H.; Luo, Z.; Xu, H.; Wang, K.; Yin, S.; Yan, Y. *Mater. Chem. Phys.* **2010**, 121, (1-2), 6-9.
69. Fu, H.; Zhang, L.; Yao, W.; Zhu, Y. *Applied Catalysis B: Environmental* **2006**, 66, (1-2), 100-110.
70. Pope, T. R.; Lassig, M. N.; Neher, G.; Weimar III, R. D.; Salguero, T. T. *Journal of Materials Chemistry C* **2014**, 2, (17), 3223.

**CHAPTER 2**  
**CHROMISM OF  $\text{Bi}_2\text{WO}_6$  IN SINGLE CRYSTAL AND NANOSHEET FORMS**

Timothy R. Pope, Melissa N. Lassig, Gregory Neher, Richard D. Weimar III, and Tina T. Salguero. *Journal of Materials Chemistry C*. 2014, 2, 3223–3230. Reproduced by permission of The Royal Society of Chemistry.

**Abstract**

Nanosheets of  $\text{Bi}_2\text{WO}_6$  with lateral dimensions of 1–2  $\mu\text{m}$  and thicknesses of 5–15 nm were prepared using  $\text{Cs}_4\text{W}_{11}\text{O}_{36}^{2-}$  nanosheets as the tungsten oxide precursor and lateral template. The formation of these nanosheets was followed by electron microscopy and powder X-ray diffraction techniques. The isolated  $\text{Bi}_2\text{WO}_6$  nanosheet product was characterized with respect to structure, morphology, spectroscopic properties, and optical properties. The bandgap energy of  $\text{Bi}_2\text{WO}_6$  nanosheets is relatively large at  $\sim 3.1$  eV. The chromism of these sheets with respect to UV irradiation and  $\text{Li}^+$  intercalation was examined in detail. The UV-induced photochromism of dispersed  $\text{Bi}_2\text{WO}_6$  nanosheets is highly dependent on the solvent environment, and the initial color change from white to black is reversible. The photochromic properties of “flowerlike” and single crystal  $\text{Bi}_2\text{WO}_6$  were evaluated as well. Another color change, pale yellow to brown-black, occurred when lithium ions were intercalated into the  $\text{Bi}_2\text{WO}_6$  lattice using n-butyl lithium. Reaction of lithiated  $\text{Bi}_2\text{WO}_6$  with water yielded nanofragments of  $\text{Bi}_2\text{WO}_6$  rather than nanosheets.

## Introduction

Bismuth tungstate ( $\text{Bi}_2\text{WO}_6$ ) is a textbook example of the Aurivillius family of layered perovskite-like metal oxides. Its structure consists of alternating layers of  $\text{Bi}_2\text{O}_2$  and corner sharing  $\text{WO}_6$  octahedra (Figure 1E).<sup>1</sup>  $\text{Bi}_2\text{WO}_6$  is a stable high-temperature ferroelectric material with a Curie temperature of 940 °C, and it displays a larger spontaneous polarization than other bismuth layer-based ferroelectrics.<sup>2,3</sup> This material also has a high electromechanical coupling coefficient, making it suitable for high-temperature piezoelectric applications.

Most recent studies of  $\text{Bi}_2\text{WO}_6$  have focused on its activity for photocatalysis, especially applied to the destruction of organic molecules.<sup>4,5</sup> It has high photogenerated hole mobility and catalytic performance because the bismuth 6s orbitals hybridize with the oxygen 2p orbitals to create a hybridized valence band.<sup>6</sup>

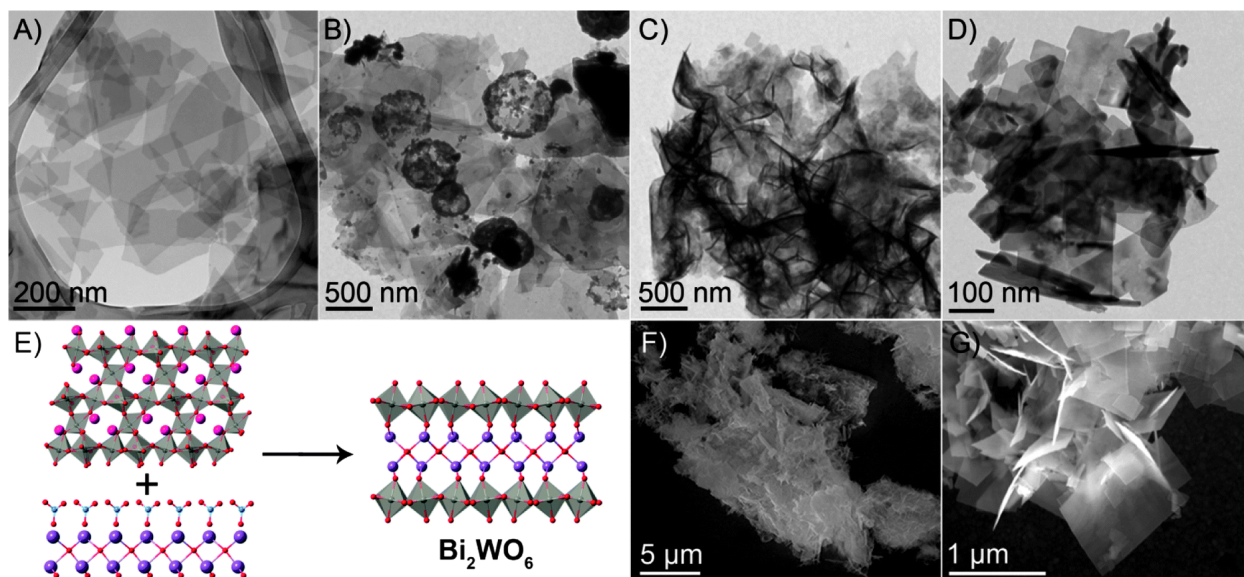


**Figure 2.1** (A) TEM image of the  $\text{Cs}_4\text{W}_{11}\text{O}_{36}^{2-}$  nanosheet precursor. (B) TEM image of  $\text{Cs}_4\text{W}_{11}\text{O}_{36}^{2-} + \text{Bi}(\text{NO}_3)_3$  reaction mixture at 0.5 h. (C and F) TEM and SEM images, respectively, of the reaction mixture at 2 h. (D and G) TEM and SEM images, respectively, of the reaction mixture at 5 h. (E) Reaction scheme illustrating the transformation of a tungsten oxide nanosheet precursor (side view along the b-axis)<sup>32</sup> and a bismuth oxide hydroxide nitrate (side view along the a-axis)<sup>33</sup> into  $\text{Bi}_2\text{WO}_6$  nanosheets (side view along the c-axis).<sup>34</sup>

$\text{Bi}_2\text{WO}_6$  is formed readily by the solid state reaction of  $\text{Bi}_2\text{O}_3$  and  $\text{WO}_3$ , and mm-sized single crystals can be grown from melt fluxes containing  $\text{Li}_2\text{B}_4\text{O}_7$ .<sup>6,7</sup> Furthermore, there are many examples of micro- and nanostructured  $\text{Bi}_2\text{WO}_6$  produced under hydrothermal conditions,<sup>4,5</sup> which has become a preferred method to control photocatalytic performance via particle size, morphology, surface area, and chemical surface functionality. In a typical hydrothermal synthesis, a precursor mixture of  $\text{Na}_2\text{WO}_4$  and  $\text{Bi}(\text{NO}_3)_3$  react to form stacked layers of  $\text{Bi}_2\text{WO}_6$  nanosheets.<sup>4</sup> Layers preferentially undergo anisotropic growth, expanding laterally instead of vertically. Typical products include micron-sized “flowerlike” clusters of  $\text{Bi}_2\text{WO}_6$  platelets,<sup>8,9</sup> although morphologies can be influenced by pH or the use of a surfactant.<sup>10-20</sup>

A cation-deficient analog of the Aurivillius phase is  $\text{Bi}_2\text{W}_2\text{O}_9$ .<sup>21</sup> In pioneering studies, Schaak and Mallouk showed that acid leaching bismuth oxide from  $\text{Bi}_2\text{W}_2\text{O}_9$  provides a colloidal dispersion of  $\text{H}_2\text{W}_2\text{O}_7$  nanosheets, a layered-perovskite solid acid.<sup>22</sup> Subsequent studies by Osterloh and co-workers showed that sub-nm thick nanosheets of  $\text{WO}_3$  (formally  $\text{H}_2\text{W}_2\text{O}_7$  stabilized with tetrabutylammonium cations) have photocatalytic hydrolysis properties comparable to bulk  $\text{WO}_3$ .<sup>23</sup>

When exposed to UV light, nanosized  $\text{WO}_3$  undergoes a photochromic shift in which the once clear material darkens significantly.<sup>24-26</sup> Thus,  $\text{WO}_3$  and metal-doped derivatives have been investigated as candidates for electrochromic devices, specifically “smart windows” that regulate the transmission of sunlight.<sup>27-29</sup> Inorganic electrochromic devices are favorable because they display high UV-stability, a wide operational temperature range, high contrast, viewing angle independence, and variable coloration intensities.<sup>30</sup>

Various other tungsten oxide derivatives also exhibit photochromic properties. For instance, Sasaki and co-workers have reported tungstate-based nanosheets derived from layered  $\text{Cs}_{6+x}\text{W}_{11}\text{O}_{36}$  and  $\text{Rb}_4\text{W}_{11}\text{O}_{35}$  materials that darken under UV irradiation.<sup>26,31</sup>

In this contribution, we discuss the chromism of  $\text{Bi}_2\text{WO}_6$  with several examples. We find that the photochromism of dispersed  $\text{Bi}_2\text{WO}_6$  nanosheets is highly dependent on solvent choice, and that the color change is reversible. Additionally, we compare the photochromism of  $\text{Bi}_2\text{WO}_6$  nanosheets with that of  $\text{Bi}_2\text{WO}_6$  in flowerlike clusters and single crystal form. In another case, we find that chromism also can be induced by the intercalation of lithium ions into the  $\text{Bi}_2\text{WO}_6$  structure.

## Results and Discussion

### *$\text{Bi}_2\text{WO}_6$ nanosheets from $\text{Cs}_4\text{W}_{11}\text{O}_{36}^{2-}$ nanosheets*

The strategy we apply here uses  $\text{Cs}_4\text{W}_{11}\text{O}_{36}^{2-}$  nanosheets as the tungsten-containing precursor for  $\text{Bi}_2\text{WO}_6$  formation, together with a commonly used source of bismuth,  $\text{Bi}(\text{NO}_3)_3$ , and without the use of a pH buffer or surfactant. The  $\text{Cs}_4\text{W}_{11}\text{O}_{36}^{2-}$  nanosheets aid the formation of well-defined  $\text{Bi}_2\text{WO}_6$  nanosheets by acting as a template for nanosheet growth.

$\text{Cs}_4\text{W}_{11}\text{O}_{36}^{2-}$  nanosheets were prepared from  $\text{Cs}_{6+x}\text{W}_{11}\text{O}_{36}$  as described previously,<sup>26</sup> except without the addition of tetrabutyl ammonium (TBA) ligands. In this synthesis, silver-gray  $\text{Cs}_{6+x}\text{W}_{11}\text{O}_{36}$  crystals are fully exfoliated to yield a pearlescent white dispersion of  $\text{Cs}_4\text{W}_{11}\text{O}_{36}^{2-}$  nanosheets. Transmission electron microscopy (TEM) confirms the morphology of this product (Figure 2.1A), and atomic force microscopy (AFM) shows that these nanosheets have an average thickness of 2.5 nm, which is comparable to the value of 2 nm reported for TBA-stabilized  $\text{Cs}_4\text{W}_{11}\text{O}_{36}^{2-}$  nanosheets.<sup>26</sup>

Occasionally the  $\text{Cs}_4\text{W}_{11}\text{O}_{36}^{2-}$  dispersion became yellow during the exfoliation process. Both TEM and powder X-ray diffraction (PXRD) analysis indicate that these samples contain restacked  $\text{Cs}_4\text{W}_{11}\text{O}_{36}^{2-}$  nanosheets. TEM images show noticeably thicker, irregular multilayer structures. Increased ordering of the crystal structure, corresponding to thicker material, is corroborated by more intense PXRD patterns. Such restacked nanosheets do not display the same reactivity as the monolayer material and yield non-uniform  $\text{Bi}_2\text{WO}_6$  nanosheets, along with larger platelet and rod morphologies. Thus, in this work, only fully exfoliated  $\text{Cs}_4\text{W}_{11}\text{O}_{36}^{2-}$  was used to prepare  $\text{Bi}_2\text{WO}_6$  nanosheets. If restacking occurs, this material can be re-exfoliated with mild sonication in 12 M HCl.

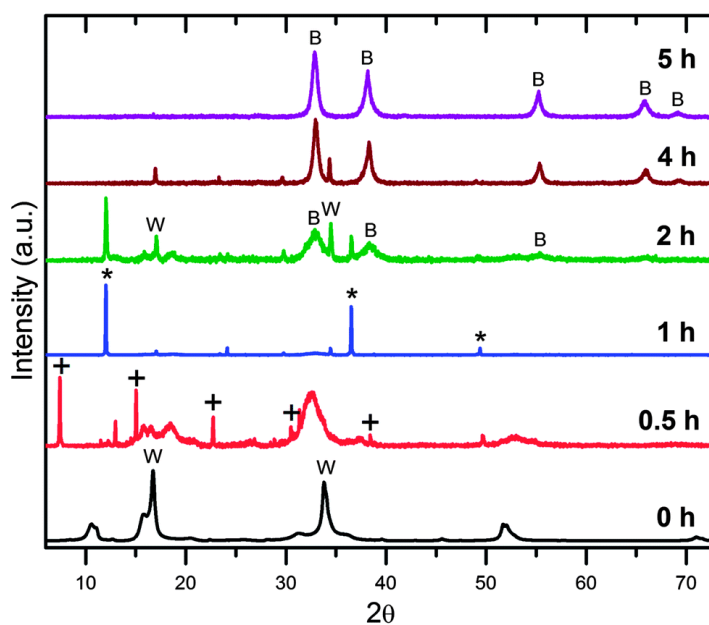


**Figure 2.2** PXRD patterns collected at intervals during the transformation of  $\text{Cs}_4\text{W}_{11}\text{O}_{36}^{2-}$  nanosheets into  $\text{Bi}_2\text{WO}_6$  nanosheets. Symbols for identified species include: + for  $[\text{Bi}_6\text{O}_5(\text{OH})_3](\text{NO}_3)_5 \cdot 3\text{H}_2\text{O}$  (JCPDS 00-053-1038), \* for  $[\text{Bi}_6\text{O}_6(\text{OH})_3](\text{NO}_3)_3 \cdot 1.5\text{H}_2\text{O}$  (JCPDS 00-048-0575), W for  $\text{Cs}_4\text{W}_{11}\text{O}_{36}^{2-}$ , B for  $\text{Bi}_2\text{WO}_6$  nanosheets.

Under hydrothermal conditions,  $\text{Cs}_4\text{W}_{11}\text{O}_{36}^{2-}$  nanosheets react with  $\text{Bi}(\text{NO}_3)_3$  over the course of several hours to form  $\text{Bi}_2\text{WO}_6$  nanosheets. Before discussing the characterization of this product, we describe a time study that provides some insight into the  $\text{Cs}_4\text{W}_{11}\text{O}_{36}^{2-}$  to  $\text{Bi}_2\text{WO}_6$  transformation. Electron microscopy images and PXRD data that correspond to several intermediate points along the reaction process are presented in Figures 2.1 and 2.2.

After 0.5 h of reaction time, the initial  $\text{Bi}(\text{NO}_3)_3$  is transformed into  $[\text{Bi}_6\text{O}_5(\text{OH})_3](\text{NO}_3)_5 \cdot 3\text{H}_2\text{O}$ . The formation of distinctive circular bismuth oxide nanosheets/platelets is apparent by TEM (Figure 1B), and this species is present in the PXRD pattern (Figure 2). By the 1 h mark, however, all the  $[\text{Bi}_6\text{O}_5(\text{OH})_3](\text{NO}_3)_5 \cdot 3\text{H}_2\text{O}$  is converted into  $[\text{Bi}_6\text{O}_6(\text{OH})_3](\text{NO}_3)_3 \cdot 1.5\text{H}_2\text{O}$ . The PXRD pattern in Figure 2 shows that initially highly crystalline  $[\text{Bi}_6\text{O}_6(\text{OH})_3](\text{NO}_3)_3 \cdot 1.5\text{H}_2\text{O}$  forms. Previous reports also have noted that  $\text{Bi}(\text{NO}_3)_3$  converts to  $[\text{Bi}_6\text{O}_6(\text{OH})_3](\text{NO}_3)_3 \cdot 1.5\text{H}_2\text{O}$  under similar hydrothermal conditions.<sup>35</sup> It appears that this species becomes the bismuth oxide source that reacts with  $\text{Cs}_4\text{W}_{11}\text{O}_{36}^{2-}$  nanosheets. In contrast, detailed in situ energy-dispersive X-ray diffraction experiments by Patzke and co-workers showed that only peaks corresponding to crystalline  $\text{Bi}_2\text{WO}_6$  are seen when  $\text{K}_2\text{WO}_4$  reacts with  $\text{Bi}(\text{NO}_3)_3$ .<sup>36</sup>

At the 2 h mark, formation of bismuth oxide from  $[\text{Bi}_6\text{O}_6(\text{OH})_3](\text{NO}_3)_3 \cdot 1.5\text{H}_2\text{O}$  is seen by TEM in Figure 2.1C and by PXRD in Figure 2.2. At this point the circular platelets become lateral sheets. As discussed by Zhang, et al.,  $\text{Bi}_2\text{WO}_6$  preferentially grows laterally along the c-axis.<sup>4</sup> In our present work, the morphology of the  $\text{Cs}_4\text{W}_{11}\text{O}_{36}^{2-}$  further promotes the formation of large two-dimensional crystals. However, the bismuth oxide is not yet fully incorporated, seen by the irregular clustering in the scanning electron microscopy (SEM) image (Figure 2.1F) and the  $[\text{Bi}_6\text{O}_6(\text{OH})_3](\text{NO}_3)_3 \cdot 1.5\text{H}_2\text{O}$  peaks in the PXRD (Figure 2.2). At this point in the reaction, we also observe a minor form of bismuth oxide with rod-like structure. The concentration of

$[\text{Bi}_6\text{O}_6(\text{OH})_3](\text{NO}_3)_3 \cdot 1.5\text{H}_2\text{O}$  is markedly decreased by the 4 h mark as the reaction with  $\text{Cs}_4\text{W}_{11}\text{O}_{36}^{2-}$  progresses. PXRD confirms the corresponding increase in the concentration of  $\text{Bi}_2\text{WO}_6$  nanosheets (Figure 2.2).

After 5 h at hydrothermal conditions, all of the cesium ions present in the  $\text{Cs}_4\text{W}_{11}\text{O}_{36}^{2-}$  crystal lattice have been leached out and the tungsten oxide reacts with bismuth oxide to form the  $\text{Bi}_2\text{WO}_6$  nanosheets. PXRD in Figure 2.2 shows the clean formation of  $\text{Bi}_2\text{WO}_6$  and exhibits broad peak widths consistent with a nanostructured material. TEM and SEM images in Figures 2.1D and G show that  $\text{Bi}_2\text{WO}_6$  forms nanosheet clusters but with no macrostructure, as opposed to the flowerlike morphologies obtained without the  $\text{Cs}_4\text{W}_{11}\text{O}_{36}^{2-}$  templates. Additionally, no bismuth oxide species are seen. The samples for this electron microscopy study were not ground prior to analysis, but when  $\text{Bi}_2\text{WO}_6$  nanosheet samples were prepared by grinding and mild sonication, we observed well-separated nanosheets. In particular, the SEM images in Figure 2.3 highlight the defined edges and “jigsaw-like” morphology of the  $\text{Bi}_2\text{WO}_6$  nanosheets formed by this route.

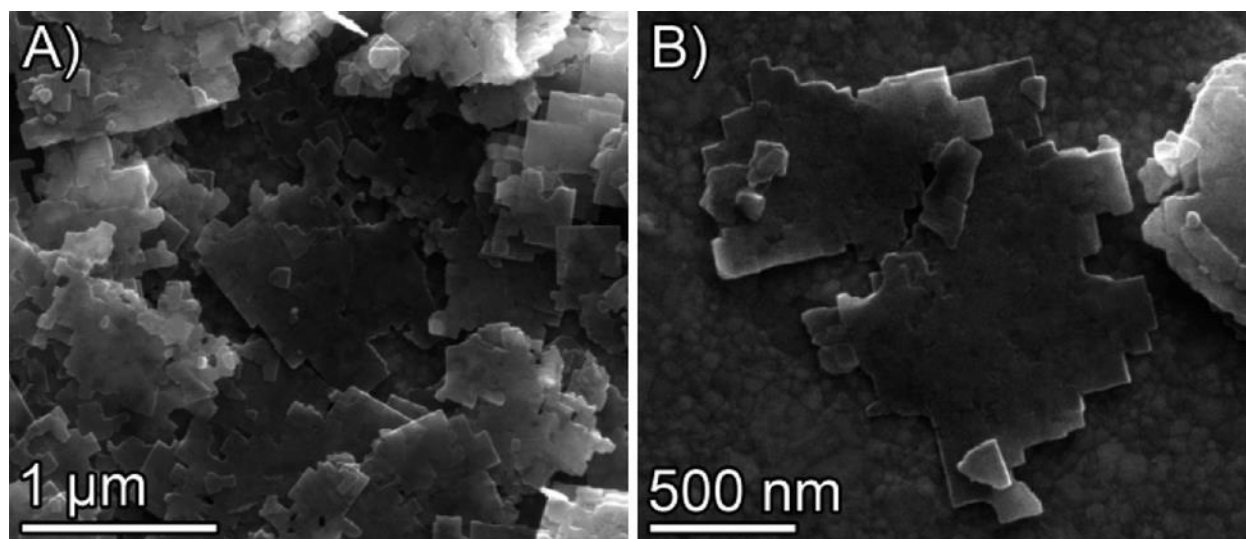


Figure 2.3 SEM images of isolated  $\text{Bi}_2\text{WO}_6$  nanosheets that highlight the morphology of this material. Image (B) clearly shows that typical lateral dimensions are in the 1–2  $\mu\text{m}$  range.

We obtained similar results for the reaction over a range of temperatures (180–220 °C) and times (5–24 h). Nanosheet products can be isolated simply by filtering, grinding, and re-dispersing in isopropyl alcohol. Cesium ions remain in the filtrate, separate from the nanosheets, as shown by electrospray ionization mass spectrometry. In contrast to bulk  $\text{Bi}_2\text{WO}_6$ , which is yellowish in color,  $\text{Bi}_2\text{WO}_6$  nanosheet powders are white and disperse readily in water to yield pearlescent dispersions. Individual  $\text{Bi}_2\text{WO}_6$  nanosheets have lateral dimensions in the 1–2  $\mu\text{m}$  range, as measured by SEM (Figure 2.3) and AFM, which are significantly larger than those prepared without a  $\text{Cs}_4\text{W}_{11}\text{O}_{36}^{2-}$  template.<sup>4</sup> The thickness range of typical  $\text{Bi}_2\text{WO}_6$  nanosheets is 5–15 nm according to electron microscopy images and AFM measurements.

The Raman spectrum of these  $\text{Bi}_2\text{WO}_6$  nanosheets is consistent with data in the literature.<sup>37</sup> Raman peaks at 828, 792, 708, 415, 301, 279, 257, and 220  $\text{cm}^{-1}$  correspond to the bending and stretching modes of  $\text{WO}_6$ , whereas those at 368 and 327  $\text{cm}^{-1}$  correspond to the bending modes of  $(\text{Bi}_2\text{O}_2)^{2+}$ . Other nano-morphologies, particularly flowerlike  $\text{Bi}_2\text{WO}_6$ , display similar peaks in the Raman spectra. In comparison to the Raman spectrum of a single crystal of  $\text{Bi}_2\text{WO}_6$ ,<sup>7</sup> we observe peak broadening for the  $\text{Bi}_2\text{WO}_6$  nanosheets, indicative of heterogeneous bond distances that may originate from strain and defects at the nanoscale.<sup>38</sup> The Raman spectrum of  $\text{Bi}_2\text{WO}_6$  nanosheets also exhibited some decreased peak intensities compared to single crystal  $\text{Bi}_2\text{WO}_6$ , primarily at 301, 279, 257 and 220  $\text{cm}^{-1}$ . Previous work by Maczka, et al. showed that decreased peak intensity can be correlated to a reduction in the  $\text{Bi}_2\text{WO}_6$  thickness.<sup>37</sup> The thin structure of  $\text{Bi}_2\text{WO}_6$  nanosheets presented here contributes to a decrease in the orthorhombic distortion, causing a decrease in band intensity.

### *Optical properties of Bi<sub>2</sub>WO<sub>6</sub> nanosheets*

The molar extinction coefficient  $\epsilon$  of a colloidal dispersion of Bi<sub>2</sub>WO<sub>6</sub> nanosheets, approximately  $280 \text{ m}^2 \text{ mol}^{-1}$ , was determined from the slope of an absorbance (at 281 nm) versus concentration plot. This value is consistent with medium-intensity absorption, and the linear Beer–Lambert relationship indicates that the nanosheets are uniformly dispersed and well-behaved in isopropyl alcohol.

Figure 2.4 shows UV-vis diffuse reflectance data for Bi<sub>2</sub>WO<sub>6</sub> nanosheets and for comparison, flowerlike Bi<sub>2</sub>WO<sub>6</sub> previously described in the literature. Both samples exhibit strong absorption bands below 350 nm, with an onset in the visible region at  $\sim 425$  nm. This onset wavelength is typical for nanostructured Bi<sub>2</sub>WO<sub>6</sub> and slightly blue shifted with respect to bulk Bi<sub>2</sub>WO<sub>6</sub>, which is consistent with the white color of Bi<sub>2</sub>WO<sub>6</sub> nanosheets.

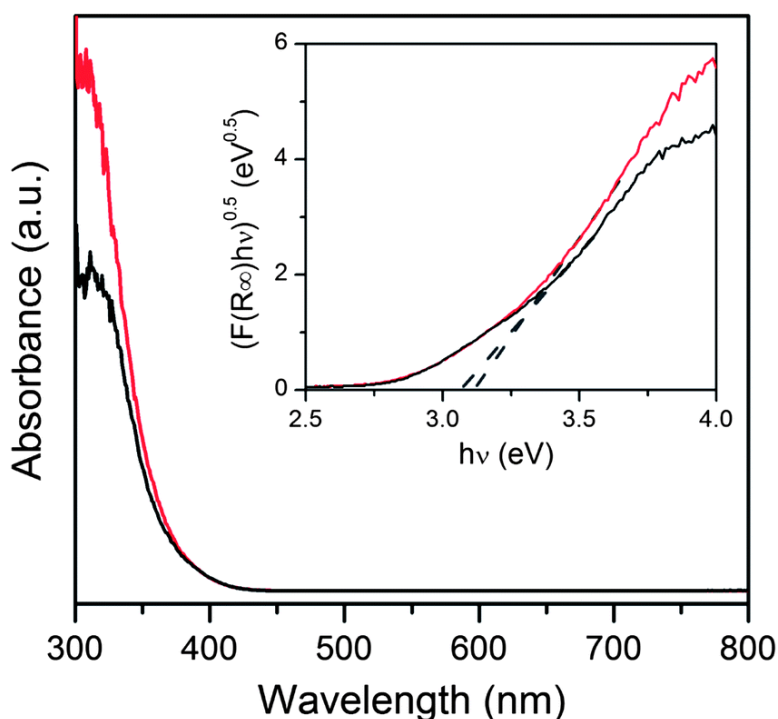


**Figure 2.4** UV-vis diffuse reflectance data for Bi<sub>2</sub>WO<sub>6</sub> nanosheets (black curve) and Bi<sub>2</sub>WO<sub>6</sub> flowerlike structures (red curve). Inset: corresponding Tauc plot used to estimate the optical bandgaps of these samples.

The optical bandgaps of  $\text{Bi}_2\text{WO}_6$  nanosheets and flowerlike structures were estimated by the Tauc method for an indirect allowed electronic transition; the curves shown in Figure 2.4 (inset) exhibit linear Tauc regions just beyond the absorption edges, and the intercepts of these lines with the photon energy axis provide bandgap values. The corresponding bandgap energies of these samples are the same within error,  $\sim 3.1$  eV. This value approaches the upper end of experimentally determined bandgaps for  $\text{Bi}_2\text{WO}_6$ . Comparable examples include  $\text{Bi}_2\text{WO}_6$  multilayered discs ( $\sim 2.9$  eV)<sup>17</sup> and hierarchical  $\text{Bi}_2\text{WO}_6$  microspheres (2.95–3.04 eV).<sup>36</sup> We note, however, that even literature values for bulk  $\text{Bi}_2\text{WO}_6$  vary widely (2.6–3.3 eV),<sup>39–42</sup> as does the use of direct vs. indirect bandgap semiconductor models. Although size, shape, and structure are known to strongly influence the electronic character of a material, it is challenging to rationalize any trend in previously reported  $\text{Bi}_2\text{WO}_6$  bandgap values.

#### *Photochromism of $\text{Bi}_2\text{WO}_6$*

Upon UV irradiation, colloidal dispersions of these  $\text{Bi}_2\text{WO}_6$  nanosheets dramatically change appearance from milky white to black in color (Figure 2.5 inset). Although there is only a slight change to gray after 15 min of UV irradiation, the color becomes saturated after  $\sim 30$  min. To further analyze this phenomenon, we tracked the absorbance of  $\text{Bi}_2\text{WO}_6$  nanosheets during UV irradiation. As shown in Figure 5, UV-vis spectra were collected at 5 min intervals. The broad absorbance present at 230–600 nm in the starting material became less pronounced after 10 min as two new, strong peaks emerged at  $\lambda_{\text{max}}$  of  $\sim 273$  and  $\sim 203$  nm. After 30 min, this peak reached maximum intensity at  $\sim 0.2$  absorption units greater than the un-irradiated starting point.

Darkened  $\text{Bi}_2\text{WO}_6$  nanosheets could be isolated by centrifugation, and their color bleached completely upon either heating at 105 °C for 15 min or washing with copious amounts of water.

UV-irradiated  $\text{Bi}_2\text{WO}_6$  nanosheets stored in the dark settle out of solution and turn gray in color, but the sample becomes black again after additional UV irradiation. The photochromism in this system showed good reversibility; cycling between colored and bleached states could be repeated three or more times.

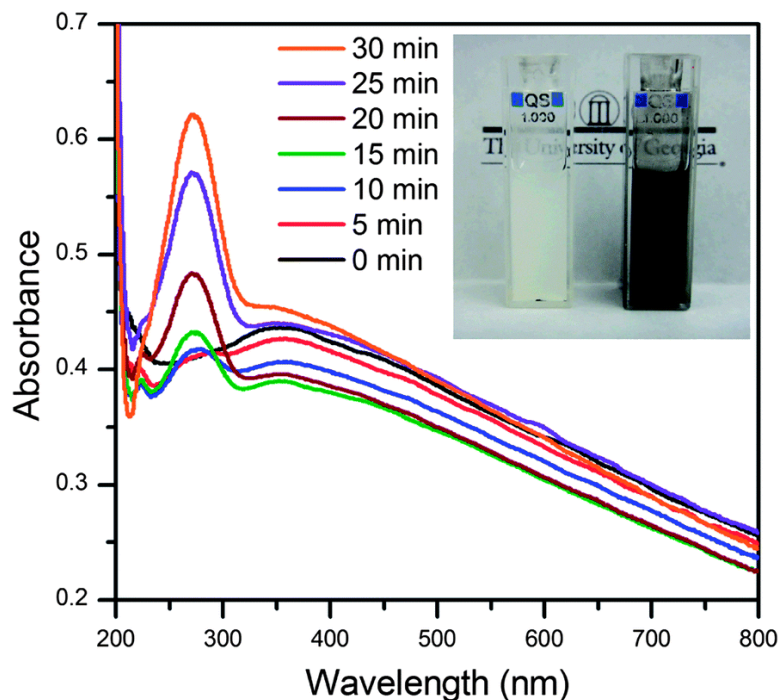


**Figure 2.5** UV-vis spectra of a UV-irradiated,  $1.3 \times 10^{-4}$  M dispersion of  $\text{Bi}_2\text{WO}_6$  nanosheets in isopropyl alcohol taken at 5 min intervals. Inset: photograph showing the dramatic color change of a concentrated  $\text{Bi}_2\text{WO}_6$  nanosheet dispersion before (white) and after (black) UV irradiation.

To further elucidate the mechanism of color change,  $\text{Bi}_2\text{WO}_6$  nanosheets were evaluated in a variety of solvents. The resulting observations about the presence or absence of photochromic behavior revealed that the photochromism of  $\text{Bi}_2\text{WO}_6$  nanosheets is highly solvent dependent. The color change occurred in alcohols, ethers, and amines yet not in water, amides, alkanes, or conjugated molecules (e.g., pyridine, benzyl alcohol). Many of the solvent environments that

support photochromic behavior in this system are known to be “hole scavengers”, molecules that donate electrons to valence band holes created upon excitation. In  $\text{WO}_3$  and  $\text{TiO}_2$  nanoparticles, for example, such hole scavengers can suppress electron–hole recombination and thus allow trapped surface electrons to impact the visible absorption.<sup>25,43</sup> Likewise, conjugated molecules like benzyl alcohol are known as “electron scavengers” that promote electron–hole recombination.

For comparison, we evaluated the photochromic properties of flowerlike  $\text{Bi}_2\text{WO}_6$ ,<sup>8</sup> which exhibited a similar color change as the  $\text{Bi}_2\text{WO}_6$  nanosheets prepared in this work: from white to gray/black. However, the corresponding UV-vis spectra showed a less dramatic change in absorption properties after UV irradiation.

Moreover, we observed that bulk  $\text{Bi}_2\text{WO}_6$  in single crystal form is photochromic as well; to our knowledge this property has not been reported previously for  $\text{Bi}_2\text{WO}_6$ —despite the fact that photochromism is well-known for many other tungsten oxide-based materials.<sup>25</sup> The pale yellow single crystals of  $\text{Bi}_2\text{WO}_6$  shown in the middle of Figure 2.6 become distinctly gray in color (leftmost crystals) upon UV irradiation within a solvent-filled environment, and they maintain this color for days under ambient benchtop conditions. Dry solid samples did not exhibit photochromic behavior, however, which confirms the important role of the solvent in the mechanism.

$\text{Cs}_4\text{W}_{11}\text{O}_{36}^{2-}$  nanosheets, such as those used as the precursor/template for  $\text{Bi}_2\text{WO}_6$  nanosheets in this work, also are photochromic. Similar to the TBA- $\text{Cs}_4\text{W}_{11}\text{O}_{36}^{2-}$  nanosheets studied by Sasaki and co-workers,<sup>26</sup> a dispersion of  $\text{Cs}_4\text{W}_{11}\text{O}_{36}^{2-}$  nanosheets changes from colorless to blue upon UV irradiation. The corresponding UV-vis spectrum shows a broad absorption at 600–1000  $\text{cm}^{-1}$  that is responsible for the blue color, but the overall change in absorption is less dramatic than that observed for  $\text{Bi}_2\text{WO}_6$  nanosheets.

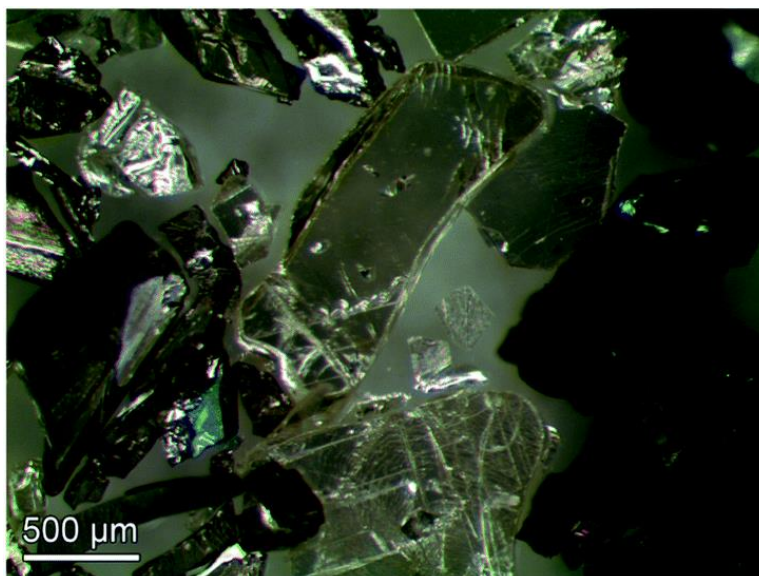


Figure 2.6 Optical microscopy image of  $\text{Bi}_2\text{WO}_6$  (pale yellow crystals in center), UV-irradiated  $\text{Bi}_2\text{WO}_6$  (gray crystals at left), and Li-intercalated  $\text{Bi}_2\text{WO}_6$  (black crystals at right).

Although the exact mechanism of photochromism in  $\text{Bi}_2\text{WO}_6$  is not yet known at this early point of study, we can make several informed observations.  $\text{Bi}_2\text{WO}_6$  clearly is different from both  $\text{WO}_3$  and  $\text{TiO}_2$  nanoparticles, two well-studied, inorganic photochromic systems. In the former case, the color change is believed to derive from photogenerated oxygen radicals trapped at defect sites, accompanied by metal reduction.<sup>25</sup> This situation is favored by high levels of oxygen vacancies, especially in amorphous  $\text{WO}_3$  samples. In the latter case, the color originates from stabilized surface electrons that lead to red-near infrared absorption.<sup>44</sup> Such surface electrons are highly sensitive to environmental conditions, e.g. solvent effects. In contrast to these cases, irradiated  $\text{Bi}_2\text{WO}_6$  absorbs strongly in the UV region rather than the red-infrared. Because the color change is robust, even upon isolation, it seems likely that the color centers correspond to reduced metal (bismuth and/or tungsten). Upon heating in air, these ions become re-oxidized and the material reverts back to its original color. In related work, Nozik and co-workers showed that excess donated electrons from hole scavengers could reduce  $\text{WO}_3$  to form  $\text{WO}_{3-x}$ .<sup>45</sup> The oxygen

atoms in the  $(\text{Bi}_2\text{O}_2)^{2+}$  layers are weakly bound as well, and so oxygen dissociation may also occur here during surface reduction. Similar chemistry has been reported for  $\text{SrBi}_2\text{Ta}_2\text{O}_9$ , which contains the same layered  $\text{Bi}_2\text{O}_2$  motif.<sup>46</sup>

### *Chromism of lithiated $\text{Bi}_2\text{WO}_6$*

A related class of materials relevant to electrochromic devices is the tungsten bronzes, which like  $\text{Bi}_2\text{WO}_6$ , contain  $\text{WO}_6$  octahedra and structural vacancies accessible for intercalation.<sup>47,48</sup> The  $\text{WO}_3$  structure was found to greatly affect both the thermodynamics and kinetics of lithium intercalation into the material.<sup>49</sup>

Cruz and co-workers showed that lithium can be incorporated electrochemically into  $\text{Bi}_2\text{WO}_6$ ,<sup>50</sup> and Xie and co-workers investigated flowerlike  $\text{Bi}_2\text{WO}_6$  as an active electrode material in lithium-ion batteries.<sup>51</sup> Other reports have shown that lithium can be chemically incorporated into another Aurivillius-type layered perovskite oxide,  $\text{Bi}_4\text{Ti}_3\text{O}_{12}$ , using n-butyl lithium.<sup>52</sup> Upon intercalation, these crystals change from yellowish to black. This color change was attributed to the partial reduction of bismuth and titanium. Upon reacting with water, the lithiated samples broke into nanosized particles that the authors characterize as nanoplatelets. The exfoliation of layered transition metal dichalcogenides by this approach also can be quite successful; the reaction of  $\text{Li}^+$  within the van der Waals gap with water to generate  $\text{LiOH}$  and  $\text{H}_2$  forces the layers apart.<sup>53,54</sup>

We observed chromism upon the incorporation of lithium ions into  $\text{Bi}_2\text{WO}_6$  single crystals. The pale yellow crystals (Figure 2.6 middle) turned brown-black in the presence of n-butyl lithium (Figure 2.6 right), with a metallic appearance similar to tungsten bronze products.<sup>55</sup> The PXRD pattern of the lithiated  $\text{Bi}_2\text{WO}_6$  single crystals shows no change compared to bulk  $\text{Bi}_2\text{WO}_6$  before lithiation. Similar results have been reported for the lithiation of  $\text{Bi}_{3.25}\text{La}_{0.75}\text{Ti}_3\text{O}_{12}$ , another

Aurivillius-phase material, with n-butyl lithium. In this study, Chevallier and co-workers determined that the intercalated lithium ions reside in the  $(\text{Bi}_2\text{O}_2)^{2+}$  layers and barely perturb the crystal structure.<sup>56</sup>

We hypothesize that the dramatic color change from pale yellow to brown-black arises from partial reduction of bismuth and tungsten, similar to the example of lithiated  $\text{Bi}_4\text{Ti}_3\text{O}_{12}$ .<sup>52</sup> A reversible color change also was observed in the  $\text{Bi}_{3.25}\text{La}_{0.75}\text{Ti}_3\text{O}_{12}$  system.<sup>56</sup>

As in prior studies, we removed lithium from lithiated  $\text{Bi}_2\text{WO}_6$  by water treatment under mild sonication. The crystals returned to a pale yellow color, although they also clearly became smaller, as indicated by PXRD peak broadening (Figure 2.7 top trace). When mm-sized  $\text{Bi}_2\text{WO}_6$  crystals were used in this reaction sequence, we obtained the mixture shown in Figure 2.8A: a white aqueous dispersion of irregular  $\text{Bi}_2\text{WO}_6$  nanoparticles, characterized by TEM (Figures 2.8B and C), and small yellow crystals of  $\text{Bi}_2\text{WO}_6$  at the bottom of the vial. These results are consistent with lithiation of only the outermost portion of the large  $\text{Bi}_2\text{WO}_6$  crystals, followed by fragmentation that leaves the unreacted inner core behind. In contrast, powdered  $\text{Bi}_2\text{WO}_6$  (ground single crystals) was completely degraded by these lithiation conditions, resulting in an amorphous PXRD pattern.

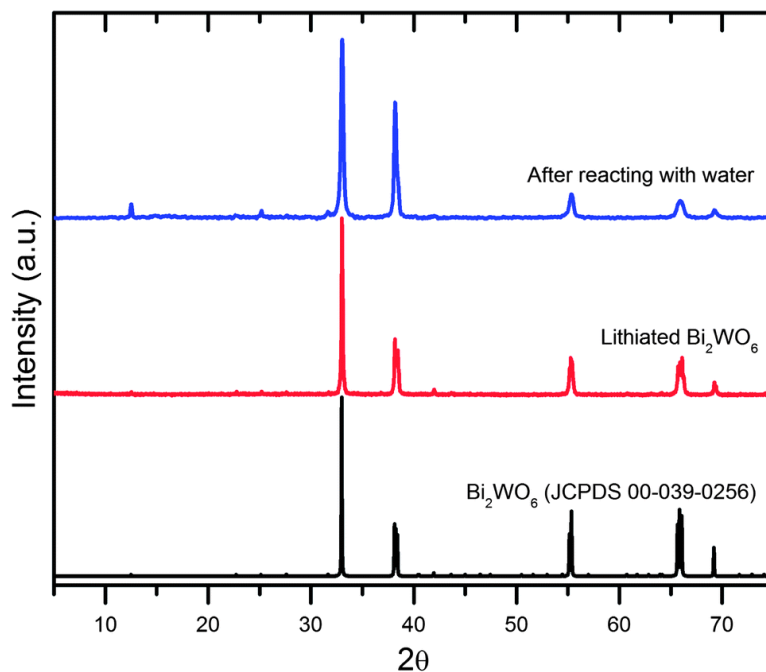


**Figure 2.7** PXR D patterns of  $\text{Bi}_2\text{WO}_6$  reference (black), ground lithiated single crystals (red) and after reacting with water (blue).

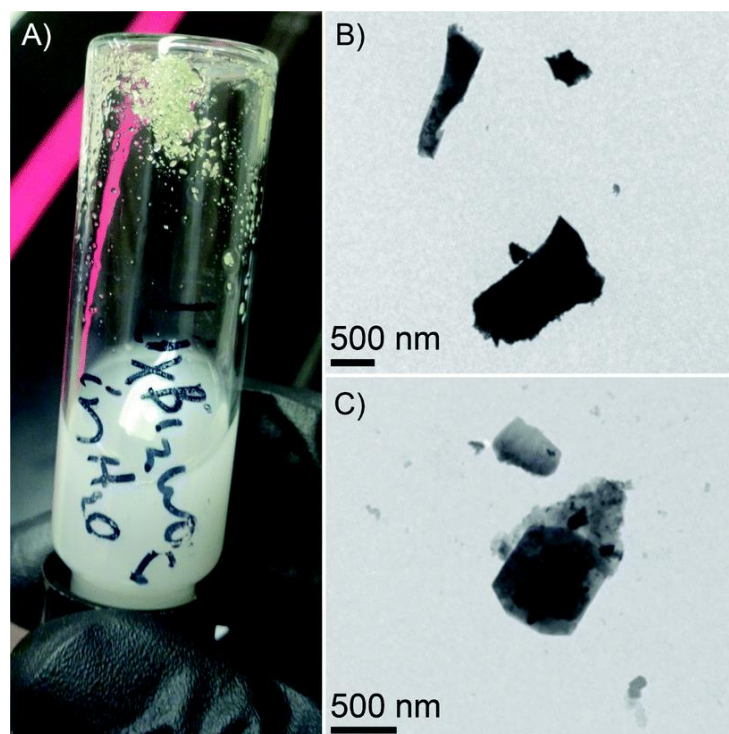


**Figure 2.8** (A) Inverted vial of dispersed  $\text{Bi}_2\text{WO}_6$  and remaining  $\text{Bi}_2\text{WO}_6$  crystals prepared by reacting lithiated  $\text{Bi}_2\text{WO}_6$  with water. (B and C) TEM images of  $\text{Bi}_2\text{WO}_6$  nano-particulates located in the white dispersion.

## Conclusions

In this contribution, we have described a successful approach to making highly anisotropic nanosheets of  $\text{Bi}_2\text{WO}_6$  with large lateral dimensions (1–2  $\mu\text{m}$ ) and 5–15 nm thicknesses. Lateral control can be achieved through the use of a  $\text{Cs}_4\text{W}_{11}\text{O}_{36}^{2-}$  nanosheet template. In this reaction, the initial bismuth source,  $\text{Bi}(\text{NO}_3)_3$ , transforms into  $[\text{Bi}_6\text{O}_5(\text{OH})_3](\text{NO}_3)_5 \cdot 3\text{H}_2\text{O}$  within 0.5 h, and after 1 h becomes  $[\text{Bi}_6\text{O}_6(\text{OH})_3](\text{NO}_3)_3 \cdot 1.5\text{H}_2\text{O}$ , which was found to be the bismuth source relevant to the formation of  $\text{Bi}_2\text{WO}_6$  nanosheets. The layered  $\text{Bi}_2\text{WO}_6$  nanosheets are formed after 5 h at solvothermal conditions. Without the  $\text{Cs}_4\text{W}_{11}\text{O}_{36}^{2-}$  nanosheet template, flowerlike clusters are formed instead.

Optical characterization of  $\text{Bi}_2\text{WO}_6$  nanosheets shows that they absorb strongly in the UV and have a relatively high band gap of  $\sim 3.1$  eV. The most surprising result is the photochromic behavior of  $\text{Bi}_2\text{WO}_6$  in nanosheet, flowerlike, and single crystal forms. Although not yet examined in detail, we propose that the mechanism of white to black color change in this system involves bismuth and/or tungsten reduction. Notably, the color change is robust and reversible.

Additionally, lithium ions can be intercalated chemically into the  $\text{Bi}_2\text{WO}_6$  structure through the use of n-butyl lithium. This reaction provides another example of  $\text{Bi}_2\text{WO}_6$  chromism, in this case pale yellow to brown-black. The subsequent reaction of lithiated  $\text{Bi}_2\text{WO}_6$  with water provides nanofragments of  $\text{Bi}_2\text{WO}_6$  rather than nanosheets. We conclude that our  $\text{Cs}_4\text{W}_{11}\text{O}_{36}^{2-}$  nanosheet templating approach remains the most effective way to prepare and isolate large  $\text{Bi}_2\text{WO}_6$  nanosheets.

## Experimental

### *Preparation of Bi<sub>2</sub>WO<sub>6</sub> nanosheets*

0.6956 g (1.43 mmol) of Bi(NO<sub>3</sub>)<sub>3</sub>·5H<sub>2</sub>O and 4.2 mL of a 15.5 mM aqueous solution of Cs<sub>4</sub>W<sub>11</sub>O<sub>36</sub><sup>2-</sup> nanosheets (7.90 mmol) were mixed thoroughly in an agate mortar. Once homogeneous, this mixture was diluted to ~30 mL total and stirred at room temperature for 2–4 h. Then this dispersion was transferred to a 42 mL Teflon-lined autoclave and heated at 220 °C for 6 h. The resulting Bi<sub>2</sub>WO<sub>6</sub> nanosheets were collected by vacuum filtration using a 0.4 μm membrane filter, and they were washed with deionized water followed by ethanol. Isolated yield of dried Bi<sub>2</sub>WO<sub>6</sub> nanosheet powder was 0.4852 g (97% yield). For characterization and subsequent experiments, this powder was hand ground with a mortar/pestle and then dispersed in water with mild bath sonication. For the time study, a homogenous mixture of the precursors was divided into individual autoclaves and heated at 180 °C for the reported times. The products were collected by vacuum filtration and then re-dispersed for analysis.

### *UV irradiation experiments*

Typical UV irradiation experiments were performed on samples of ~35 mg Bi<sub>2</sub>WO<sub>6</sub> dispersed in 5 mL solvent, unless another concentration is specified. Dispersions were placed in 1 cm<sup>2</sup> double-sided cuvettes and irradiated for 2 h with a quartz mercury vapor grid lamp with a power of 450 μW cm<sup>-2</sup>, located 5 cm away from the sample.

### *Intercalation of Bi<sub>2</sub>WO<sub>6</sub> with lithium*

A typical method for the intercalation of lithium into Bi<sub>2</sub>WO<sub>6</sub> entails the following: within an Ar-filled glovebox, place 0.25 g of bulk Bi<sub>2</sub>WO<sub>6</sub> (0.35 mmol) into 2 mL of dry hexane and

carefully add 1.4 mL of 2.5 M n-butyl lithium (3.5 mmol). Seal and stir at room temperature for 3–5 days. The lithiated product was filtered under an argon atmosphere via gravity filtration, rinsed with excess hexane, and stored under argon prior to optical microscopy and PXRD analysis. Subsequent reaction of lithiated bismuth tungstate in water is accomplished by bath sonication for 1–2 h.

#### *Characterization details*

PXRD patterns were collected using a Bruker D8-Advance diffractometer (Co-K $\alpha$  radiation source) operated at 40 mA and 40 kV. All samples were collected from 3–75  $2\theta$  with a rate of 0.1 seconds per step. Samples were prepared by pressing the dry powders into an aluminum mount.

Electron microscopy samples were prepared with samples dispersed in isopropanol using bath sonication. TEM images were attained using a FEI Tecnai 20 (200 keV) microscope. SEM samples were drop cast onto gold-coated silicon wafers, and images were collected with a FEI Inspect F field emission gun scanning electron microscope operated at 10 keV.

UV-vis absorption spectra were collected using a Cary 50 UV-visible spectrometer, with a scanning range of 200 to 1100 nm. UV-vis diffuse reflectance spectra were collected with a Shimadzu 2450 UV-vis spectrophotometer outfitted with a integration-sphere detector. Diffuse reflectance samples consisted of powders packed into a 1  $\times$  2  $\times$  4 mm sample holder.

## References

1. B. Aurivillius, *Ark. Kemi*, 1952, 5, 39–47.
2. Y. Noguchi and M. Miyayama, in *Lead-Free Piezoelectrics*, ed. S. Priya and S. Nahm, Springer, New York, 2012, pp. 405–459.
3. Y. Yoneda, S. Kohara, H. Takeda and T. Tsurumi, *Jpn. J. Appl. Phys.*, 2012, 51, 09LE06.
4. C. Zhang and Y. Zhu, *Chem. Mater.*, 2005, 17, 3537–3545.
5. L. Zhang, H. Wang, Z. Chen, P. K. Wong and J. Liu, *Appl. Catal., B*, 2011, 106, 1–13.
6. J. Tang, Z. Zou and J. Ye, *Catal. Lett.*, 2004, 92, 53–56.
7. H. Takeda, J. S. Han, M. Nishida, T. Shiosaki, T. Hoshina and T. Tsurumi, *Solid State Commun.*, 2010, 150, 836–839.
8. L. Zhang, W. Wang, Z. Chen, L. Zhou, H. Xu and W. Zhu, *J. Mater. Chem.*, 2007, 17, 2526–2532 RSC .
9. J. Xia, H. Li, Z. Luo, H. Xu, K. Wang, S. Yin and Y. Yan, *Mater. Chem. Phys.*, 2010, 121, 6–9.
10. H. Fu, L. Zhang, W. Yao and Y. Zhu, *Appl. Catal., B*, 2006, 66, 100–110.
11. Y. Li, J. Liu, X. Huang and G. Li, *Cryst. Growth Des.*, 2007, 7, 1350–1355.
12. L. Zhang, W. Wang, L. Zhou and H. Xu, *Small*, 2007, 3, 1618–1625.
13. M. Shang, W. Wang, S. Sun, L. Zhou and L. Zhang, *J. Phys. Chem. C*, 2008, 112, 10407–10411.
14. L. Wu, J. Bi, Z. Li, X. Wang and X. Fu, *Catal. Today*, 2008, 131, 15–20.
15. D. Ma, S. Huang, W. Chen, S. Hu, F. Shi and K. Fan, *J. Phys. Chem. C*, 2009, 113, 4369–4374.

16. C. Xu, X. Wei, Z. Ren, Y. Wang, G. Xu, G. Shen and G. Han, *Mater. Lett.*, 2009, 63, 2194–2197.
17. C. Xu, X. Wei, Y. Guo, H. Wu, Z. Ren, G. Xu, G. Shen and G. Han, *Mater. Res. Bull.*, 2009, 44, 1635–1641.
18. Y. Zhou, K. Vuille, A. Heel and G. R. Patzke, *Z. Anorg. Allg. Chem.*, 2009, 635, 1848–1855.
19. C. Wang, H. Zhang, F. Li and L. Zhu, *Environ. Sci. Technol.*, 2010, 44, 6843–6848.
20. Y. Tian, G. Hua, W. Xu, N. Li, M. Fang and L. Zhang, *J. Alloys Compd.*, 2011, 509, 724–730.
21. J.-C. Champarnaud-Mesjard, B. Frit and A. Watanabe, *J. Mater. Chem.*, 1999, 9, 1319–1322 RSC .
22. R. E. Schaak and T. E. Mallouk, *Chem. Commun.*, 2002, 706–707 RSC .
23. M. R. Waller, T. K. Townsend, J. Zhao, E. M. Sabio, R. L. Chamousis, N. D. Browning and F. E. Osterloh, *Chem. Mater.*, 2012, 24, 698–704.
24. Y. Shigesato, *Jpn. J. Appl. Phys., Part 1*, 1991, 30, 1457–1462.
25. T. He and J. Yao, *J. Mater. Chem.*, 2007, 17, 4547–4557 RSC .
26. K. Fukuda, K. Akatsuka, Y. Ebina, R. Ma, K. Takada, I. Nakai and T. Sasaki, *ACS Nano*, 2008, 2, 1689–1695.
27. C. G. Granqvist, *Solid State Ionics*, 1992, 53–56(1), 479–489.
28. Karuppasamy and A. Subrahmanyam, *Thin Solid Films*, 2007, 516, 175–178.
29. G. A. Niklasson and C. G. Granqvist, *J. Mater. Chem.*, 2007, 17, 127–156.
30. K. Bange and T. Gambke, *Adv. Mater.*, 1990, 2, 10–16.
31. K. Fukuda, K. Akatsuka, Y. Ebina, M. Osada, W. Sugimoto, M. Kimura and T. Sasaki, *Inorg. Chem.*, 2012, 51, 1540–1543.

32. K. Okada, F. Marumo and S. Iwai, *Acta Crystallogr., Sect. B: Struct. Crystallogr. Cryst. Chem.*, 1978, 34, 50–54.
33. N. Henry, M. Evain, P. Deniard, S. Jobic, F. Abraham and O. Mentre, *Z. Naturforsch., B: Chem. Sci.*, 2005, 60, 322–327.
34. K. S. Knight, *Mineral. Mag.*, 1992, 56, 399–409.
35. L. Xie, J. Wang, Y. Hu, Z. Zheng, S. Weng, P. Liu, X. Shi and D. Wang, *Mater. Chem. Phys.*, 2012, 136, 309–312.
36. Y. Zhou, E. Antonova, W. Bensch and G. R. Patzke, *Nanoscale*, 2010, 2, 2412–2417 RSC .
37. M. Maczka, L. Macalik, K. Hermanowicz, L. Kepinski and P. Tomaszewski, *J. Raman Spectrosc.*, 2010, 41, 1059–1066.
38. K. P. Mann, E. M. P. Steinmiller and S. E. Skrabalak, *Dalton Trans.*, 2012, 41, 7939–7945 RSC .
39. S. Mahanty and J. Ghose, *Mater. Lett.*, 1991, 11, 254–256.
40. Y. Huang, Z. Ai, W. Ho, M. Chen and S. Lee, *J. Phys. Chem. C*, 2010, 114, 6342–6349.
41. L. Zhou, M. Yu, J. Yang, Y. Wang and C. Yu, *J. Phys. Chem. C*, 2010, 114, 18812–18818.
42. C. Bhattacharya, H. C. Lee and A. J. Bard, *J. Phys. Chem. C*, 2013, 117, 9633–9640.
43. M. Jakob, H. Levanon and P. V. Kamat, *Nano Lett.*, 2003, 3, 353–358.
44. Bedja, S. Hotchandani and P. V. Kamat, *J. Phys. Chem.*, 1993, 97, 11064–11070.
45. M. T. Nenadovic, T. Rajh, O. I. Micic and A. J. Nozik, *J. Phys. Chem.*, 1984, 88, 5827–5830.
46. Y. Shimakawa and Y. Kubo, in *MRS Proceedings*, Cambridge Univ Press, 2000.
47. D. Guo and M. S. Whittingham, *Int. J. Mod. Phys. B*, 1993, 7, 4145–4164.
48. N. Kumagai, A. Yu and H. Yashiro, *Solid State Ionics*, 1997, 98, 159–166.
49. C. O. Avellaneda, *Mater. Sci. Eng., B*, 2007, 138, 123–127.

50. F. E. Longoria Rodríguez and A. Martínez-de la Cruz, *Mater. Res. Bull.*, 2001, 36, 1195–1204.
51. Wu, F. Duan, Y. Zheng and Y. Xie, *J. Phys. Chem. C*, 2007, 111, 12866–12871.
52. J.-Y. Kim, I. Chung, J.-H. Choy and G.-S. Park, *Chem. Mater.*, 2001, 13, 2759–2761.
53. D. W. Murphy, F. J. Di Salvo, G. W. Hull and J. V. Waszczak, *Inorg. Chem.*, 1976, 15, 17–21.
54. P. Joensen, R. F. Frindt and S. R. Morrison, *Mater. Res. Bull.*, 1986, 21, 457–461.
55. Bange, *Sol. Energy Mater. Sol. Cells*, 1999, 58, 1–131.
56. V. Chevallier, G. Nihoul and V. Madigou, *J. Solid State Chem.*, 2008, 181, 439–449.

**CHAPTER 3**  
**BISMUTH METAL OXIDE NANOSHEETS FROM A BISMUTH BORATE**  
**NANOSHEET TEMPLATE**

Timothy R. Pope, Abigail Bruning, Gregory Neher, and Tina T. Salguero. *In preparation for the Journal of Materials Chemistry C.*

**Abstract**

Nano-structured bismuth tungstate ( $\text{Bi}_2\text{WO}_6$ ) was prepared by hydrothermal synthesis using a synthesized bismuth hydroxyl borate ( $\text{Bi}_2\text{O}_2[\text{BO}_2(\text{OH})]$ ) nanosheet precursor as the bismuth oxide source. The hydrothermal synthesis of the  $\text{Bi}_2\text{O}_2[\text{BO}_2(\text{OH})]$  nanosheet precursor was found to be highly dependent on the solution pH and stoichiometric ratio of the starting materials.  $\text{Bi}_2\text{O}_2[\text{BO}_2(\text{OH})]$  nanosheets with thicknesses of 20–40 nm and lateral dimensions up to a micron were obtained using a 4:1 B:Bi stoichiometric ratio and reaction at a temperature of 180 °C and a pH of 8. The bismuth hydroxyl borate nanosheet precursor was then used in the hydrothermal synthesis of  $\text{Bi}_2\text{WO}_6$  along with either a soluble tungsten precursor ( $\text{Na}_2\text{WO}_4$ ), which produced aggregates of large nanoplatelets, or a nanosheet precursor ( $\text{Cs}_4\text{W}_{11}\text{O}_{36}^{2-}$ ), which produced nanosheets with lateral dimensions in the micrometer range and thicknesses of 5–40 nm.

## Introduction

Metal oxides have been widely studied for their catalytic abilities. In particular, bismuth tungstate ( $\text{Bi}_2\text{WO}_6$ ) acts as a photocatalyst to degrade organic pollutants under visible light and also as a photocatalyst for the oxygen evolution reaction.<sup>1-6</sup> The photocatalytic ability of  $\text{Bi}_2\text{WO}_6$  was shown to rely on the material having high crystallinity, whereas, amorphous  $\text{Bi}_2\text{WO}_6$  displays negligible photocatalytic activity.<sup>4</sup> Furthermore, the material's size influences the catalytic properties; for example, a reduction in the thickness leads to a reduction in bandgap, meaning less energy is required to form excitons, which further enhances the photocatalytic activity.<sup>3, 7</sup> In fact, the photodegradation of Rhodamine B is 8–10 times higher when using nanoscale  $\text{Bi}_2\text{WO}_6$  rather than the bulk material.<sup>8</sup>

Furthermore, stable nanosheet dispersions are highly desirable because they can lead to facile solution catalysis due to the increase in surface area and, thus, surface reactive sites. Nanosheet dispersions also allow for the deposition of thin films of catalyst material onto solid substrates, which is especially useful in cases where the thin films formed by chemical vapor deposition are relatively thick (microns).<sup>9</sup> Therefore, it is of interest to develop a facile method for the formation of solution processable, nanostructured  $\text{Bi}_2\text{WO}_6$ . Solvothermal growth methods in aqueous media at low temperatures are inexpensive and scalable, whereas top down approaches are difficult for such covalently bound layered materials in contrast to van der Waals materials. Hence, we focus on solvothermal methods for the formation of nanosheets of  $\text{Bi}_2\text{WO}_6$ .

Principally, we are interested in  $\text{Bi}_2\text{WO}_6$  nanosheets that are only a few monolayers thick and have lateral dimensions in the micrometer range, in preference over other nanoscale morphologies due to the potential enhancement of photooxidation activity. Photooxidation occurs when excitons are generated upon exposure to light, and the considerably decreased thickness of

nanosheets greatly lowers the recombination rate, which results in enhanced photocatalytic activity.<sup>10</sup> In  $\text{Bi}_2\text{WO}_6$ , exciton generation occurs primarily at bismuth and oxide sites. Because  $\text{Bi}_2\text{WO}_6$  has a layered structure consisting of alternating  $[\text{Bi}_2\text{O}_2]^{2+}$  and  $[\text{WO}_4]^{2-}$  layers (Figure 3.1), extending the crystal along the  $(0k0)$  lattice planes, where  $[\text{Bi}_2\text{O}_2]^{2+}$  is the terminal layer, increases the number of exciton generation sites and provides efficient photooxidation.<sup>10</sup>

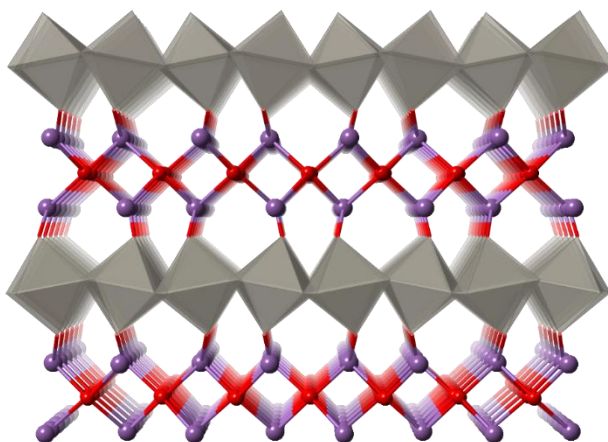


**Figure 3.1.** Structure of  $\text{Bi}_2\text{WO}_6$  looking along the  $(0k0)$  lattice plane with alternating layers of  $[\text{Bi}_2\text{O}_2]^{2+}$  and  $[\text{WO}_4]^{2-}$  arranged in the simplest form of the Aurivillius structure.

$\text{Bi}_2\text{WO}_6$  can be synthesized in bulk by the solid state reaction of  $\text{Bi}_2\text{O}_3$  and  $\text{WO}_3$ .<sup>1, 6</sup> Unlike some layered materials, like transition metal dichalcogenides, bulk  $\text{Bi}_2\text{WO}_6$  crystals are not easily exfoliated into nanosheets. Nanoscale  $\text{Bi}_2\text{WO}_6$  has previously been synthesized directly under hydrothermal conditions using an acidic precursor solution of  $\text{Na}_2\text{WO}_4$  and  $\text{Bi}(\text{NO}_3)_3$ ; however, this method typically produces microscale flower-like clusters made up of aggregated nanoplatelets.<sup>11, 12</sup> Zhu and coworkers used hydrothermal synthesis to form square nanoparticles of  $\text{Bi}_2\text{WO}_6$  with lateral dimensions of 20–50 nm.<sup>2, 13</sup> They hypothesized that lateral growth dominated over increased layer growth due to the chemical potential of the tungsten oxide surface being higher than that of the bismuth oxide surface; because the tungsten surface exists along the

*a*- and *b*-axes, the (*h*00) and (0*k*0) facets displayed higher growth rates.<sup>2</sup> Sun et al. also synthesized oriented Bi<sub>2</sub>WO<sub>6</sub> by adjusting the pH of the reaction system to 4.8 during hydrothermal synthesis, which produced a nano-morphology with thicknesses of 3–4 nm and lateral dimensions of ~100 nm.<sup>10</sup> A variety of other nano-morphologies have been formed by alternative methods such as calcination of amorphous precursors, ultrasonic spray pyrolysis, refluxing with colloidal templates, and microwave assisted solvothermal synthesis,<sup>14-17</sup> though none of these methods produce free-standing nanosheets.

Detailed in Chapter II, we used a nanosheet precursor in the hydrothermal synthesis of Bi<sub>2</sub>WO<sub>6</sub> to directly synthesize isolable nanosheets with thicknesses of 5–15 nm and lateral dimensions of 1–2 μm.<sup>18</sup> By tracking the composition and morphology over the course of the reaction, we found that using a Cs<sub>4</sub>W<sub>11</sub>O<sub>36</sub><sup>2-</sup> nanosheet precursor for the source of reactive tungsten oxide produces a templating effect which leads to nanosheets of large lateral dimension. We concluded that the metal nanosheet precursor is the major controlling factor in the formation of bismuth metal oxide nanosheets. In this report, we again turn to a nanosheet precursor to form Bi<sub>2</sub>WO<sub>6</sub> nanosheets—this time altering the bismuth source to provide a lateral template and to further elucidate the templating effect. First, the synthesis of Bi<sub>2</sub>WO<sub>6</sub> was carried out using a Bi<sub>2</sub>O<sub>2</sub>[BO<sub>2</sub>(OH)] nanosheet precursor and Na<sub>2</sub>WO<sub>6</sub>, which gave aggregates of thick platelets that were distinct from the flower-like morphologies obtained previously from Bi(NO<sub>3</sub>)<sub>3</sub> and Na<sub>2</sub>WO<sub>6</sub>. Then, the synthesis was also performed using two reactive nanosheet precursors, Bi<sub>2</sub>O<sub>2</sub>[BO<sub>2</sub>(OH)] and Cs<sub>4</sub>W<sub>11</sub>O<sub>36</sub><sup>2-</sup>, which produced free standing Bi<sub>2</sub>WO<sub>6</sub> nanosheets with lateral dimensions in the micrometer range and thicknesses of 5–40 nm.

## Results and Discussion

### *Synthesis of $\text{Bi}_2\text{O}_2[\text{BO}_2(\text{OH})]$ Precursor*

Bismuth hydroxyl borate ( $\text{Bi}_2\text{O}_2[\text{BO}_2(\text{OH})]$ ) has been investigated as a layered photocatalyst for the degradation of Rhodamine B under UV irradiation.<sup>19, 20</sup> However, we are more interested in this material's potential to act as a bismuth oxide source in the hydrothermal synthesis of  $\text{Bi}_2\text{WO}_6$ . As shown in Figure 3.2,  $\text{Bi}_2\text{O}_2[\text{BO}_2(\text{OH})]$  has a layered structure consisting of alternating  $[\text{BO}_2(\text{OH})]^{2-}$  and  $(\text{Bi}_2\text{O}_2)^{2+}$  layers arranged in a Sillén-like configuration similar to bismuth subcarbonate ( $\text{Bi}_2\text{O}_2\text{CO}_3$ ).<sup>20</sup> This structure is also similar to that of  $\text{Bi}_2\text{WO}_6$ , where the  $[\text{BO}_2(\text{OH})]^{2-}$  layer is replaced by a layer of corner-shared tungsten oxide octahedra. Due to the similarity of the  $(\text{Bi}_2\text{O}_2)^{2+}$  layer in  $\text{Bi}_2\text{O}_2[\text{BO}_2(\text{OH})]$  and  $\text{Bi}_2\text{WO}_6$ , we hypothesized that  $\text{Bi}_2\text{O}_2[\text{BO}_2(\text{OH})]$  can act as a layered template to promote lateral growth.

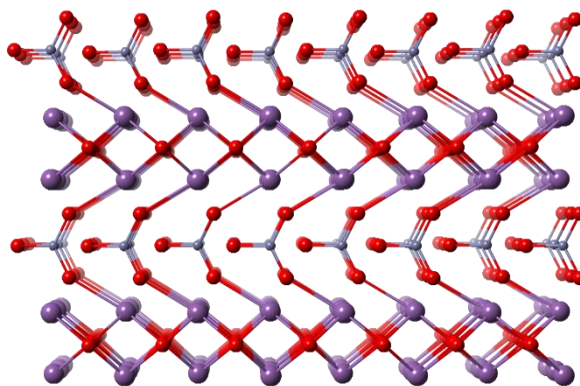


**Figure 3.2.** Structure of  $\text{Bi}_2\text{O}_2[\text{BO}_2(\text{OH})]$  with  $[\text{BO}_2(\text{OH})]^{2-}$  and  $(\text{Bi}_2\text{O}_2)^{2+}$  layers arranged in a Sillén-like configuration, looking along the  $(0k0)$  lattice plane.

As detailed in Chapter II, for the synthesis of  $\text{Bi}_2\text{WO}_6$  nanosheets, bismuth nitrate ( $\text{Bi}(\text{NO}_3)_3$ ) dissolved in nitric acid was used as the bismuth source.<sup>18</sup> Cesium tungstate ( $\text{Cs}_4\text{W}_{11}\text{O}_{36}^{2-}$ ) nanosheets were used as the tungsten oxide source and provided a template for generating the two dimensional structure of the final product. In this subsequent work, we use

sodium tungstate ( $\text{Na}_2\text{WO}_4$ ) as the powder precursor and  $\text{Bi}_2\text{O}_2[\text{BO}_2(\text{OH})]$  as the nanostructured precursor. In addition, the synthesis was also accomplished using nanosheets for both precursors ( $\text{Bi}_2\text{O}_2[\text{BO}_2(\text{OH})]$  and  $\text{Cs}_4\text{W}_{11}\text{O}_{36}^{2-}$ ).

Cong et al. synthesized  $\text{Bi}_2\text{O}_2[\text{BO}_2(\text{OH})]$  for the first time in 2011 using hydrothermal synthesis techniques.<sup>21</sup> In their synthesis,  $\text{H}_3\text{BO}_3$  and  $\text{Bi}_2\text{O}_3$  were ground together, dissolved in water, and reacted at 220 °C for 3 days, hydrothermally. They found that the product depended on the amount of water added, with  $\text{Bi}_2\text{O}_2[\text{BO}_2(\text{OH})]$  always being formed with a mixture of either  $\text{Bi}_2\text{O}_2[\text{B}_3\text{O}_5(\text{OH})]$  or  $\text{Bi}_4\text{B}_2\text{O}_9$ . Using PXRD to determine the crystal structure,  $\text{Bi}_2\text{O}_2[\text{BO}_2(\text{OH})]$  was found to consist of alternating layers of  $[\text{Bi}_2\text{O}_2]^{2+}$  and  $[\text{BO}_2(\text{OH})]^{2-}$ . Huang et al. took a different route to synthesize  $\text{Bi}_2\text{O}_2[\text{BO}_2(\text{OH})]$  by utilizing a  $\text{Bi}_4\text{B}_2\text{O}_9$  precursor made by sintering ground  $\text{H}_3\text{BO}_3$  and  $\text{Bi}_2\text{O}_3$  at 600 °C.<sup>20</sup>  $\text{Bi}_2\text{O}_2[\text{BO}_2(\text{OH})]$  was then prepared from the precursor by hydrothermal synthesis at 200 °C for 24 hours. This method, however, did not produce a nanoscale product but instead clusters of micrometer-sized platelets. Zhang et al. followed these works and fabricated  $\text{Bi}_2\text{O}_2[\text{BO}_2(\text{OH})]$  nanosheets that showed enhanced photocatalytic activity using an approach similar to Cong et al..<sup>19</sup> In their approach,  $\text{H}_3\text{BO}_3$  and  $\text{Bi}(\text{NO}_3)_3 \cdot 5\text{H}_2\text{O}$  were first hydrolyzed by altering the pH of the solution, then reacted in the presence of a polyvinylpyrrolidone surfactant under hydrothermal conditions at 120 °C for 12 hours. The  $\text{Bi}_2\text{O}_2[\text{BO}_2(\text{OH})]$  nanosheets were around 400 nm in lateral dimension with tunable thicknesses of 15–60 nm. Zhang et al. hypothesized that the formation of nanosheets was in part due to the polyvinylpyrrolidone surfactant absorbing on the surface and restricting growth along the  $\langle 010 \rangle$  direction.<sup>19</sup>

Following the procedure of Zhang et al., we synthesized  $\text{Bi}_2\text{O}_2[\text{BO}_2(\text{OH})]$  nanosheets by the hydrothermal synthesis of  $\text{H}_3\text{BO}_3$  and  $\text{Bi}(\text{NO}_3)_3$ . However, several modifications had to be

made from the original procedure to form the intended product and morphology: (1) the stoichiometry was altered to 4:1 B:Bi, (2) the pH was restricted to 8 rather than 13 during hydrolysis, and (3) no surfactant was included in the hydrothermal synthesis.

Specifically,  $\text{Bi}_2\text{O}_2[\text{BO}_2(\text{OH})]$  nanosheets were prepared by mixing solutions of boric acid in deionized water and bismuth nitrate in 1 M  $\text{HNO}_3$  in a 4:1 molar ratio of  $\text{H}_3\text{BO}_3$  to  $\text{Bi}(\text{NO}_3)_3 \cdot 5\text{H}_2\text{O}$ . In a typical experiment, 0.4913 g (1 mmol) of  $\text{Bi}(\text{NO}_3)_3 \cdot 5\text{H}_2\text{O}$  was dissolved in 7.5 mL of 1 M  $\text{HNO}_3$ . A second solution of 0.247 g (4 mmol)  $\text{H}_3\text{BO}_3$  in 15 mL DI water was added to the bismuth nitrate solution. The pH of the combined solution was then raised from  $\sim 0.5$  to 2 then to 5 and finally to 8 through dropwise addition of 5 M  $\text{NaOH}$  (stirring for 10 minutes at each pH value). The solution was then transferred to a 45 mL Teflon-lined autoclave and heated in an oven to 180 °C for 8 h. After hydrothermal treatment, the resultant white solid was rinsed with water and isopropyl alcohol then vacuum dried at 50 °C to obtain  $\text{Bi}_2\text{O}_2[\text{BO}_2(\text{OH})]$  with an isolated yield of 0.245 g (0.481 mmol, 95.3 % yield).

Before submitting the solution to hydrothermal synthesis, both starting materials are first hydrolysed by altering the pH.<sup>19</sup> When the two starting materials are dissolved together, the pH of the solution is  $\sim 0.5$ . Upon increasing the pH to 2,  $\text{Bi}(\text{NO}_3)_3$  hydrolyzes to precipitate  $\text{BiONO}_3$  platelets or needles, which is seen by liquid crystalline pearlescent distortions in the solution. The pH is then further increased to 6.5–7, stirred for 10 more minutes, then increased again to 8 and stirred for 10 minutes, where  $\text{H}_3\text{BO}_3$  hydrolyzes to  $[\text{BO}_2(\text{OH})]^{2-}$ . This solution is then added to the Teflon-line autoclave to undergo hydrothermal synthesis. Upon heating, an ion exchange reaction occurs between the two hydrolysis products to form the final  $\text{Bi}_2\text{O}_2[\text{BO}_2(\text{OH})]$  structure.

The pH of the solution during hydrothermal synthesis dramatically influences the identity of the final product. The powder XRD patterns for the product of hydrothermal synthesis at a pH of 7, 8, and 13 are given in Figure 3.3. At pH 7,  $[\text{Bi}_6\text{O}_6(\text{OH})_3](\text{NO}_3)_3 \cdot 1.5\text{H}_2\text{O}$  is formed. Previously, Christensen et al. synthesized  $[\text{Bi}_6\text{O}_6(\text{OH})_3](\text{NO}_3)_3 \cdot 1.5\text{H}_2\text{O}$  under hydrothermal conditions from bismuth nitrate at a temperature of  $\sim 190^\circ\text{C}$  and were able to obtain a powder XRD pattern of the product.<sup>22</sup> The crystal structure of  $[\text{Bi}_6\text{O}_6(\text{OH})_3](\text{NO}_3)_3 \cdot 1.5\text{H}_2\text{O}$  is given in Figure 3.3. At pH 8,  $\text{Bi}_2\text{O}_2[\text{BO}_2(\text{OH})]$  is formed preferentially. As the pH is further increased,  $\alpha\text{-Bi}_2\text{O}_3$  begins to form. When the pH is increased to 13, only  $\alpha\text{-Bi}_2\text{O}_3$  is formed.

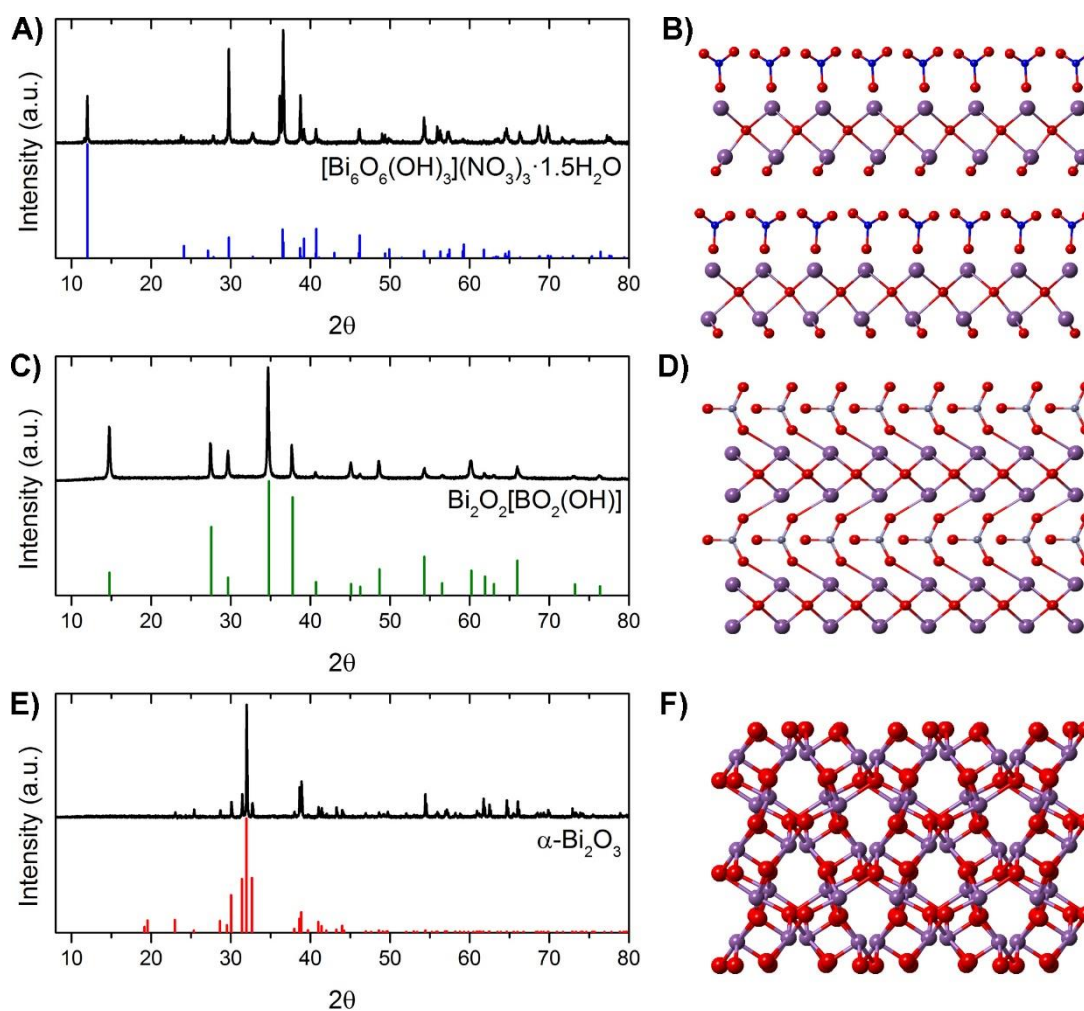


**Figure 3.3.** Powder XRD patterns, with reference patterns, and crystals structures of the products of the hydrothermal synthesis of  $\text{H}_3\text{BO}_3$  and  $\text{Bi}_3(\text{NO}_3)_3$  at  $180^\circ\text{C}$  for 8 hours and at A,B) pH 7 ( $[\text{Bi}_6\text{O}_6(\text{OH})_3](\text{NO}_3)_3 \cdot 1.5\text{H}_2\text{O}$ ), C,D) pH 8 ( $\text{Bi}_2\text{O}_2[\text{BO}_2(\text{OH})]$ ), and E,F) pH 13 ( $\alpha\text{-Bi}_2\text{O}_3$ ).

During hydrothermal synthesis at pH 8, the growth of  $\text{Bi}_2\text{O}_2[\text{BO}_2(\text{OH})]$  nanosheets was tracked by examining the powder XRD pattern of samples reacted at various times (Figure 3.4). The product was collected by centrifuging the reaction solution at high rpm to precipitate the product, removing the supernatant, centrifuging again first with water then with isopropanol, and finally dried in a  $50\text{ }^\circ\text{C}$  vacuum oven. As shown by the peaks in the XRD pattern at  $12$  and  $37\text{ }2\theta$  (denoted by \* in Figure 3.4a), after 1 hour the intermediate  $[\text{Bi}_6\text{O}_6(\text{OH})_3](\text{NO}_3)_3 \cdot 1.5\text{H}_2\text{O}$  is formed. This material was observed as an intermediate in the hydrothermal synthesis of  $\text{Bi}_2\text{WO}_6$  from  $\text{Bi}(\text{NO}_3)_3$  as detailed in Chapter II,<sup>18</sup> as well as in a previous report by Xie et al., where  $[\text{Bi}_6\text{O}_6(\text{OH})_3](\text{NO}_3)_3 \cdot 1.5\text{H}_2\text{O}$  was formed under similar hydrothermal conditions from  $\text{Bi}(\text{NO}_3)_3$ .<sup>23</sup>  $[\text{Bi}_6\text{O}_6(\text{OH})_3](\text{NO}_3)_3 \cdot 1.5\text{H}_2\text{O}$  production reaches a maximum at 3 hours, then declines as  $\text{Bi}_2\text{O}_2[\text{BO}_2(\text{OH})]$  nanosheets begin to form, shown by the peaks at  $15$  and  $35\text{ }2\theta$ . After 8 hours all  $[\text{Bi}_6\text{O}_6(\text{OH})_3](\text{NO}_3)_3 \cdot 1.5\text{H}_2\text{O}$  is consumed and the synthesis of  $\text{Bi}_2\text{O}_2[\text{BO}_2(\text{OH})]$  nanosheets is complete.

The homogeneity and morphology of the final  $\text{Bi}_2\text{O}_2[\text{BO}_2(\text{OH})]$  product can be controlled by altering the stoichiometry of  $\text{H}_3\text{BO}_3$  to  $\text{Bi}_3(\text{NO}_3)_3$ . Figure 3.5 shows SEM images of the different morphologies obtained at different stoichiometric ratios of B:Bi, while Figure 3.6 shows the powder XRD pattern of the different products.. A low stoichiometric ratio of 2:1 B:Bi produces mainly the  $[\text{Bi}_6\text{O}_6(\text{OH})_3](\text{NO}_3)_3 \cdot 1.5\text{H}_2\text{O}$  intermediate, because there is not enough boron present to drive the ion exchange reaction to completion. A 4:1 ratio provides enough boron to drive the ion exchange reaction and results in  $\text{Bi}_2\text{O}_2[\text{BO}_2(\text{OH})]$  nanosheets. An 8:1 ratio also produces  $\text{Bi}_2\text{O}_2[\text{BO}_2(\text{OH})]$  but in a mixture of nanosheets and platelet morphologies; in general, the morphology is smaller and thicker at 8:1 ratios with some nanosheets present as compared with 4:1 ratios. At 15:1 large platelets are formed, as seen by SEM, and also a secondary crystal

structure (bismuth oxide) emerges in the XRD pattern. The 4:1 B:Bi stoichiometric ratio tends to produce the largest and most uniform  $\text{Bi}_2\text{O}_2[\text{BO}_2(\text{OH})]$  nanosheets. Therefore, for subsequent experiments  $\text{Bi}_2\text{O}_2[\text{BO}_2(\text{OH})]$  nanosheets were made using the 4:1 B:Bi ratio.

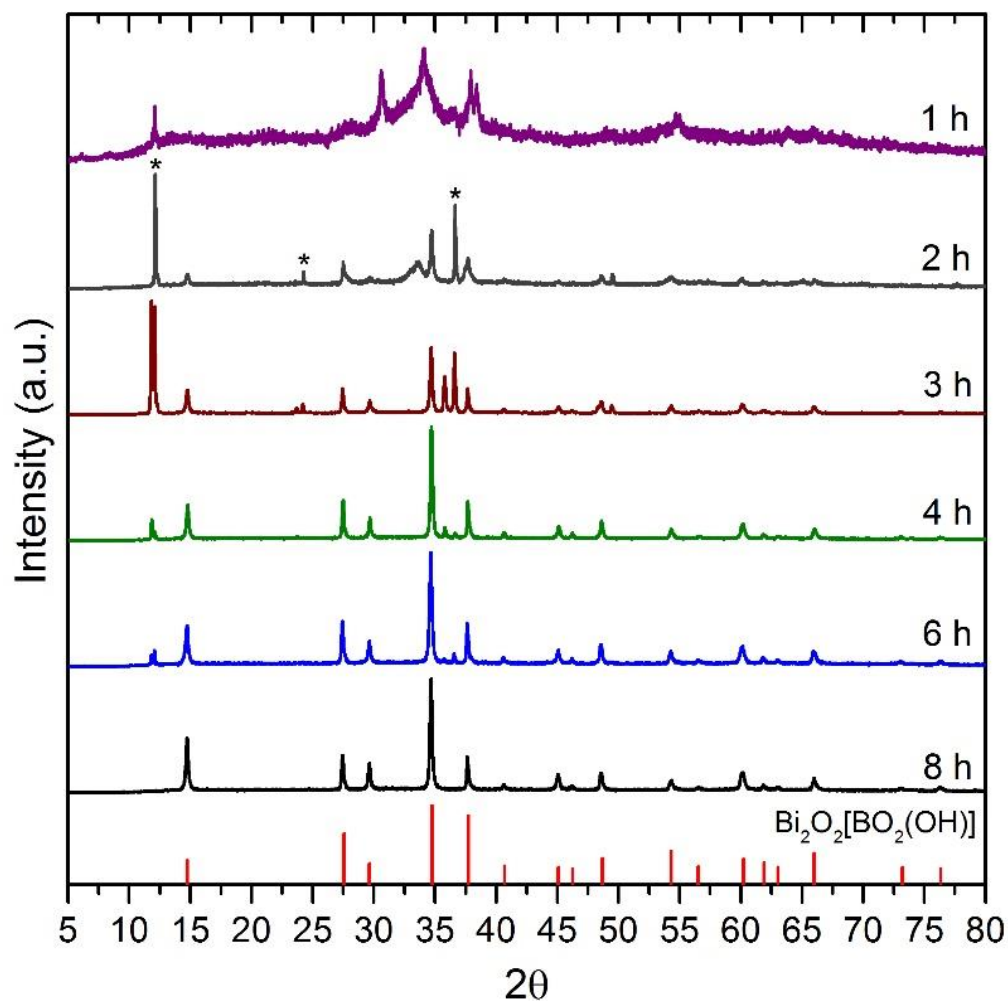


**Figure 3.4.** Powder XRD patterns of samples taken from the hydrothermal synthesis of  $\text{Bi}_2\text{O}_2[\text{BO}_2(\text{OH})]$  at various times. The \* denotes the  $[\text{Bi}_6\text{O}_6(\text{OH})_3](\text{NO}_3)_3 \cdot 1.5\text{H}_2\text{O}$  intermediate.

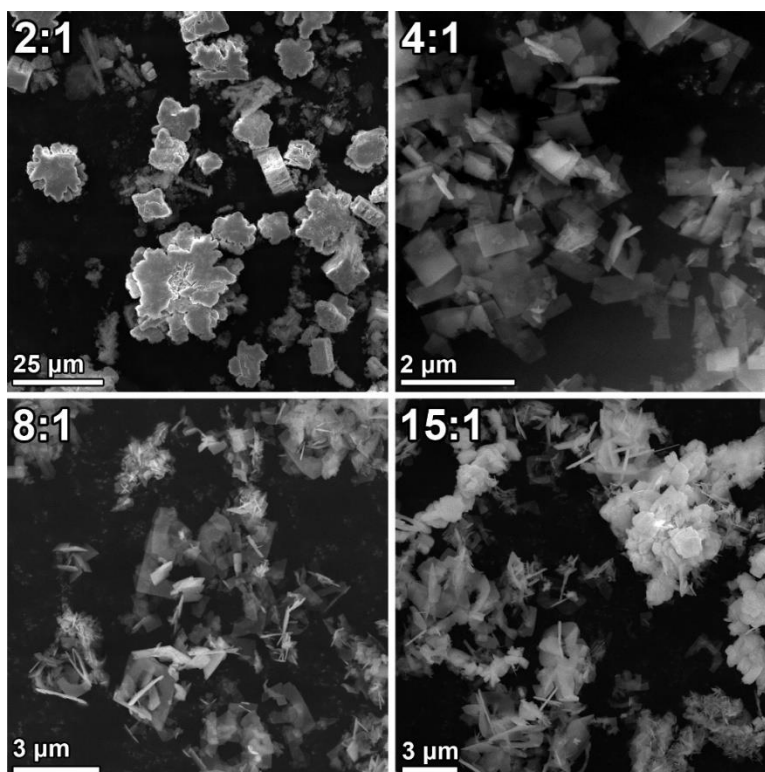


**Figure 3.5.** SEM images of the different morphologies obtained at B:Bi stoichiometric ratios of 2:1, 4:1, 8:1, and 15:1. The 4:1 ratio produced the largest and most uniform nanosheet morphology.

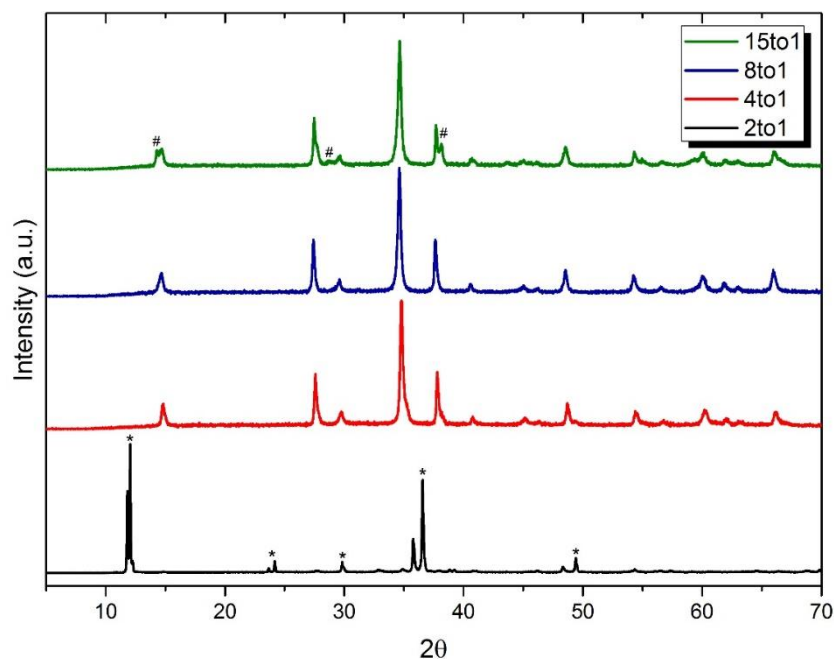


**Figure 3.6.** Powder XRD patterns of the products obtained at B:Bi stoichiometric ratios of 2:1, 4:1, 8:1, and 15:1. The 2:1 and 15:1 ratios, specifically, show peaks corresponding to other materials besides  $\text{Bi}_2\text{O}_2[\text{BO}_2(\text{OH})]$ . The \* denotes the  $[\text{Bi}_6\text{O}_6(\text{OH})_3](\text{NO}_3)_3 \cdot 1.5\text{H}_2\text{O}$  intermediate. The peaks marked with # correspond to bismuth oxide.

The resultant  $\text{Bi}_2\text{O}_2[\text{BO}_2(\text{OH})]$  can clearly be characterized as nanosheets. SEM and TEM images show that the nanosheets are up to a micrometer in lateral dimension, while AFM analysis shows that the nanosheets are 20–40 nm thick (Figure 3.7). Electron diffraction taken during SEM analysis, matches the simulated diffraction pattern of  $\text{Bi}_2\text{O}_2[\text{BO}_2(\text{OH})]$  looking down the b-axis, which signifies that the nanosheets preferentially grow along the (0*k*0) axis. Diffuse reflectance data, shown in Figure 3.8, estimates the bandgap at 2.95 eV, which is comparable to the 2.85 eV bandgap reported previously.<sup>20</sup>

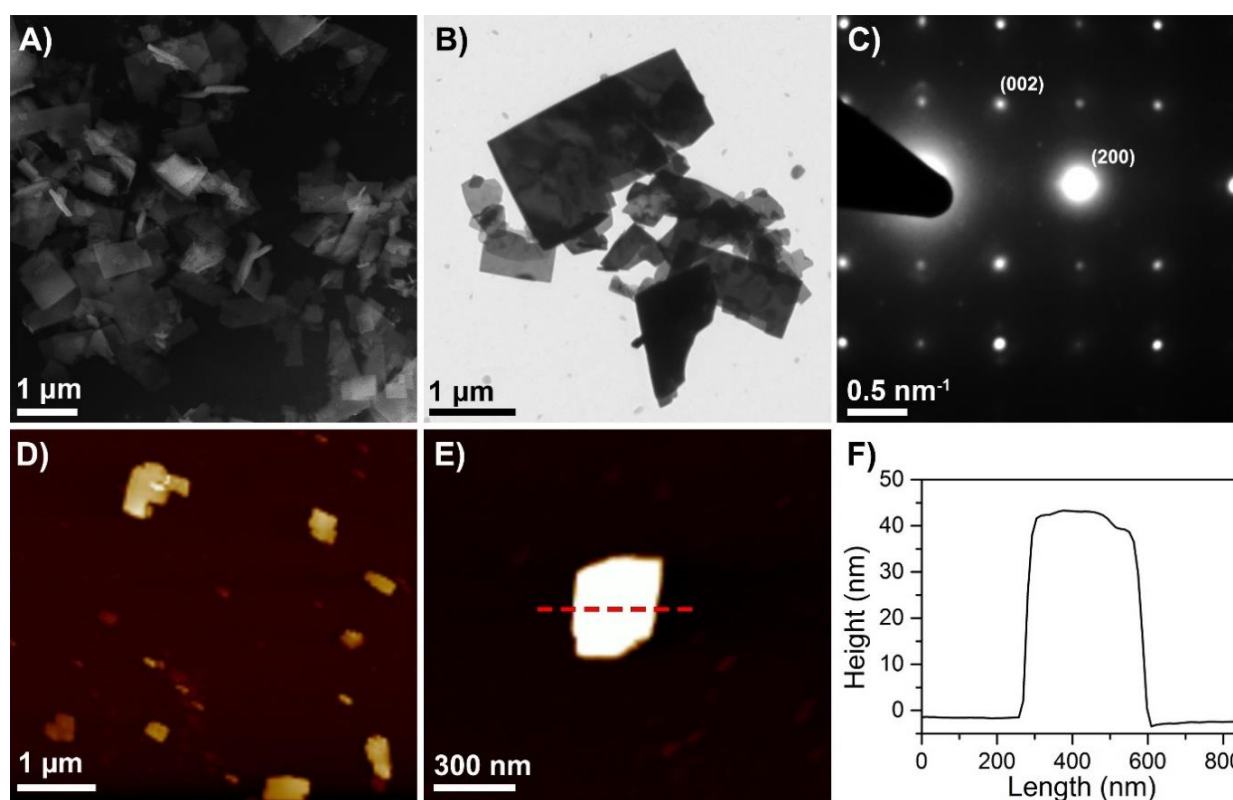


**Figure 3.7.** A) TEM image, B) SEM image, C) electron diffraction pattern, D–E) AFM images, and F) height profile of  $\text{Bi}_2\text{O}_2[\text{BO}_2(\text{OH})]$  nanosheets synthesized from a 4:1 ratio of  $\text{H}_3\text{BO}_3:\text{Bi}_3(\text{NO}_3)_3$  at pH 8.

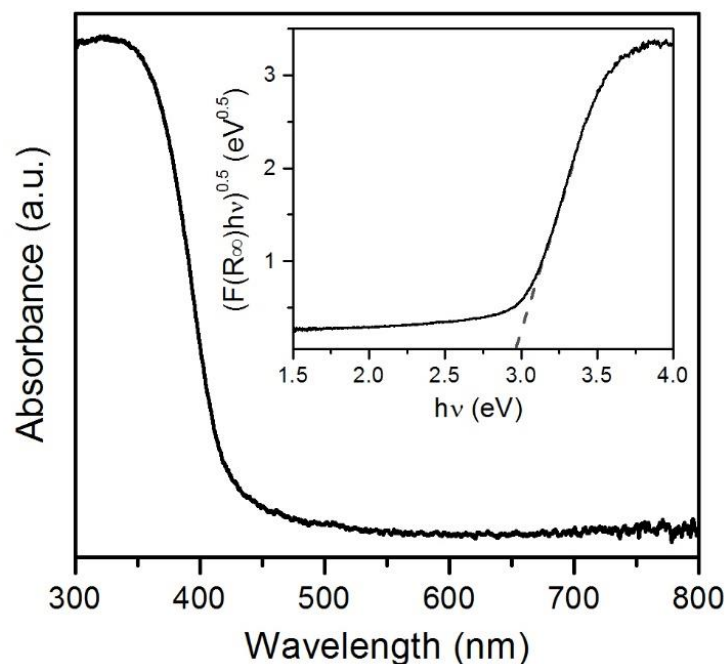


**Figure 3.8.** UV-vis diffuse reflectance data for  $\text{Bi}_2\text{O}_2[\text{BO}_2(\text{OH})]$  nanosheets synthesized from a 4:1 ratio of  $\text{H}_3\text{BO}_3:\text{Bi}_3(\text{NO}_3)_3$  at pH 8. Inset: corresponding Tauc plot used to estimate the optical bandgap of the sample.

#### *Synthesis of $\text{Bi}_2\text{WO}_6$ Nanosheets*

Next, we attempted to elucidate whether  $\text{Bi}_2\text{O}_2[\text{BO}_2(\text{OH})]$  nanosheets provide a templating effect and the extent to which the tungsten precursor plays a role in the final nano-morphology of  $\text{Bi}_2\text{WO}_6$ . To determine this,  $\text{Bi}_2\text{WO}_6$  was synthesized under hydrothermal conditions using  $\text{Bi}_2\text{O}_2[\text{BO}_2(\text{OH})]$  nanosheets as the bismuth oxide precursor with either soluble  $\text{Na}_2\text{WO}_4$  powder or  $\text{Cs}_4\text{W}_{11}\text{O}_{36}^{2-}$  nanosheets as the tungsten oxide precursor.  $\text{Cs}_4\text{W}_{11}\text{O}_{36}^{2-}$  nanosheets with an average thickness of  $\sim 2.5$  nm were prepared from  $\text{Cs}_{6+x}\text{W}_{11}\text{O}_{36}$  as described in Chapter II,<sup>18</sup> which is a modified synthesis from that provided by Fukuda et al.<sup>24</sup>

For the hydrothermal synthesis of  $\text{Bi}_2\text{WO}_6$  nanosheets, 95 mg (186  $\mu\text{mol}$ ) of the previously synthesized  $\text{Bi}_2\text{O}_2[\text{BO}_2(\text{OH})]$  sample was dissolved in 10 mL DI water and dispersed in a bath sonicator. The solution was placed in a Teflon-lined autoclave along with either 0.1 mL of a ( $\sim 80$

mM solution;  $\sim 8 \mu\text{mol}$ ) aqueous dispersion  $\text{Cs}_4\text{W}_{11}\text{O}_{36}^{2-}$  nanosheets or 33 mg of  $\text{Na}_2\text{WO}_4 \cdot 2\text{H}_2\text{O}$  ( $\sim 100 \mu\text{mol}$ ) to give a  $\sim 44:1$  molar ratio of bismuth to tungsten. The mixture was then reacted at  $220^\circ\text{C}$  for 24 hours. After reaction, the sample was centrifuged at 10,000 rpm for 5 minutes to isolate the insoluble nanosheets. The precipitate was then bath sonicated in 1 M nitric acid for 1 hour (x3) to remove any remaining precursor nanosheets. Figure 3.9 shows a PXRD pattern for  $\text{Bi}_2\text{WO}_6$  formed from  $\text{Na}_2\text{WO}_4 \cdot 2\text{H}_2\text{O}$  before and after acid washing; before acid washing  $\text{Bi}_2\text{O}_2[\text{BO}_2(\text{OH})]$  is clearly observed in the sample, whereas after acid washing only  $\text{Bi}_2\text{WO}_6$  remains. The resultant solid was rinsed with water and ethanol, and vacuum dried at  $50^\circ\text{C}$ . Figure 3.10 shows the PXRD patterns of the reaction product using  $\text{Cs}_4\text{W}_{11}\text{O}_{36}^{2-}$  nanosheets after 8, 16, and 24 hours of hydrothermal synthesis (after acid washing and drying). At 8 hours, the majority of the reaction mixture was  $\text{Cs}_4\text{W}_{11}\text{O}_{36}^{2-}$  nanosheets with a small amount of  $\text{Bi}_2\text{WO}_6$ . After 16 hours,  $\text{Bi}_2\text{WO}_6$  is clearly observed in the pattern; however, some  $\text{Cs}_4\text{W}_{11}\text{O}_{36}^{2-}$  nanosheets remain in the reaction mixture. After 24 hours, all of the  $\text{Cs}_4\text{W}_{11}\text{O}_{36}^{2-}$  nanosheets are consumed and only  $\text{Bi}_2\text{WO}_6$  is seen.

The reaction involving  $\text{Na}_2\text{WO}_4 \cdot 2\text{H}_2\text{O}$  produced a pale yellow powder with an isolated yield of 54.2 mg (77% yield); for reference, bulk  $\text{Bi}_2\text{WO}_6$  is yellow. The reaction involving  $\text{Cs}_4\text{W}_{11}\text{O}_{36}^{2-}$  produced a white powder of  $\text{Bi}_2\text{WO}_6$  with an isolated yield of 53.6 mg (87% yield), which is similar to what was produced in Chapter II when  $\text{Cs}_4\text{W}_{11}\text{O}_{36}^{2-}$  nanosheets and a soluble bismuth oxide precursor were used.<sup>18</sup>

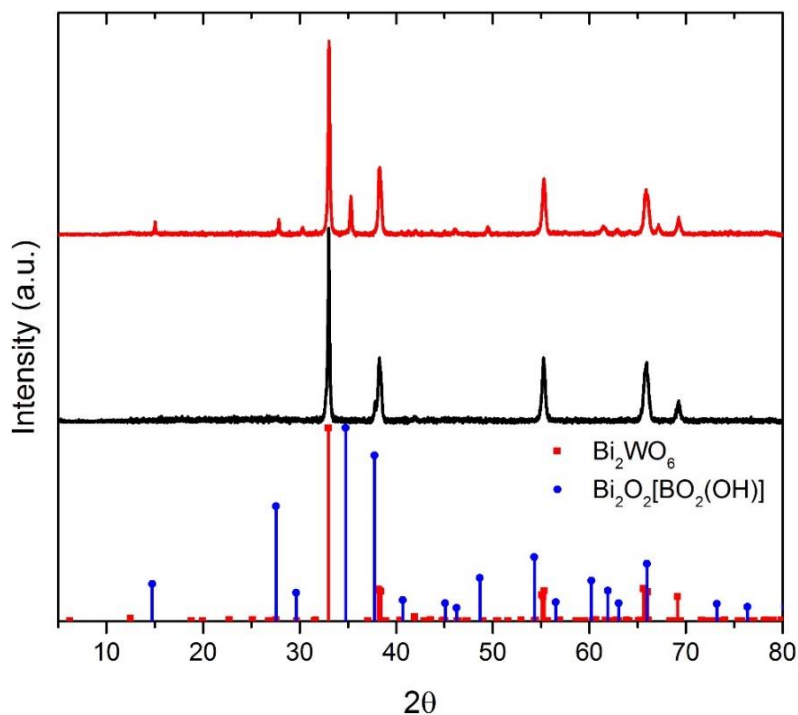


**Figure 3.9.** PXRD patterns before (red) and after (black) washing the reaction product made from  $\text{Na}_2\text{WO}_4 \cdot 2\text{H}_2\text{O}$  with 1 M nitric acid. Reference patterns for  $\text{Bi}_2\text{WO}_6$  and  $\text{Bi}_2\text{O}_2[\text{BO}_2(\text{OH})]$  are included.

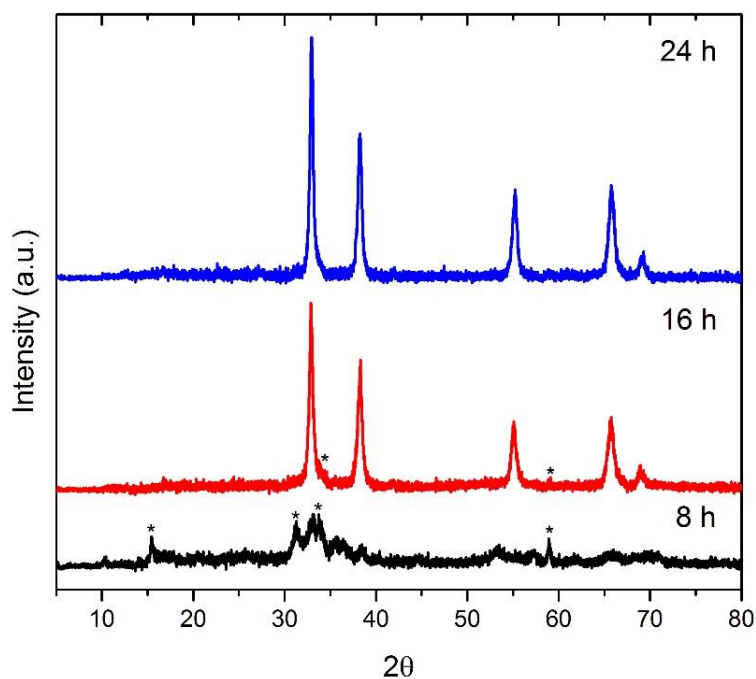


**Figure 3.10.** PXRD patterns of the reaction product made from  $\text{Cs}_4\text{W}_{11}\text{O}_{36}^{2-}$  nanosheets after reacting for 8 hours, 16 hours, and 24 hours, with acid washing and drying. The peaks at 24 hours match those of  $\text{Bi}_2\text{WO}_6$ . Peaks marked with an \* indicate remaining  $\text{Cs}_4\text{W}_{11}\text{O}_{36}^{2-}$  nanosheets.

Figure 3.11 shows the PXRD patterns of  $\text{Bi}_2\text{WO}_6$  produced from both tungstate sources ( $\text{Cs}_4\text{W}_{11}\text{O}_{36}^{2-}$  and  $\text{Na}_2\text{WO}_4$ ). The peaks of the  $\text{Bi}_2\text{WO}_6$  nanosheets produced from  $\text{Na}_2\text{WO}_4$  are narrower and more intense than those produced from the  $\text{Cs}_4\text{W}_{11}\text{O}_{36}^{2-}$  nanosheets. This can be explained by the morphology of the resultant  $\text{Bi}_2\text{WO}_6$ , as larger, more crystalline samples contribute to sharp PXRD peaks. As seen in the TEM and SEM images in Figure 3.12, the  $\text{Bi}_2\text{WO}_6$  nanosheets produced from  $\text{Na}_2\text{WO}_4$  are aggregated in thick platelets, where the platelets are multiple micrometers in lateral dimensions and hundreds of nanometers in thickness. This morphology is distinct from  $\text{Bi}_2\text{WO}_6$  produced from soluble precursors,  $\text{Bi}(\text{NO}_3)_3$  and  $\text{Na}_2\text{WO}_4$ , which produces a three-dimensional flower-like morphology consisting of two-dimensional  $\text{Bi}_2\text{WO}_6$  sheets.<sup>11, 12, 18</sup>

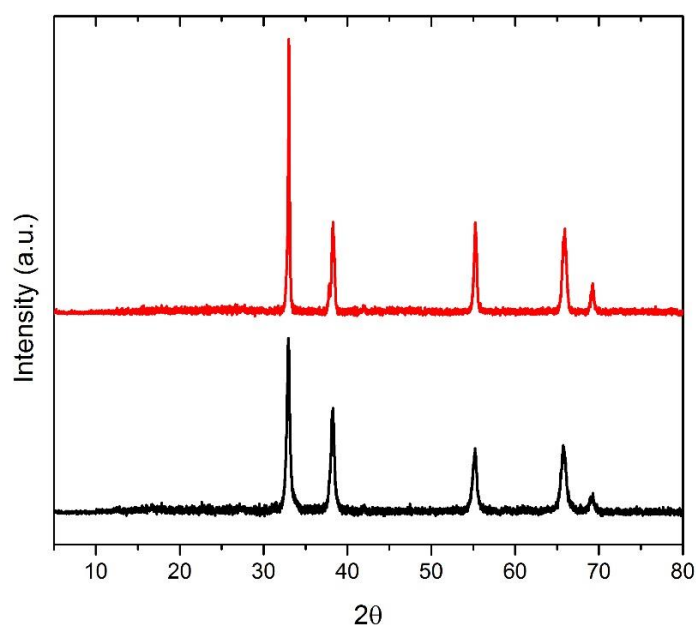


**Figure 3.11.** PXRD pattern of  $\text{Bi}_2\text{WO}_6$  made from  $\text{Na}_2\text{WO}_4$  (red) and  $\text{Cs}_4\text{W}_{11}\text{O}_{36}^{2-}$  nanosheets (black).

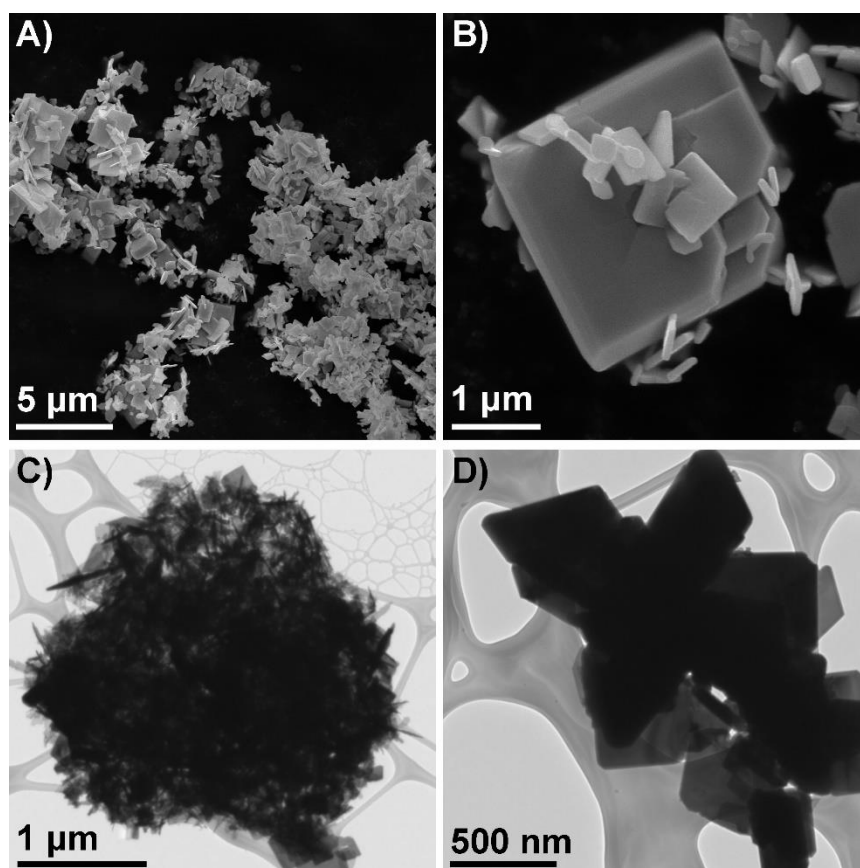


**Figure 3.12.** A,B) SEM and C,D) TEM images of  $\text{Bi}_2\text{WO}_6$  produced from  $\text{Bi}_2\text{O}_2[\text{BO}_2(\text{OH})]$  and  $\text{Na}_2\text{WO}_4$ , showing large aggregates of nanosheet platelets.

Conversely,  $\text{Bi}_2\text{WO}_6$  produced from all nanosheet precursors,  $\text{Bi}_2\text{O}_2[\text{BO}_2(\text{OH})]$  and  $\text{Cs}_4\text{W}_{11}\text{O}_{36}^{2-}$ , shows a nanosheet morphology, as seen in the TEM image, select area electron diffraction, AFM image, and height profile of the product given in Figure 3.13. The nanosheets have lateral dimensions in the micrometer range and thicknesses of 5–40 nm, which are comparable to the nanosheets produced in Chapter II from a soluble bismuth oxide source and  $\text{Cs}_4\text{W}_{11}\text{O}_{36}^{2-}$  nanosheets, which had lateral dimensions of 1–2  $\mu\text{m}$  and thicknesses of 5–15 nm.<sup>18</sup> However, the morphology of the nanosheets is altered slightly after acid washing. The nanosheets in Figure 3.13, which underwent acid washing, have rounded edges. In contrast, the nanosheets prior to acid washing, shown in Figure 3.14, have squared edges, though the lateral dimensions remain the same. In addition, the select area electron diffraction in Figure 3.14 indicates that the

observed nanosheets are, in fact,  $\text{Bi}_2\text{WO}_6$  and not any remaining  $\text{Bi}_2\text{O}_2[\text{BO}_2(\text{OH})]$  and  $\text{Cs}_4\text{W}_{11}\text{O}_{36}^{2-}$  precursor nanosheets.

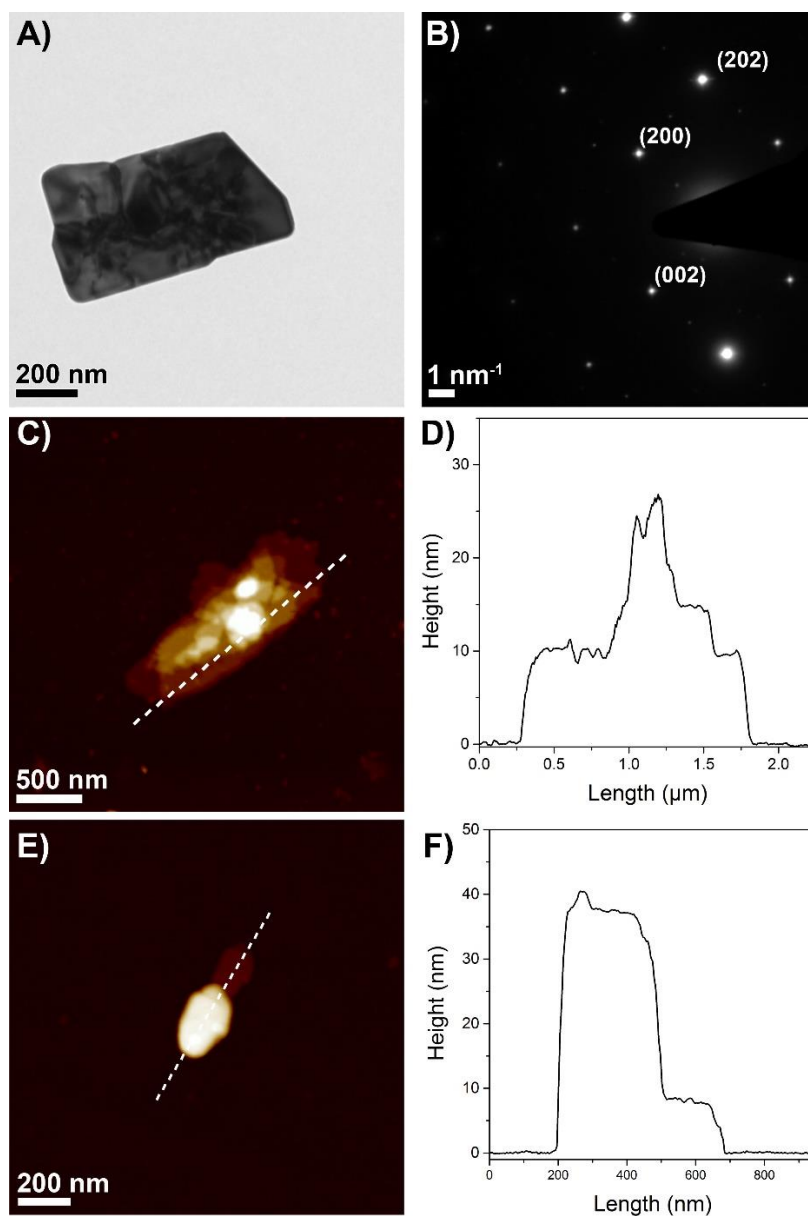


**Figure 3.13.** A) TEM image, B) select area electron diffraction, C, E) AFM image, and D,F) height profile of  $\text{Bi}_2\text{WO}_6$  produced from  $\text{Bi}_2\text{O}_2[\text{BO}_2(\text{OH})]$  and  $\text{Cs}_4\text{W}_{11}\text{O}_{36}^{2-}$  nanosheets after acid washing.

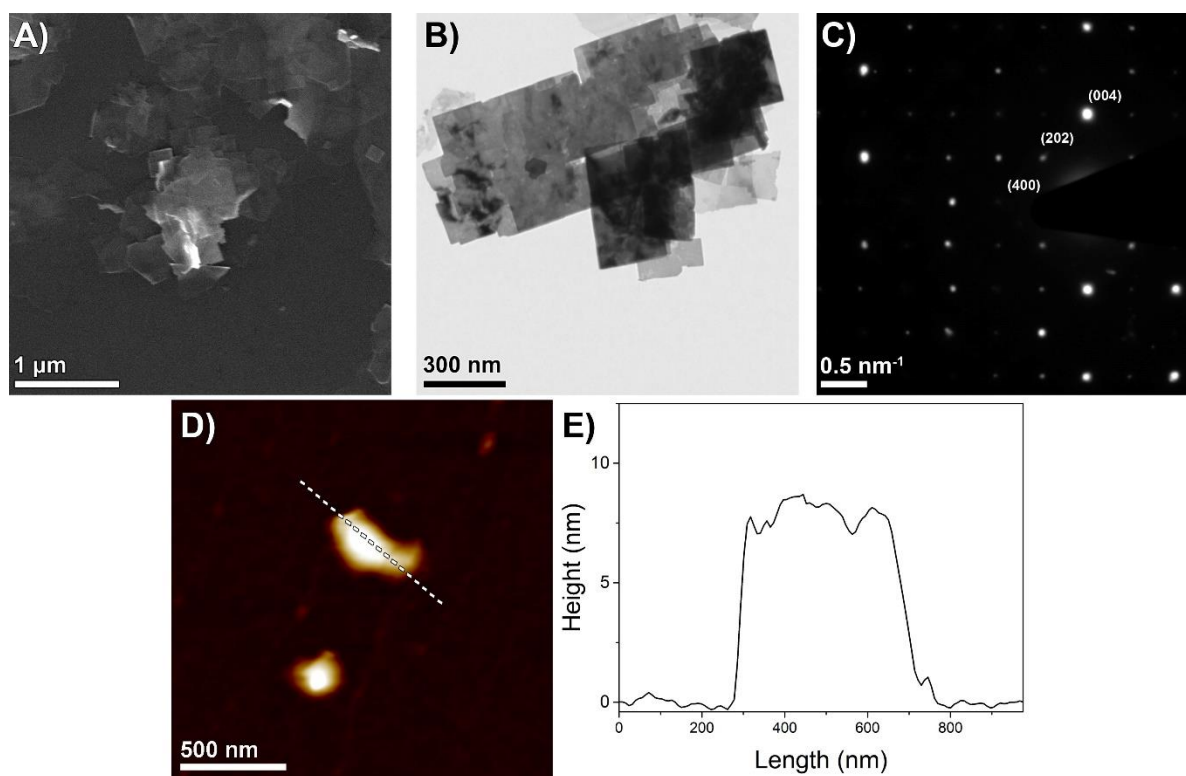


**Figure 3.14.** A) SEM image, B) TEM image, C) select area electron diffraction, D) AFM image, and E) height profile of  $\text{Bi}_2\text{WO}_6$  nanosheets produced from  $\text{Bi}_2\text{O}_2[\text{BO}_2(\text{OH})]$  and  $\text{Cs}_4\text{W}_{11}\text{O}_{36}^{2-}$  nanosheets prior to acid washing. The select area electron diffraction proves that the observed nanosheets are  $\text{Bi}_2\text{WO}_6$  and not any remaining  $\text{Bi}_2\text{O}_2[\text{BO}_2(\text{OH})]$  and  $\text{Cs}_4\text{W}_{11}\text{O}_{36}^{2-}$ .

The optical bandgap of  $\text{Bi}_2\text{WO}_6$  products made from  $\text{Bi}_2\text{O}_2[\text{BO}_2(\text{OH})]$  and either  $\text{Cs}_4\text{W}_{11}\text{O}_{36}^{2-}$  nanosheet precursors or soluble  $\text{Na}_2\text{WO}_4$  was estimated by UV-vis diffuse reflectance spectroscopy using the Tauc plot method (Figure 3.15). The determination of the bandgap for either direct ( $n = 1/2$ ) or indirect ( $n = 2$ ) allowed electronic transitions is accomplished by converting the UV diffuse reflectance data to the Kubelka-Munk function,  $F(R^\infty)$ , then applying it to the Tauc equation  $(h\nu F(R^\infty))^{1/n} = A(h\nu - E_g)$ . Plotting this equation and tracing a tangent line at the inflection point to the horizontal axis will result in a point of intersection with the horizontal axis that gives the bandgap ( $E_g$ ). In our previous work detailed in Chapter II,  $\text{Bi}_2\text{WO}_6$  nanosheets had an optical bandgap of  $\sim 3.1$  eV when an indirect transition ( $n = 2$ ) was used.<sup>18</sup> Here, an indirect

transition gives an optical bandgap of 2.06 eV for the  $\text{Bi}_2\text{WO}_6$  clusters made from  $\text{Bi}_2\text{O}_2[\text{BO}_2(\text{OH})]$  and  $\text{Na}_2\text{WO}_4$ , and for  $\text{Bi}_2\text{WO}_6$  nanosheets made from  $\text{Bi}_2\text{O}_2[\text{BO}_2(\text{OH})]$  and  $\text{Cs}_4\text{W}_{11}\text{O}_{36}^{2-}$ , an indirect transition gives an optical bandgap of 2.51 eV. In the literature, the optical bandgap for bulk  $\text{Bi}_2\text{WO}_6$  varies from 2.6–3.3 eV, depending on the method and model used to determine the bandgap; some methods calculated the bandgap assuming an indirect transition while others assumed a direct transition.<sup>15, 25-27</sup> Optical bandgaps for nanoscale  $\text{Bi}_2\text{WO}_6$  falls in the range of ~2.9 eV for multilayered discs,<sup>28</sup> 2.95–3.04 eV for microspheres,<sup>29</sup> and ~3.1 eV for flower-like structures.<sup>18</sup> Considering this variation between the determined value and the literature values, the optical bandgaps were also calculated using a direct transition ( $n = 1/2$ ). In this case, the optical bandgap for  $\text{Bi}_2\text{WO}_6$  clusters made from  $\text{Bi}_2\text{O}_2[\text{BO}_2(\text{OH})]$  and  $\text{Na}_2\text{WO}_4$  was calculated to be 2.78 eV, while that for  $\text{Bi}_2\text{WO}_6$  nanosheets made from  $\text{Bi}_2\text{O}_2[\text{BO}_2(\text{OH})]$  and  $\text{Cs}_4\text{W}_{11}\text{O}_{36}^{2-}$  was calculated to be 3.19 eV. These values fall closer to those in the literature; however, the tangent line does not present as high quality of a fit as does the data using an indirect transition (as shown by the  $R^2$  values in Figure 3.15).

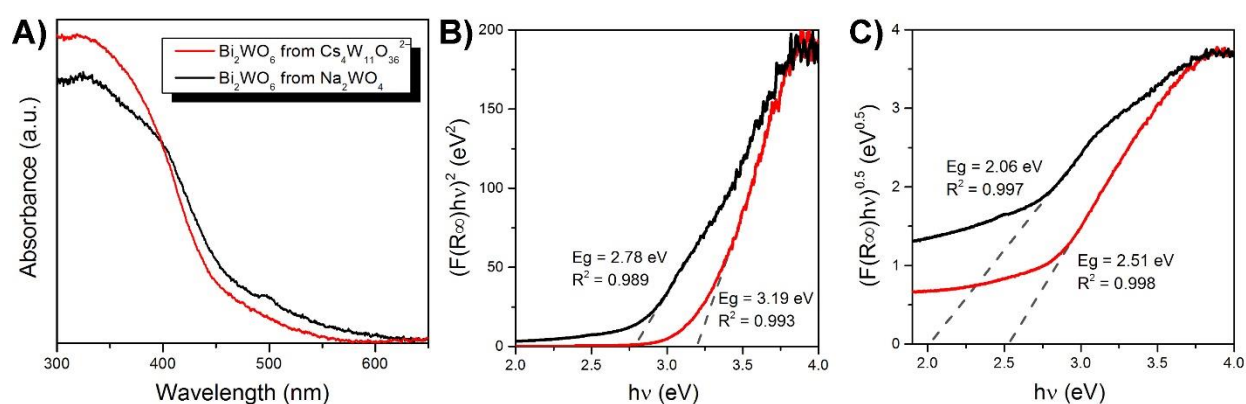


**Figure 3.15.** A) UV-vis diffuse reflectance data for  $\text{Bi}_2\text{WO}_6$  nanosheets produced from the  $\text{Bi}_2\text{O}_2[\text{BO}_2(\text{OH})]$  nanosheet precursor with either soluble  $\text{Na}_2\text{WO}_4$  precursor (black) or  $\text{Cs}_4\text{W}_{11}\text{O}_{36}^{2-}$  nanosheet precursors (red). Also included are the Tauc plots corresponding to a B) direct allowed transition and C) indirect allowed transition, which were used to estimate the optical bandgap of the samples.

## Conclusions

In order to take advantage of a templating effect when using nanosheet precursors, we optimized the synthesis of bismuth hydroxyl borate ( $\text{Bi}_2\text{O}_2[\text{BO}_2(\text{OH})]$ ) to produce pristine nanosheets with lateral dimensions in the micrometer range. We found that the reaction is highly sensitive to both the pH of the solution during hydrothermal synthesis and the stoichiometric ratio of the  $\text{H}_3\text{BO}_3$  to  $\text{Bi}_3(\text{NO}_3)_3$  reactants. Altering the pH lead to a change in product, while altering the stoichiometric ratio lead to a change in morphology. The optimal pH and stoichiometric ratio to produce  $\text{Bi}_2\text{O}_2[\text{BO}_2(\text{OH})]$  nanosheets were found to be 8 and 4:1, respectively.

The  $\text{Bi}_2\text{O}_2[\text{BO}_2(\text{OH})]$  nanosheets were then used as a reactive precursor in the hydrothermal synthesis of  $\text{Bi}_2\text{WO}_6$  to produce two-dimensional  $\text{Bi}_2\text{WO}_6$  morphologies when both soluble ( $\text{Na}_2\text{WO}_4$ ) and nanosheet ( $\text{Cs}_4\text{W}_{11}\text{O}_{36}^{2-}$ ) tungsten oxide precursors were used.  $\text{Bi}_2\text{WO}_6$  produced from a soluble  $\text{Na}_2\text{WO}_4$  precursor presented as aggregated platelets of nanosheets. This morphology is similar to the flower-like morphology produced when both the bismuth and tungsten oxide precursors are soluble.<sup>11, 12</sup>  $\text{Bi}_2\text{WO}_6$  produced from the  $\text{Cs}_4\text{W}_{11}\text{O}_{36}^{2-}$  nanosheet precursor formed thin nanosheets with lateral dimensions in the micrometer range and thicknesses of 5–40 nm. This morphology is comparable to the  $\text{Bi}_2\text{WO}_6$  nanosheet morphology obtained when a soluble bismuth oxide precursor and a  $\text{Cs}_4\text{W}_{11}\text{O}_{36}^{2-}$  nanosheet precursor was used.<sup>18</sup> Overall, the  $\text{Cs}_4\text{W}_{11}\text{O}_{36}^{2-}$  nanosheet tungsten oxide precursor seems provide a better template for  $\text{Bi}_2\text{WO}_6$  nanosheet formation, though the  $\text{Bi}_2\text{O}_2[\text{BO}_2(\text{OH})]$  nanosheet precursor does influence the nano-morphology of the final product. Thus, we affirm our previous conclusion that  $\text{Cs}_4\text{W}_{11}\text{O}_{36}^{2-}$  nanosheet templating remains the most effective way to prepare and isolate large  $\text{Bi}_2\text{WO}_6$  nanosheets.

## References

1. Tang, J.; Zou, Z.; Ye, J. *Catal. Lett.* **2004**, 92, (1), 53-56.
2. Zhang, C.; Zhu, Y. *Chem. Mater.* **2005**, 17, (13), 3537-3545.
3. Fu, H.; Pan, C.; Yao, W.; Zhu, Y. *J. Phys. Chem. B* **2005**, 109, (47), 22432-22439.
4. Amano, F.; Yamakata, A.; Nogami, K.; Osawa, M.; Ohtani, B. *J. Am. Chem. Soc.* **2008**, 130, (52), 17650-17651.
5. Zhang, L.; Wang, H.; Chen, Z.; Wong, P. K.; Liu, J. *Applied Catalysis B: Environmental* **2011**, 106, (1-2), 1-13.
6. Kudo, A.; Hijii, S. *Chem. Lett.* **1999**, 28, (10), 1103-1104.
7. Zhang, L.; Wang, W.; Zhou, L.; Xu, H. *Small* **2007**, 3, (9), 1618-1625.
8. Shang, M.; Wang, W.; Sun, S.; Zhou, L.; Zhang, L. *Journal of Physical Chemistry C* **2008**, 112, (28), 10407-10411.
9. Ma, R.; Sasaki, T. *Acc. Chem. Res.* **2015**, 48, (1), 136-143.
10. Sun, S.; Wang, W.; Zhang, L.; Gao, E.; Jiang, D.; Sun, Y.; Xie, Y. *ChemSusChem* **2013**, 6, (10), 1873-1877.
11. Zhang, L.; Wang, W.; Chen, Z.; Zhou, L.; Xu, H.; Zhu, W. *J. Mater. Chem.* **2007**, 17, (24), 2526-2532.
12. Xia, J.; Li, H.; Luo, Z.; Xu, H.; Wang, K.; Yin, S.; Yan, Y. *Mater. Chem. Phys.* **2010**, 121, (1-2), 6-9.
13. Fu, H.; Zhang, L.; Yao, W.; Zhu, Y. *Applied Catalysis B: Environmental* **2006**, 66, (1-2), 100-110.
14. Zhang, S.; Zhang, C.; Man, Y.; Zhu, Y. *J. Solid State Chem.* **2006**, 179, (1), 62-69.

15. Huang, Y.; Ai, Z.; Ho, W.; Chen, M.; Lee, S. *Journal of Physical Chemistry C* **2010**, 114, (14), 6342-6349.
16. Shang, M.; Wang, W.; Xu, H. *Crystal Growth & Design* **2009**, 9, (2), 991-996.
17. Wu, L.; Bi, J.; Li, Z.; Wang, X.; Fu, X. *Catal. Today* **2008**, 131, (1-4), 15-20.
18. Pope, T. R.; Lassig, M. N.; Neher, G.; Weimar III, R. D.; Salguero, T. T. *Journal of Materials Chemistry C* **2014**, 2, (17), 3223.
19. Zhang, R.; Dai, Y.; Lou, Z.; Li, Z.; Wang, Z.; Yang, Y.; Qin, X.; Zhang, X.; Huang, B. *CrystEngComm* **2014**, 16, (23), 4931.
20. Huang, H.; He, Y.; Lin, Z.; Kang, L.; Zhang, Y. *The Journal of Physical Chemistry C* **2013**, 117, (44), 22986-22994.
21. Cong, R.; Sun, J.; Yang, T.; Li, M.; Liao, F.; Wang, Y.; Lin, J. *Inorg. Chem.* **2011**, 50, (11), 5098-5104.
22. Christensen, A. N.; Chevallier, M.-A.; Skibsted, J.; Iversen, B. B. *J. Chem. Soc., Dalton Trans.* **2000**, (3), 265-270.
23. Xie, L.; Wang, J.; Hu, Y.; Zheng, Z.; Weng, S.; Liu, P.; Shi, X.; Wang, D. *Mater. Chem. Phys.* **2012**, 136, (2-3), 309-312.
24. Fukuda, K.; Akatsuka, K.; Ebina, Y.; Ma, R.; Takada, K.; Nakai, I.; Sasaki, T. *ACS Nano* **2008**, 2, (8), 1689-1695.
25. Mahanty, S.; Ghose, J. *Mater. Lett.* **1991**, 11, (8-9), 254-256.
26. Zhou, L.; Yu, M.; Yang, J.; Wang, Y.; Yu, C. *The Journal of Physical Chemistry C* **2010**, 114, (44), 18812-18818.
27. Bhattacharya, C.; Lee, H. C.; Bard, A. J. *Journal of Physical Chemistry C* **2013**, 117, (19), 9633-9640.

28. Xu, C.; Wei, X.; Guo, Y.; Wu, H.; Ren, Z.; Xu, G.; Shen, G.; Han, G. *Mater. Res. Bull.* **2009**, 44, (8), 1635-1641.
29. Zhou, Y.; Antonova, E.; Bensch, W.; Patzke, G. R. *Nanoscale* **2010**, 2, (11), 2412-7.

**CHAPTER 4**

**NANOSCALE TRANSITION METAL DICHALCOGENIDES:  
FORMATION AND APPLICATIONS OF TANTALUM DISELENIDE**

Timothy R. Pope, Pradyumna Goli, Chenglong Jiang , Jacqueline Renteria, Rameez Samnakay, Zhong Yan, Darshana Wickramaratne, Alexander Khitun, Roger Lake, Alexander Balandin and Tina T. Salguero. *In preparation for Crystal Growth & Design.*

## Abstract

Transition metal dichalcogenides are layered materials with interesting nanoscale properties similar to graphene. Of special interest is tantalum diselenide ( $\text{TaSe}_2$ ), which can be synthesized in the  $1T$ ,  $2H$ , or  $3R$  polytype using chemical vapor transport (CVT). CVT forms bulk crystals that can extend up to millimeters in diameter. The bulk material can then be exfoliated into nanosheets using ultrasonication. In this chapter, the oxidation behavior of several polytypes of  $\text{TaSe}_2$  is examined. Exposure to air at elevated temperatures leads to the formation of tantalum oxide on the surface. Prolonged exposure to air at atmospheric temperatures causes a polytype transformation from  $1T$ - $\text{TaSe}_2$  to  $2H$ - $\text{TaSe}_2$ . Because both oxidation and polytype transformation are limited to the crystal surface, delamination of the top layer using the Scotch tape method removes any impurities to recover pristine crystals. It is necessary to have pristine nanosheets in electronics applications because the different polytype have different electronic behaviors and surface oxidation can inhibit electron transport. This chapter also outlines several novel characterization methods and applications of  $\text{TaSe}_2$  that were carried out by our collaborators at the University of California, Riverside.

## Introduction

Graphene, a single two-dimensional layer of conjugated carbon atoms, has been thoroughly studied in the past decade due to its interesting electronic properties. Graphene field-effect transistors (FETs) display high mobility,<sup>1,2</sup> high saturation velocity,<sup>3</sup> low flicker noise,<sup>4,5</sup> and can be gated at room temperature.<sup>1,2,6</sup> Additionally, the graphene FETs' lower flicker noise (also called  $1/f$  noise or pink noise) provides increased functionalities for signal processing compared with conventional electronic devices.<sup>5,7,8</sup> For fundamental research graphene is typically exfoliated from graphite using the Scotch-tape method, where a piece of tape is used to separate a single layer of graphene from the bulk.<sup>6</sup> Currently, graphene is difficult to fabricate in large dimensions, but if made on a large scale, has the potential to revolutionize electronics. However, because graphene does not have a band gap, devices cannot be switched off. Furthermore, high carrier concentrations and high mobilities inherent in the material lead to substantial device leakage currents, and graphene devices also are susceptible to radiation damage.<sup>9</sup>

In order to overcome deficiencies of graphene, researchers have turned to alternative two-dimensional materials. Another example of a “graphene-like” material is bismuth telluride ( $\text{Bi}_2\text{Te}_3$ ). Bismuth telluride can be cleaved into single layers then restacked to form quasi-2D crystals that have electrical and thermal properties unique from the bulk material.<sup>10,11</sup> Circuits made from such metallic materials would have certain benefits (i.e. low cost and resistance to radiation damage) over circuits made from either traditional semiconducting materials or novel materials like graphene.

Two-dimensional transition metal dichalcogenides ( $\text{MX}_2$ ) also have been referred to as “graphene-like” due to their similar physical, electrical, and thermal properties. Such layered van der Waals materials can be mechanically cleaved (delaminated) from bulk crystals in a similar

manner to graphene (i.e., by the Scotch tape method), chemically exfoliated, or exfoliated by sonication.

One of the most well studied  $\text{MX}_2$  materials is molybdenum disulfide ( $\text{MoS}_2$ ), otherwise known by its mineral name molybdenite. Molybdenite is found naturally throughout the world and is mined often as a co-deposit with graphite. Molybdenite is widely used in industry as a catalyst to remove sulfur from petroleum streams by hydrodesulfurization, where the edge sites are the active sites for catalysis. In hydrodesulfurization, organosulfur functionalities are removed from refined petroleum products using reductive hydrogen to produce  $\text{H}_2\text{S}$ . In another industrial application, nanocomposites of  $\text{MoS}_2$  are used as catalysts for hydroconversion (Microcat®), where hydrogenation and thermal decomposition, otherwise known as cracking, occur simultaneously. Because the material has nanoscale dimensions, the surface area and thus the edge sites of coordinatively unsaturated molybdenum sites are maximized for catalysis.<sup>12-14</sup> Much like graphite, delaminated molybdenum disulfide also can be used as a dry lubricant; however, it is more suitable for use at higher temperatures. Moreover, friction force microscopy on few-layer  $\text{MoS}_2$  (and other two-dimensional materials such as graphene and  $\text{NbSe}_2$ ) showed decreasing thickness correlates to an increase in the friction force on the materials, which could lead to control of the nanoscale-friction of nano-electromechanical devices.<sup>15</sup> In addition, exfoliated  $\text{MoS}_2$  nanosheets also display interesting photoluminescence properties and can be used as light emitters in optoelectronic devices, such as photovoltaics and light emitting diodes.<sup>16, 17</sup>

Like graphene,  $\text{MoS}_2$  delaminated into two-dimensional films that are on a smaller scale than that of the Bohr exciton radius of the material (e.g. mono- to few-layers) has similar quantum mechanical confinement effects. Though bulk  $\text{MoS}_2$  is an indirect bandgap semiconductor with a bandgap of 1.2 eV, monolayer  $\text{MoS}_2$  is a direct bandgap semiconductor with a 1.8 eV bandgap.

The presence of a band gap on this scale allows the use of MoS<sub>2</sub> nanosheets as the “on/off switch” in nano-FET devices; this is in contrast with graphene, which has no bandgap. Recently, Radisavljevic et al. fabricated a field-effect transistor based on single layer MoS<sub>2</sub> that achieved a mobility of 200 cm<sup>2</sup>V<sup>-1</sup>s<sup>-1</sup>, on/off ratio exceeding 10<sup>8</sup>, and ultralow standby power dissipation.<sup>18</sup> In subsequent work by the same author, a device with dual-gated geometry was used to demonstrate the dependence of single-layer MoS<sub>2</sub> conductivity on temperature.<sup>19</sup> Interestingly, the material showed a temperature-dependent conductivity, which implies a metal to insulator transition. At charge carrier densities below 1x10<sup>13</sup> cm<sup>-2</sup> the conductance decreased as the temperature decreased; however, at higher charge carrier densities the conductance increased as the temperature decreased. Lembke and Kis have shown that MoS<sub>2</sub> has an extremely high maximum current density of 5x10<sup>7</sup> A/cm<sup>2</sup>.<sup>20</sup> This value is 50 times higher than the limit in maximum current density for metals and is proposed to be a result of the interlayer Mo–S covalent bonds being of higher strength than metallic bonds.<sup>21-23</sup>

Though MoS<sub>2</sub> is the most well studied MX<sub>2</sub> material due to its ready availability, other MX<sub>2</sub> materials display interesting electronic properties as well. Liu et al. have shown that field-effect transistors based on multilayer tungsten disulfide (WS<sub>2</sub>) exhibits comparable electronic properties to MoS<sub>2</sub> transistors, with on/off ratios of 10<sup>8</sup> and electron mobility up to 234 cm<sup>2</sup>V<sup>-1</sup>s<sup>-1</sup>.<sup>24</sup> In particular, tantalum diselenide (TaSe<sub>2</sub>) has remarkable properties such as superconductivity,<sup>25</sup> anisotropic optical properties,<sup>26</sup> and an anomalous change in magnetic properties at low temperatures.<sup>27</sup> TaSe<sub>2</sub> also has a superlattice structure that denotes a second level of organization after the repeating unit cell (i.e. the layered structure).<sup>28, 29</sup> Many of the remarkable properties of TaSe<sub>2</sub> can be changed by changing the thickness of the material. For example, the thermal conductivity of TaSe<sub>2</sub> sheets decreases as the sheet thickness is decreased.<sup>30</sup> Because the thermal

conductivity arises from phonon effects, when the sample thickness is nearly equal to the phonon mean free path the thermal conductivity decreases due to acoustic phonon-boundary scattering, indicating that the two-dimensional nature of the film influences the thermal transport properties more so than intrinsic lattice properties.<sup>30</sup>

TaSe<sub>2</sub> can be isolated as nanosheets using similar methods that are applied to graphene; however, unlike graphene, TaSe<sub>2</sub> has multiple crystal structures with corresponding electrical properties. The metallic form of TaSe<sub>2</sub> cannot directly replace graphene in all applications. For example, field-effect transistors typically employ semiconducting materials so that the conductivity of the charge carrier material can be controlled by an applied voltage. However, with slight modification of the device structure, all-metallic electronic devices can be fabricated from metallic 2H-TaSe<sub>2</sub> nanosheets due to an unexpected abrupt change from highly resistive to conductive when a certain voltage threshold is applied.<sup>31</sup> Because the voltage threshold is dependent on the nanosheet thickness, such all-metallic devices could be used as logic circuits by using two TaSe<sub>2</sub> nanosheets of different thickness in parallel. In addition, metallic TaSe<sub>2</sub> has the potential to be used in spintronic devices because of the material's strong spin-orbit coupling and short spin-orbit scattering length of 17 nm.<sup>32</sup> Alternatively, the metallic characteristics of TaSe<sub>2</sub> can be removed by doping the material with iron, which causes a metal to insulator transition.<sup>33</sup> Iron-doped TaSe<sub>2</sub> is also strongly ferromagnetic at extremely low temperatures (2 K).<sup>34</sup>

A particularly interesting electrical phenomenon present in a number of MX<sub>2</sub> materials, including TaSe<sub>2</sub>, is charge density waves (CDWs). Single layer nanosheets have the ability to CDWs at temperatures approaching room temperature.<sup>35</sup> CDWs arise from a periodic ordering of electron density within the material and can be viewed as a macroscopic quantum state.<sup>35</sup> This ordering of electron density also occurs concurrent with a periodic distortion of the atomic lattice

of the crystal.<sup>29</sup> CDWs are temperature-dependent and can manifest in commensurate, nearly commensurate, and incommensurate phases. The different phases correspond to different lattice distortions. In the commensurate phase, the electron density is aligned with the atomic lattice. In the incommensurate phase, the electron density is not aligned with the atomic lattice and is often the result of random impurities which distorts the crystal lattice away from periodicity.<sup>36</sup> However, the CDW state can be altered by changing the temperature even without the presence of impurities. The temperature at which the transition occurs depends on both the energy necessary to induce a lattice distortion and the stability gained by altering the electronic state.<sup>37</sup>

CDW states are especially prevalent in two-dimensional inorganic materials and have been studied in a number of  $\text{MX}_2$  materials, including  $\text{TiSe}_2$ ,  $\text{NbSe}_2$ ,  $\text{TaSe}_2$ .<sup>29, 38-40</sup> Goli et al. have reported that decreasing the thickness of  $\text{TiSe}_2$  films increases the temperature at which a CDW transition occurs.<sup>39</sup> However, in both  $\text{VSe}_2$  and  $\text{TaS}_2$  films, decreasing the film thickness lowers the CDW transition temperature.<sup>41-43</sup> This difference in behavior is due to the mechanism of CDW transition and is specific to each two-dimensional  $\text{MX}_2$  material—as well as polymorphs of each.<sup>44-46</sup> Thus, it is necessary to examine the CDW for the specific material of interest. Several groups have reported the existence of CDW states in thin films of  $\text{TaSe}_2$ , specifically, by using Raman spectroscopy to track changes in the crystal lattice structure.<sup>47-51</sup> Somnakay et al. were able to track the transition temperature where  $1T\text{-TaSe}_2$  switches from commensurate CDW to incommensurate CDW using Raman spectroscopy<sup>37</sup> and will be discussed in further detail later in this report.

The following sections focus on tantalum diselenide ( $\text{TaSe}_2$ ) and discuss the structure and polytypes, preparation and characterization, oxidation behavior, exfoliation techniques to create nanosheets, and, finally, applications and electronic devices fabricated and tested by our collaborators at the University of California, Riverside.<sup>30, 31, 37</sup>

## Results and Discussion

### *Structure of Tantalum Diselenide*

$\text{MX}_2$  materials have a layered structure comprised of repeating two-dimensional sandwich-like layer units of transition metal encased in chalcogenide (X-M-X). Each layer is held together by van der Waals forces. This distinctive structure allows  $\text{MX}_2$  materials to be exfoliated relatively easily into two-dimensional nanosheets. Small ions or molecules, such as small organic molecules or alkali earth metals, can be intercalated in between the unit layers, allowing for exfoliation into single unit layers or use in interesting applications such as lithium ion batteries.<sup>52-54</sup>

The structure we focus on in this report is tantalum diselenide ( $\text{TaSe}_2$ ), the structure of which consists of alternating Se-Ta-Se layers and is shown in Figure 4.1. Alternative modalities of the coordination geometry and stacking arrangement of Se-Ta-Se layers produces several polytypes. The three most common polymorphs being the *1T*-, *2H*-, and *3R*- $\text{TaSe}_2$  polytypes—this is also true for most layered transition metal dichalcogenide. The numeral prefix in the polytype name represents the total number of X-M-X layers in the unit cell; for example, in the *2H*- $\text{TaSe}_2$  polytype there are two X-M-X unit layers in the unit cell. The italicized letter in the prefix signifies the crystal structure; for example, *H* denotes a hexagonal structure, *R* a rhombohedral, and *T* a trigonal structure. These different polytypes present various electrical and physical properties. For example, CDWs in *2H*- $\text{TaSe}_2$  are present at low temperatures, while CDWs in *1T*- $\text{TaSe}_2$  present at room temperature and can undergo commensurate to incommensurate transitions.<sup>55</sup> In addition, *1T*- and *2H*- $\text{TaSe}_2$  tend to be metallic and become superconducting at low temperatures., while *3R*- $\text{TaSe}_2$  has a superconducting transition temperature 6–17 times higher than that of *2H*- $\text{TaSe}_2$ .<sup>25</sup>

The major difference between these three structures is the coordination geometry between the transition metal center and the chalcogenide. In the *1T*- $\text{TaSe}_2$  structure, the tantalum metal

center and the selenium atoms forms an octahedral coordination geometry, where the selenium atoms are rotated by  $60^\circ$  in the X-M-X layer above and below. This is in contrast to the  $2H$ - and  $3R$ -TaSe<sub>2</sub> forms, which both have trigonal prismatic coordination geometries, where the selenium atoms are positioned directly above and below one another. The  $2H$ -TaSe<sub>2</sub> structure consists of a two-layer repeating pattern of trigonal prismatic X-M-X layers, where the tantalum atoms are located on top of one another (as in the case of  $1T$ -TaSe<sub>2</sub>) and the trigonal prisms (selenium atoms) are rotated  $60^\circ$  from each other above and below (AcA BcB repeating units), see Figure 4.1. The  $3R$  structure has a three-layer stacking pattern where the metals are off-set from the X-M-X layers above and below. Interestingly, some of the polytypes have different colors, as shown in Figure 4.2,  $2H$ - and  $3R$ -TaSe<sub>2</sub> are silver, while  $1T$ -TaSe<sub>2</sub> is golden.

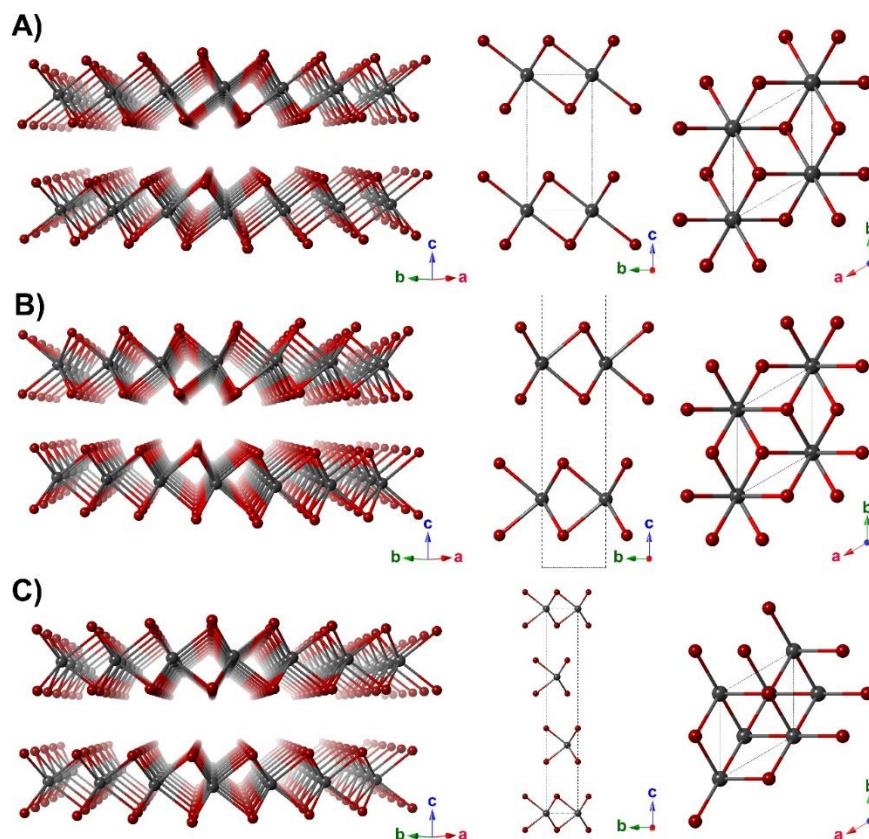


**Figure 4.1.** Different crystal structures of TaS<sub>2</sub>: A)  $1T$ -TaS<sub>2</sub>, B)  $2H$ -TaS<sub>2</sub>, and C)  $3R$ -TaS<sub>2</sub>. The views at left highlight the layered nature of these materials and the van der Waals gap. The views in the middle and at right show the structures along the a-axis (middle) and c-axis (right).

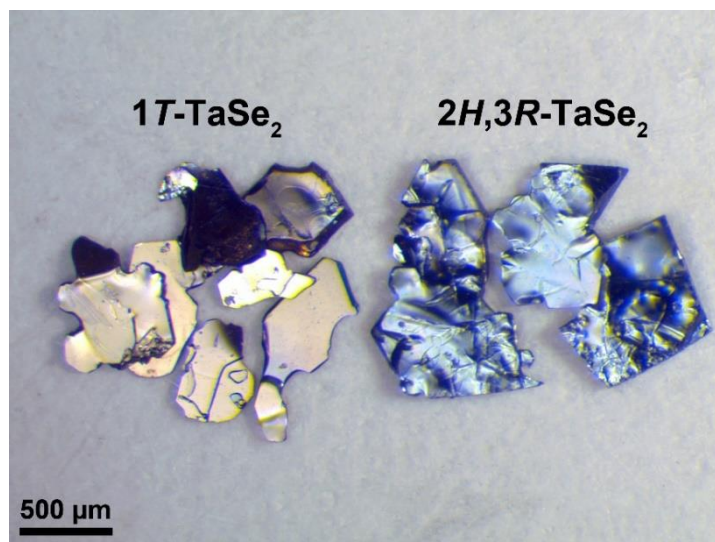


**Figure 4.2.** As-grown crystals of TaSe<sub>2</sub>: the silver crystals (right) are mixed 2H,3R-TaSe<sub>2</sub> and the golden crystals (left) are 1T-TaSe<sub>2</sub>. Reprinted with permission from *Nano Lett.* **15**, 2965 (2015). Copyright 2015 American Chemical Society.

#### *Materials Preparation and Characterization*

Bulk MX<sub>2</sub> samples are produced by heating stoichiometric amounts of elemental transition metal and chalcogenide at high temperatures in an air-free environment.<sup>56, 57</sup> The elemental powders are ground together for thorough mixing and placed in a quartz ampule. To ensure that no oxygen is present in the sample, the ampule is evacuated and backfilled with argon gas for three cycles. After the final evacuation, the ampule is sealed and heated to 700 °C in a furnace. After 15 hours, the ampule is removed from the furnace and allowed to cool naturally, shaken to mix the powders further, and exposed to a second heating cycle at 900 °C for 15 hours, and once again allowed to cool naturally. The resultant powder of micro-regime crystals are used as a precursor for chemical vapor transport (CVT) which produces large, pristine millimeter-sized crystals suitable for mechanical exfoliation into mono- to few-layer samples.<sup>31, 58</sup> Figure 4.3 shows the general schematic for CVT. During CVT, the microcrystalline MX<sub>2</sub> powder is loaded at one end a quartz ampule along with a chemical transport agent, typically 3–5 mg/cm<sup>3</sup> of I<sub>2</sub>. To prevent

oxidation at high temperatures, oxygen and water must be completely excluded from the system through the use of proper glassware preparation, evacuation, inert gas purging cycles, and quartz ampule sealing. In order to prevent excess sublimation of  $I_2$  during evacuation the ampule is fixed in a dry ice/acetonitrile cooling bath ( $-41\text{ }^\circ\text{C}$ ). Once sealed, the ampule is heated to CVT temperatures in a furnace with two temperature zones; where a high temperature zone and a low temperature zone is set. The end of the ampule containing the sample and transport agent is exposed to the high temperature zone, which is typically  $50\text{--}100\text{ }^\circ\text{C}$  higher than the low temperature zone. The source material complexes with the transport agent and deposits on the low temperature zone of the ampule; where large, pristine crystals are grown. After several weeks of CVT growth, the crystals can reach lateral dimensions of millimeters. Figure 4.4 highlights the change in crystal size before and after CVT for  $WSe_2$  and  $TaSe_2$ .

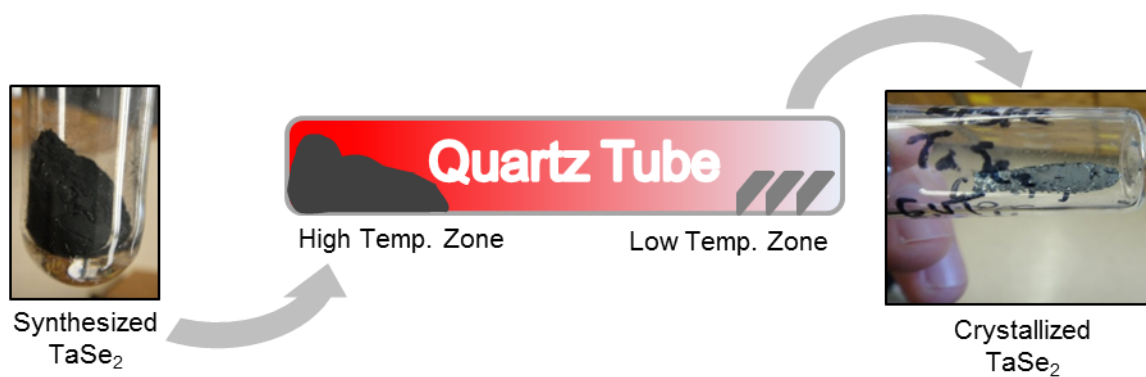


**Figure 4.3.** Schematic for the chemical vapor transport (CVT) of  $MX_2$  single crystals. The two different temperature zones allow for the sublimation (high temp. zone) and deposition (low temp. zone) of the crystals. A chemical transport agent, such as  $I_2$ , carries the material from the high temperature zone to the low temperature zone. Before CVT, the sample is microcrystalline. After CVT, large single crystals emerge.

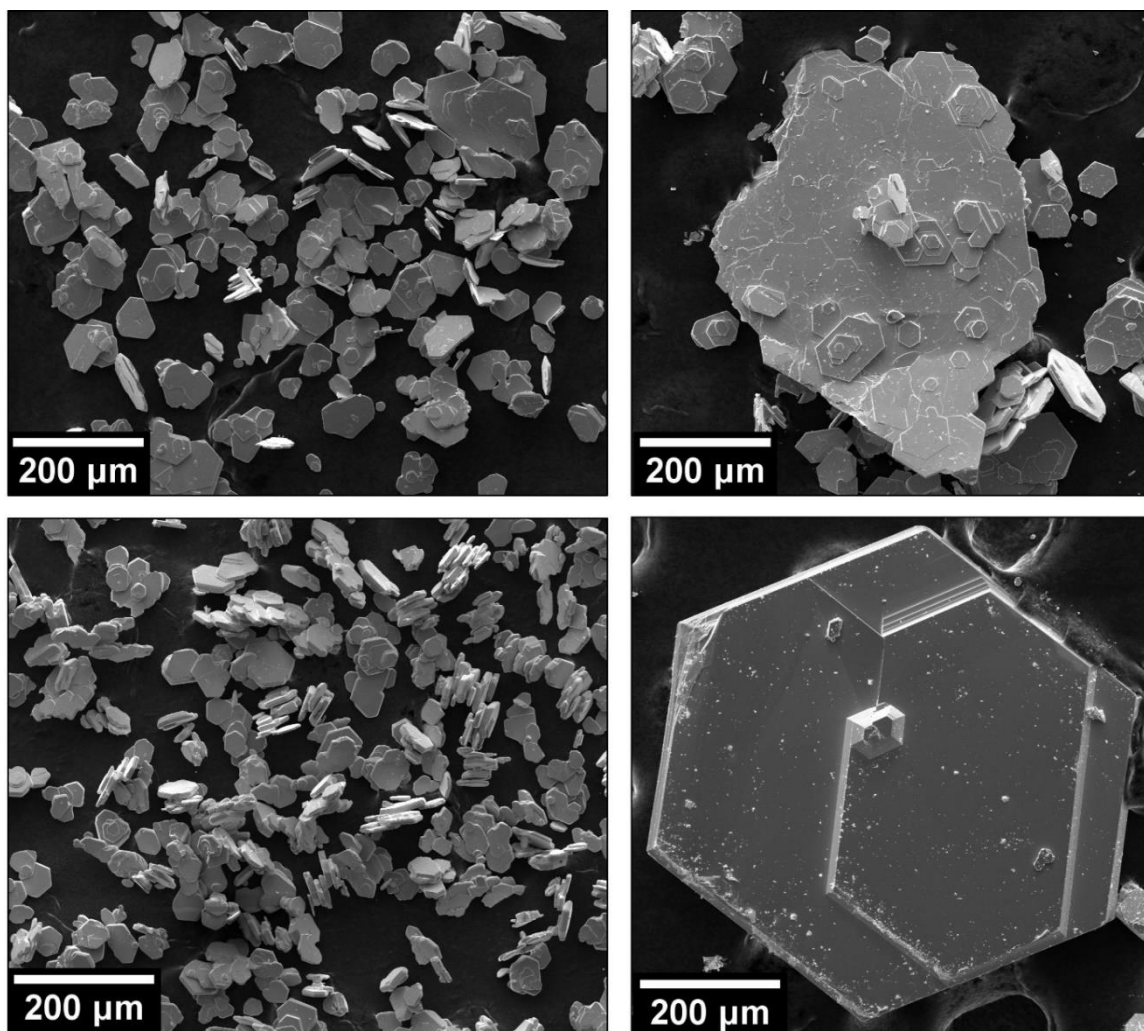


**Figure 4.4.** SEM images of  $\text{WSe}_2$  (top) and  $\text{TaS}_2$  (bottom) before (left) and after (right) CVT. In both cases, precursor crystals are  $\sim 60 \mu\text{m}$  in length with thicknesses of  $\sim 5\text{--}10 \mu\text{m}$ . After CVT, the lateral dimensions of the crystals increase dramatically to  $\sim 200\text{--}800 \mu\text{m}$  with thicknesses of  $5\text{--}30 \mu\text{m}$ .

Crystal growth is strongly dependent on the CVT temperature and temperature gradient across the temperature zones.<sup>56</sup> In addition, the crystal phase, or polytype, is determined by the CVT temperature and cooling rate after CVT completion.<sup>57, 59</sup> For example, bulk precursor crystals of tantalum diselenide ( $\text{TaSe}_2$ ) synthesized from elemental materials produces the  $3R\text{-TaSe}_2$  polytype. Upon CVT at  $\sim 800 \text{ }^\circ\text{C}$ , these crystals are vaporized and reformed at the low temperature zone in the quartz ampule. After transport, a slow cooling rate ( $1 \text{ }^\circ\text{C}/\text{min}$ ) results in an almost

complete conversion to  $2H$ -TaSe<sub>2</sub>. Figure 4.5 shows a PXRD pattern of the  $3R$ -TaSe<sub>2</sub> precursor and  $2H$ -TaSe<sub>2</sub> crystals after CVT. The broad peaks in the precursor pattern indicate small crystallites, while the defined peaks in the  $2H$ -TaSe<sub>2</sub> pattern indicates a large, highly crystalline product. Rapidly quenching the CVT ampule in an ice bath from growth temperatures exceeding 900 °C produces the high temperature  $1T$ -TaSe<sub>2</sub> polytype; however, non-quantitative amounts of  $2H$ -TaSe<sub>2</sub> and  $3R$ -TaSe<sub>2</sub> are also produced. Fortunately, the color differences of the polytypes allows for easy mechanical separation of the crystals.  $1T$ -TaSe<sub>2</sub> crystals are isolated by hand from crystals of  $2H,3R$ -TaSe<sub>2</sub> due to the distinct golden color of the  $1T$  form, as shown in Figure 4.2. Rapid quenching from a growth temperature of 500 °C to 850 °C results primarily in  $3R$ -TaSe<sub>2</sub> with some  $2H$ -TaSe<sub>2</sub>.<sup>56</sup>

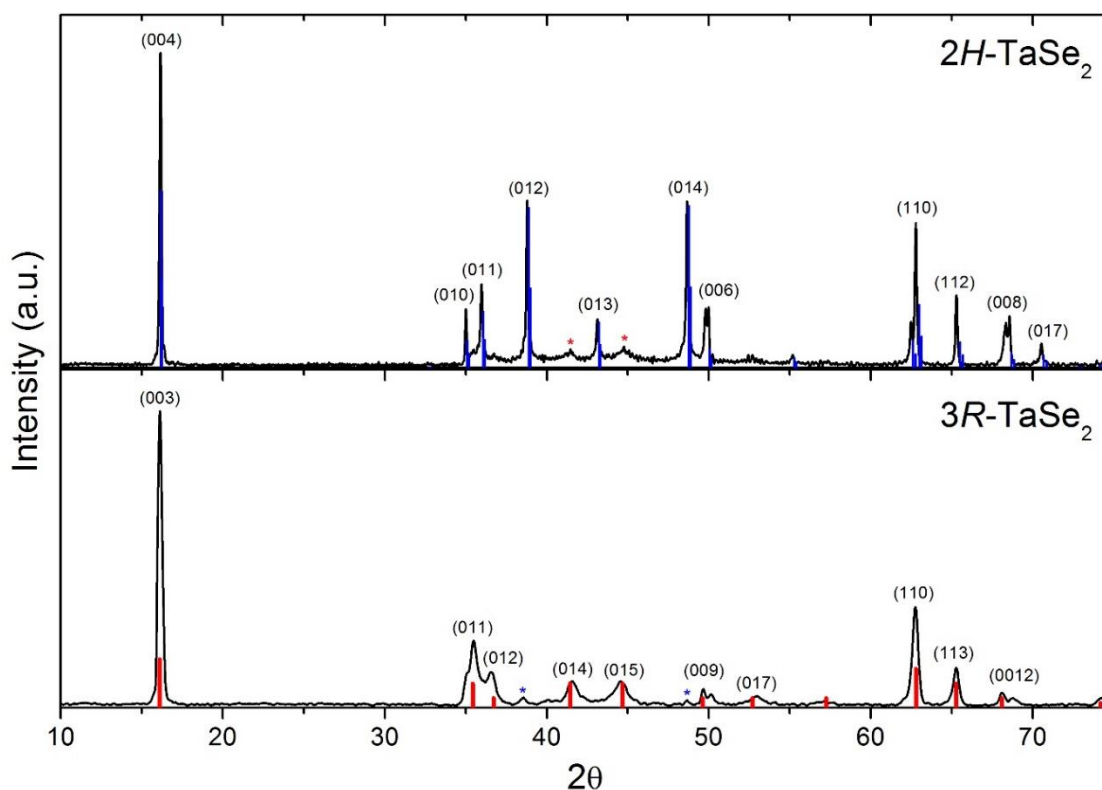


**Figure 4.5.** PXRD pattern of the  $3R$ -TaSe<sub>2</sub> precursor, showing broad peaks that indicate small crystallites, and  $2H$ -TaSe<sub>2</sub> product after CVT, showing defined peaks that indicate larger crystalline domains. Droplines are known peak positions for  $2H$ -TaSe<sub>2</sub> (blue) and  $3R$ -TaSe<sub>2</sub> (red). The asterisks indicate trace amounts of alternate polytypes.

The crystals were further examined by energy-dispersive X-ray spectroscopy (EDS) and wave-dispersive spectroscopy (WDS) using electron probe microanalysis (EPMA). Theoretically, TaSe<sub>2</sub> is comprised of 46.60% of Se and 53.40% Ta by weight. The EDS data given in Table 4.1 shows a weight percentage of 43.23% for Se and 56.77% for Ta, which largely matches the theoretical weight percentages. WDS through EPMA, which gives more precise measurements, matched weight percentages of 43.60% for Se and 51.86% for Ta. Calculating for atomic percentage, the theoretical percentages are 66.00% for Se and 33.00% for Ta, giving a 2:1 ratio of Se:Ta. Both EDS and EPMA, once again, agree with the theoretical percentages (Table 4.1). EDS yields experimental atomic percentages of 63.57% Se and 36.43% Ta (1.74:1), and EPMA atomic percentages of 67.80% Se and 32.24% Ta (2.10:1). These results indicate that after CVT growth the crystals remain pristine with no oxide impurities or inclusion of the transport agent.

**Table 4.1. Comparison of EDS and EPMA data from 2H-TaSe<sub>2</sub> crystals. Reprinted with permission from J. Appl. Phys. 114, 204301 (2013). Copyright 2013, AIP Publishing LLC.**

	Theoretical weight %	Experimental weight %		Theoretical atomic %	Experimental atomic %	
		EPMA	EDS		EPMA	EDS
Se	46.60	47.60	43.23	66.00	67.80	63.57
Ta	53.40	51.86	56.77	33.00	32.24	36.43
Total weight %	100.0	99.46	100.0	—	—	—
Se/Ta	—	—	—	2.00	2.10	1.74

Care must be taken not to use an excessive amount of transport agent during CVT crystal growth. Figure 4.6 shows SEM images of 1T-TaSe<sub>2</sub> crystals produced by CVT with varying amounts of I<sub>2</sub> transport agent. The crystals grown using an ideal amount of I<sub>2</sub> transport agent (3–5 mg/cm<sup>3</sup>) show smooth surfaces and edge sites, and can be shown to be composed of only tantalum and selenium. When excess I<sub>2</sub> is used (6–10 mg/cm<sup>3</sup>), small ribbons are formed at the edge sites

on a large percentage of the crystals. In order to determine the composition of the ribbons, the crystals were sonicated in isopropyl alcohol to disassociate them from the edges of the TaSe<sub>2</sub> crystal and the dispersion was dropcast onto a copper TEM grid and observed with SEM. Isolated ribbon fragments were seen, and EDS analysis gave atomic percentages of ~24% tantalum, ~68% selenium, and ~8% iodine. Additionally, long, unbroken ribbons were also observed from the same sample, and EDS analysis gave atomic percentages of ~47% tantalum, ~48% selenium, and ~5% iodine. A small percentage of crystals grown with the ideal amount of I<sub>2</sub> transport agent (3–5 mg/cm<sup>3</sup>) show some iodine-doped TaSe<sub>2</sub> ribbons. In order to produce pristine crystals of TaSe<sub>2</sub>, it is important to consider not only the stoichiometric ratio of tantalum and selenium but also the amount of I<sub>2</sub> transport agent used during CVT growth.

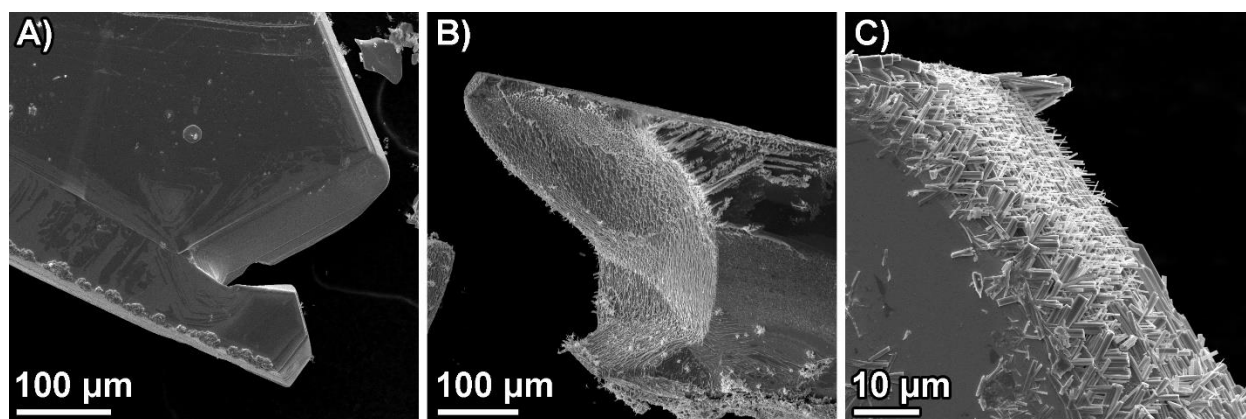


**Figure 4.6.** SEM images of 1T-TaSe<sub>2</sub> after CVT growth with (A) the ideal amount of I<sub>2</sub> transport agent (3–5 mg/cm<sup>3</sup>) and (B, C) excess I<sub>2</sub> (6–10 mg/cm<sup>3</sup>). The ribbons in B and C correspond to iodine-doped TaSe<sub>2</sub>.

#### *Surface Oxidation and Polymorph Transformation*

Because oxidation negatively affects the performance of materials used in electronic devices, the extent of oxidation in a material is important to quantify. In order to further understand surface oxidation of bulk samples of MX<sub>2</sub> systems, studies using Raman spectroscopy, EDS, and

SEM were carried out. Past reports utilizing thermogravimetric analysis indicate that many bulk  $\text{MX}_2$  materials have oxidation temperatures exceeding  $700\text{ }^\circ\text{C}$ .<sup>60</sup> However, such high temperatures are not relevant to typical electronic device applications. Thus, we studied oxidation at a range of temperatures (100, 200, 300, 500, and  $700\text{ }^\circ\text{C}$ ) with varying times to understand when oxidation occurs and to what extent.

Figure 4.7 shows the Raman spectra of  $1T\text{-TaSe}_2$  crystals from CVT heated to various temperatures for 1 hour in air. No noticeable change in peak position or width is seen for the samples heated to  $100\text{ }^\circ\text{C}$  and  $200\text{ }^\circ\text{C}$ . However, after being heating to  $300\text{ }^\circ\text{C}$  for an hour, a distinct shoulder peak is seen in the spectrum at  $250\text{ cm}^{-1}$ . Heating crystals to  $500\text{ }^\circ\text{C}$  for an hour, the peak at  $250\text{ cm}^{-1}$  broadens and now dominates the spectrum. Once a temperature of  $700\text{ }^\circ\text{C}$  is reached, the pattern entirely matches a previously reported spectrum for tantalum oxide ( $\text{Ta}_2\text{O}_5$ ).<sup>61</sup> Because the shift in peak position and broadening of peak width began at  $300\text{ }^\circ\text{C}$ , it can be concluded that surface oxidation occurs after 1 hour at temperatures as low as  $300\text{ }^\circ\text{C}$ .

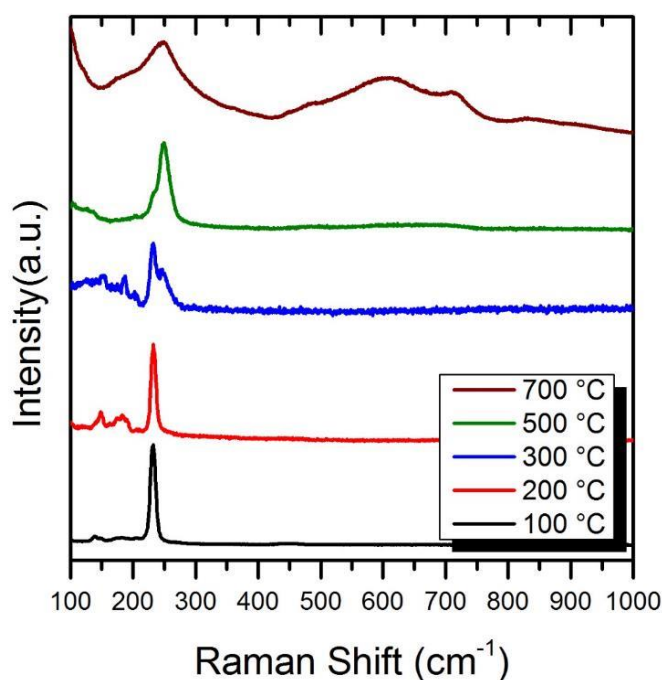


**Figure 4.7.** Raman spectra of  $1T\text{-TaSe}_2$  after exposure to ambient atmosphere at various temperatures for 1 hour.

Next, we studied prolonged heating at 100 and 200 °C in air. After 6 hours of heating 1*T*-TaSe<sub>2</sub> samples at 100 °C, the Raman spectrum remained unchanged. EDS was performed on the surface and edge sites, with data given in Table 4.2. The surface showed no oxygen content and maintained a 2:1 ratio of selenium to tantalum. At the edge, however, EDS shows that 39.9% of atoms were oxygen, indicating that oxidation occurs at the edge sites under these conditions. As coordinatively unsaturated metal atoms are present at edge sites, oxidation is more likely to readily occur there, as suggested by the EDS results.

**Table 4.2. Atomic percentages determined by EDS for surface and edge sites of TaSe<sub>2</sub> samples heated to 100 or 200 °C under ambient atmosphere for 6 hours.**

		Surface			Edge		
		Ta	Se	O	Ta	Se	O
1 <i>T</i> -TaSe <sub>2</sub>	100 °C	32.6%	67.4%	0.0%	19.6%	40.5%	39.9%
	200 °C	24.3%	55.4%	20.3%	24.8%	34.4%	40.8%
3 <i>R</i> ,2 <i>H</i> -TaSe <sub>2</sub>	100 °C	28.1%	71.9%	0.0%	20.2%	43.9%	35.9%
	200 °C	30.4%	58.7%	10.9%	23.3%	46.6%	30.1%

After 6 hours of heating 1*T*-TaSe<sub>2</sub> samples at 200 °C in air, small crystallites were observed to have grown from the edge sites (Figure 4.8). EDS collected from the surface now shows some oxidation, with an atomic percentage of oxygen of 20.3%. Further oxidation was observed at the crystal edge (40.8 at.% oxygen). The crystalline protrusions were found to be 95.5 at.% of selenium, indicating that as the 1*T*-TaSe<sub>2</sub> is oxidized the excess selenium is removed from the crystal and deposited on the outer surface (mainly at edge sites).

Crystals comprised of a mixture of two polytypes, 3*R*,2*H*-TaSe<sub>2</sub>, were also heated in air for 6 hours at 100 °C and 200 °C. As with the 1*T*-TaSe<sub>2</sub> form, at 100 °C no surface oxidation was

observed by EDS analysis. However, a similar amount of oxidation was observed at the edge sites (35.9 at.% oxygen). After heating  $3R,2H$ -TaSe<sub>2</sub> crystals to 200 °C for 6 hours, a very minor amount of surface oxidation is observed (10.9 at.% oxygen) and edge sites again showed the presence of some surface oxidation (30.1 at.% oxygen). However, the SEM image in Figure 4.9 clearly show crystals seemingly grown from defects and edges of the crystals. In contrast to the protrusions found on the  $1T$ -TaSe<sub>2</sub> crystals heated at 200 °C, these protrusions showed little selenium (6.6 at.%) and were mostly composed of tantalum (45.8 at.%) and oxygen (47.6 at.%).

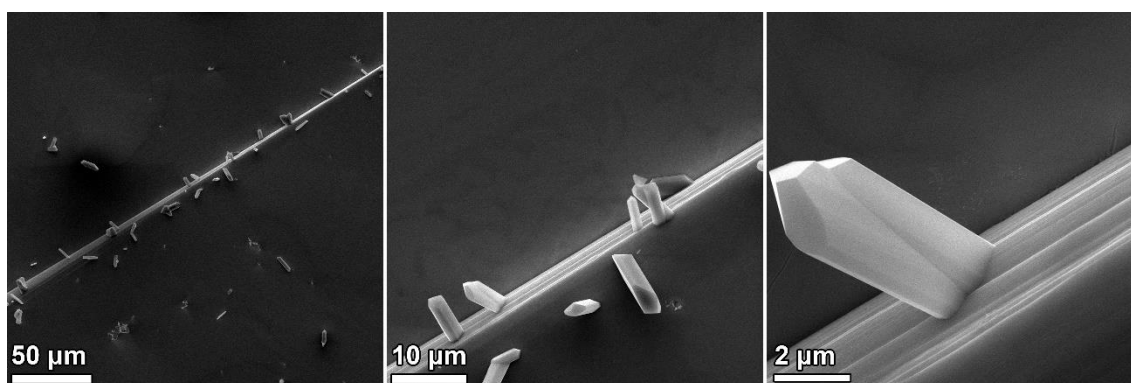


**Figure 4.8.**  $1T$ -TaSe<sub>2</sub> crystals heated under ambient atmosphere at 200 °C for 6 hours. The crystals on the step edge were determined by EDS analysis to be selenium.

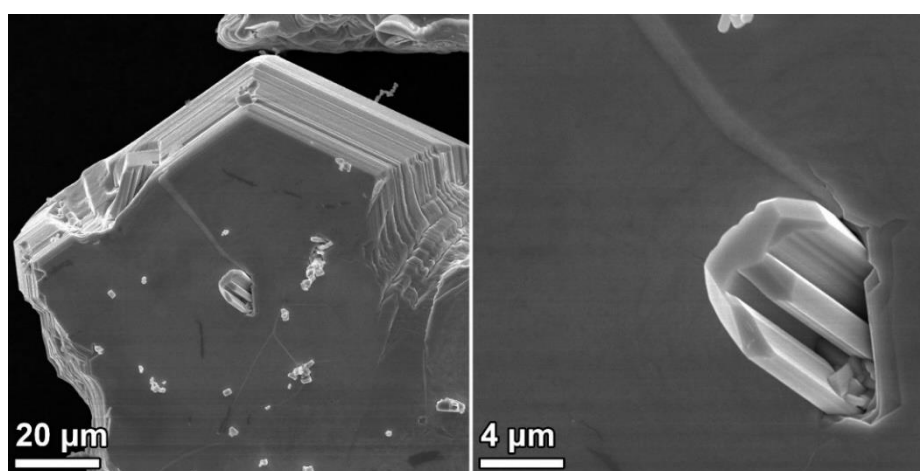


**Figure 4.9.** SEM images of  $3R,2H$ -TaSe<sub>2</sub> crystals heated under ambient atmosphere at 200 °C for 6 hours. The crystals protruding from defect or edge sites were determined by EDS analysis to be crystals of tantalum oxide.

It is interesting to note that different polytypes show different oxidation behaviors. As discussed above, during oxidation the  $1T$ -TaSe<sub>2</sub> polytype forms a layer of tantalum oxide and pushes excess selenium out from the structure, which then crystallizes on edge sites. In contrast, the  $3R,2H$ -TaSe<sub>2</sub> polytype forms protrusions of tantalum oxide at edge and defect sites.

Though a minor amount of surface oxidation may occur under ambient conditions, it is easily removed through mechanical delamination (i.e. Scotch tape method). With the help of our collaborators in the Stickney lab we examined the surface oxidation of a  $2H$ -TaSe<sub>2</sub> sample after storage in ambient conditions. As shown in Figure 4.10, X-ray photoelectron spectroscopy (XPS) of the sample showed peaks corresponding to the native oxide of tantalum (Ta<sub>2</sub>O<sub>5</sub>).<sup>30</sup> However, when the surface layers of the crystal are removed by delamination, the oxide peaks are no longer evident. This indicates the oxide layer forms only on the exposed surface and does not penetrate through the crystal. Therefore, TaSe<sub>2</sub> oxidation during long-term storage in ambient conditions can be removed by simply delaminating the top layer of the crystal.

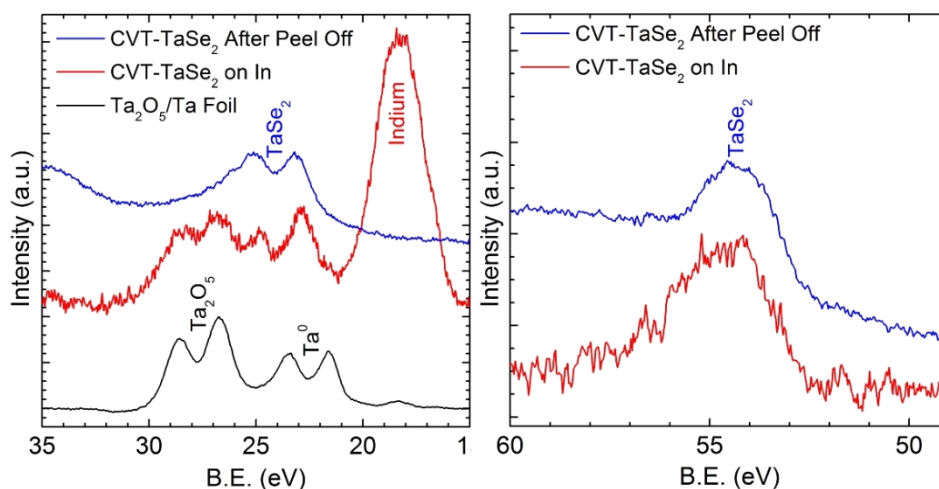


**Figure 4.10.** The XPS spectra on the left show the Ta 4f photoelectric peaks from  $2H$ -TaSe<sub>2</sub> crystals pressed on indium foil before (red) and after (blue) the removal of surface layers. The spectrum of Ta<sub>2</sub>O<sub>5</sub> on Ta foil (black) is included for reference. The XPS spectra on the right show the Se 3d photoelectric peaks from  $2H$ -TaSe<sub>2</sub> crystals before (red) and after (blue) removal of surface layers. Reprinted with permission from J. Appl. Phys. **114**, 204301 (2013). Copyright 2013, AIP Publishing LLC.

After 4 months of storage in ambient conditions, golden crystals of  $1T$ -TaSe<sub>2</sub> turned gray in color. When the crystals were observed by SEM, as shown in Figure 4.11, the surface of the aged crystals appeared to be much rougher than that of the smooth surfaces of freshly grown  $1T$ -TaSe<sub>2</sub> crystals. When the grey surface is scratched, the golden color becomes visible again at the newly exposed surface. In addition, the newly exposed surface showed the same smooth appearance as the freshly grown  $1T$ -TaSe<sub>2</sub> crystals. EDS analysis of the aged surface gave atomic percentages of ~29% tantalum, ~55% selenium, and ~16% oxygen. EDS analysis of the newly exposed surface gave atomic percentages of ~33% tantalum, ~63% selenium, and ~4% oxygen, indicating that oxidation is mainly confined to the surface.

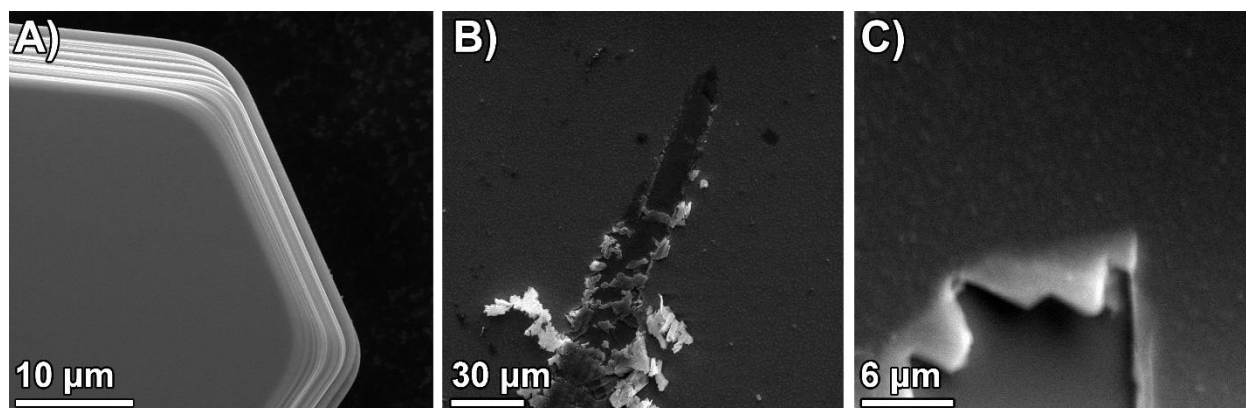


**Figure 4.11.** SEM images of (A) freshly grown  $1T$ -TaSe<sub>2</sub> crystals and (B, C)  $1T$ -TaSe<sub>2</sub> crystals after exposure to ambient conditions for 4 months and scratched to remove the surface layer. After aging the crystals appear gray in color, in contrast to the golden color of freshly grown  $1T$ -TaSe<sub>2</sub>; however, after scratching the golden luster is once again visible in the newly exposed regions.

In order to further examine the change in the crystal surface after prolonged exposure to ambient conditions, Raman spectroscopy was performed on the aged surface and on the newly exposed surface (Figure 4.12). The newly exposed surface primarily shows peaks corresponding to the  $1T$ -TaSe<sub>2</sub> form at 152, 174, 185, and 192  $\text{cm}^{-1}$ . Smaller peaks at 208 and 235  $\text{cm}^{-1}$  are also observed in the spectra of the newly exposed surface, which correspond to a minor amount of the

$2H$ -TaSe<sub>2</sub> polytype in the sample. This pattern matches the pattern of freshly grown  $1T$ -TaSe<sub>2</sub> crystals. The aged surface, on the other hand, showed much larger peaks corresponding to the  $2H$ -TaSe<sub>2</sub> polytype than the  $1T$ -TaSe<sub>2</sub> polytype. Thus, after prolonged exposure to ambient conditions, the surface of the  $1T$ -TaSe<sub>2</sub> crystals transform to the  $2H$ -TaSe<sub>2</sub> polytype—as well as oxidizes. This conclusion is supported by the obvious color change from golden to gray after exposure, and the exposure of the golden color after scratching the crystals to reveal a fresh surface.

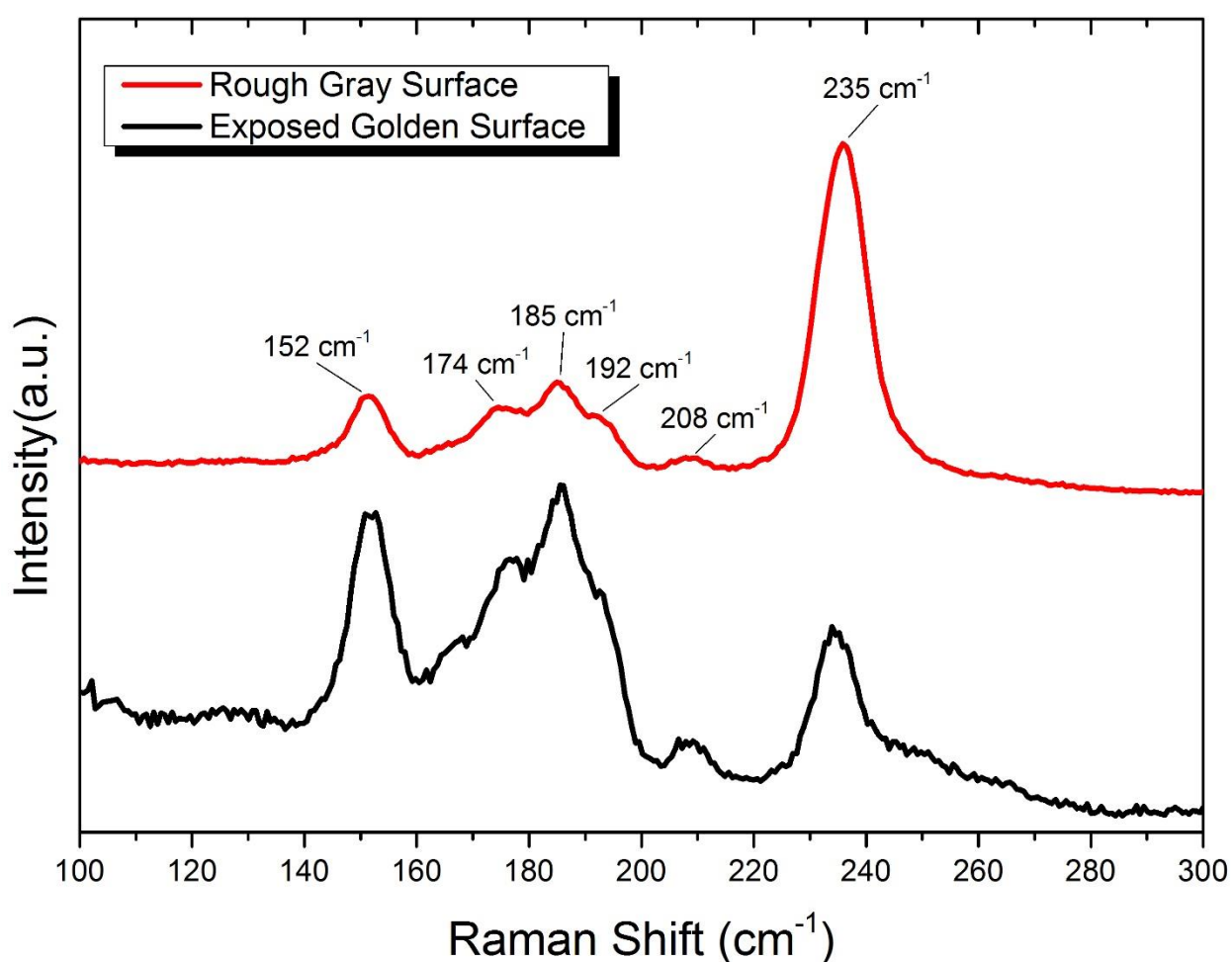


**Figure 4.12.** Raman spectra of  $1T$ -TaSe<sub>2</sub> crystals after exposure to ambient conditions for 4 months (red) and the newly exposed golden surface (black).

These studies on the surface of heated and aged TaSe<sub>2</sub> crystals indicate that, if not stored under an inert atmosphere at ambient temperature, TaSe<sub>2</sub> crystals will become impure over time either through oxidation or transformation to a different polytype. However, both of these conversions occur at the crystal surface, and thus the pristine inner crystal can be exposed again by removal of the surface layers through methods such as delamination.

### *Exfoliation into Nanosheets*

Though high quality nanosheets can be obtained via the Scotch tape method of mechanical delamination, this method is unsuitable for obtaining large quantities of nanosheets with large surface areas. Therefore, exfoliation methods have been developed as an alternative method for obtaining nanosheets and few-layer samples. One method for obtaining exfoliated nanosheets of MX<sub>2</sub> involves lithium intercalation.<sup>53</sup> When MX<sub>2</sub> samples are dispersed in solution along with an organolithium compound, such as *N*-butyllithium, lithium ions intercalate between the MX<sub>2</sub> layers. Subsequent reaction with water cleaves the layers and results in a collection of thin sheets. This method often reaches nanosheet yields nearing 100%.<sup>16</sup> However, intercalating a compound with lithium sometimes has the side effect of altering the material's polytype. When 2*H*-MoS<sub>2</sub> is intercalated with lithium, the structure transforms to the 1*T*-MoS<sub>2</sub> phase.<sup>62</sup> In TaS<sub>2</sub>, the opposite transition occurs, where 1*T*-TaS<sub>2</sub> is transformed into 2*H*-TaS<sub>2</sub> upon lithium intercalation.<sup>63</sup> In addition, exfoliation alters the orbital hybridization by removing s-p<sub>z</sub> orbital interactions between adjacent layers, which leads to the transition from an indirect bandgap (bulk) to a direct bandgap (nanosheet).<sup>64</sup>

Coleman et al. introduced a paradigm shift in exfoliation methods by exfoliating MX<sub>2</sub> nanosheets without intercalation through ultrasonication using a coordination solvent.<sup>65</sup> A

coordination solvent is used to aid in overcoming the van der Waals energy between the  $\text{MX}_2$  layers in order for exfoliation to occur.<sup>66</sup> The bulk material is first dispersed in a solvent with a surface energy similar to that of the material.<sup>67</sup> For example, *N*-methylpyrrolidone and *N*-vinylpyrrolidone are often used to exfoliate  $\text{TaSe}_2$  samples—typically, our lab uses a modified version of Coleman’s method where the  $\text{MX}_2$  sample is probe ultrasonicated for at least 1 hour. The sheets are then isolated from any remaining bulk crystals by centrifugation at low rpm. The supernatant, consisting of the nanosheets, is then centrifuged at high rpm to remove the nanosheets from the solvent which then are redispersed in the desired solvent. This method of exfoliation can produce very thin sheets with lateral dimensions reaching several hundred nanometers, as shown in the TEM image of a free-standing film of  $2H\text{-TaSe}_2$  in Figure 4.13. In addition, this exfoliation procedure does not change the polymorph of the  $\text{MX}_2$  (i.e.  $2H\text{-TaSe}_2$  remains  $2H\text{-TaSe}_2$ ). However, a marked change in the PXRD pattern is observed, as seen in Figure 4.14. The peaks are markedly broader upon exfoliation, which indicates a major reduction in the size of the material. The sample also demonstrates a preferred orientation ( $00\ell$ ) plane (the layer plane of the crystal), which specifies that exfoliation occurs along this ( $00\ell$ ) plane. Hence, the (002), (006), and (008) peaks in Figure 4.14 are greatly amplified as a result of this preferred orientation. Similarly, Figure 4.15 shows the PXRD pattern of  $1T\text{-TaSe}_2$  before and after exfoliation. Before exfoliation, directly after CVT growth, the material was mostly  $1T\text{-TaSe}_2$  with a small amount of  $2H\text{-TaSe}_2$ . After exfoliation, the sample remains in the  $1T\text{-TaSe}_2$  polytype and also shows a preferred orientation along the ( $00\ell$ ) series.

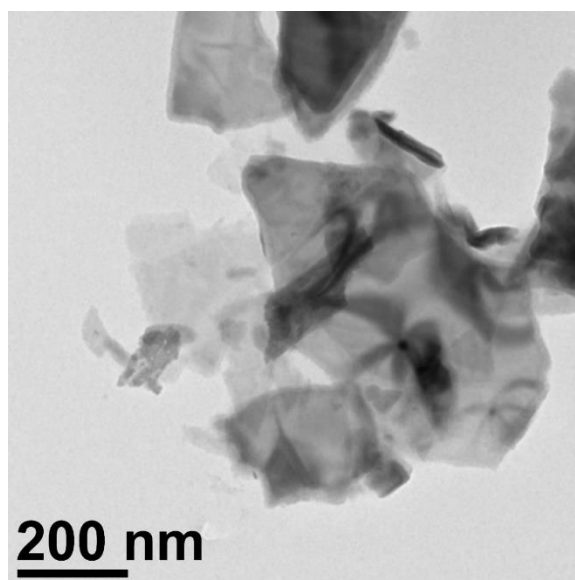


**Figure 4.13.** TEM image of free-standing  $2H\text{-TaSe}_2$  nanosheets produced by solvent-assisted exfoliation.

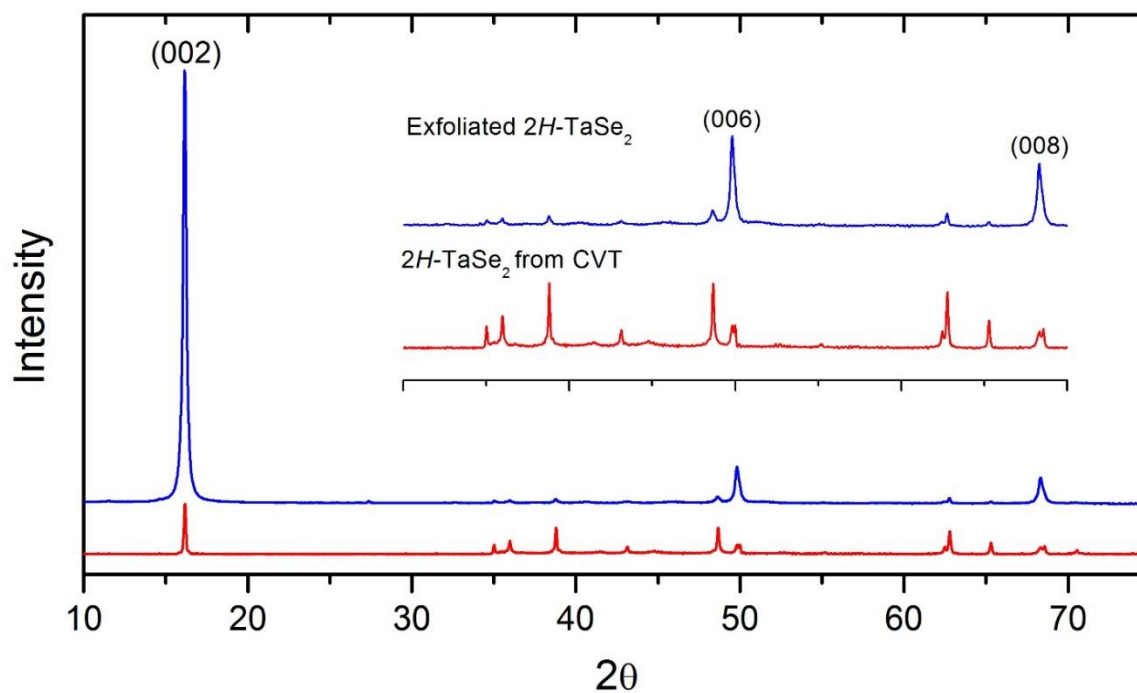


**Figure 4.14.** XRD patterns of  $2H\text{-TaSe}_2$  taken on the large crystal directly after CVT (red trace) and after exfoliation by a modified Coleman method (blue trace). Exfoliation occurs preferentially along the  $(00\ell)$  plane, as indicated by the large increase in the (002), (006), and (008) peaks.

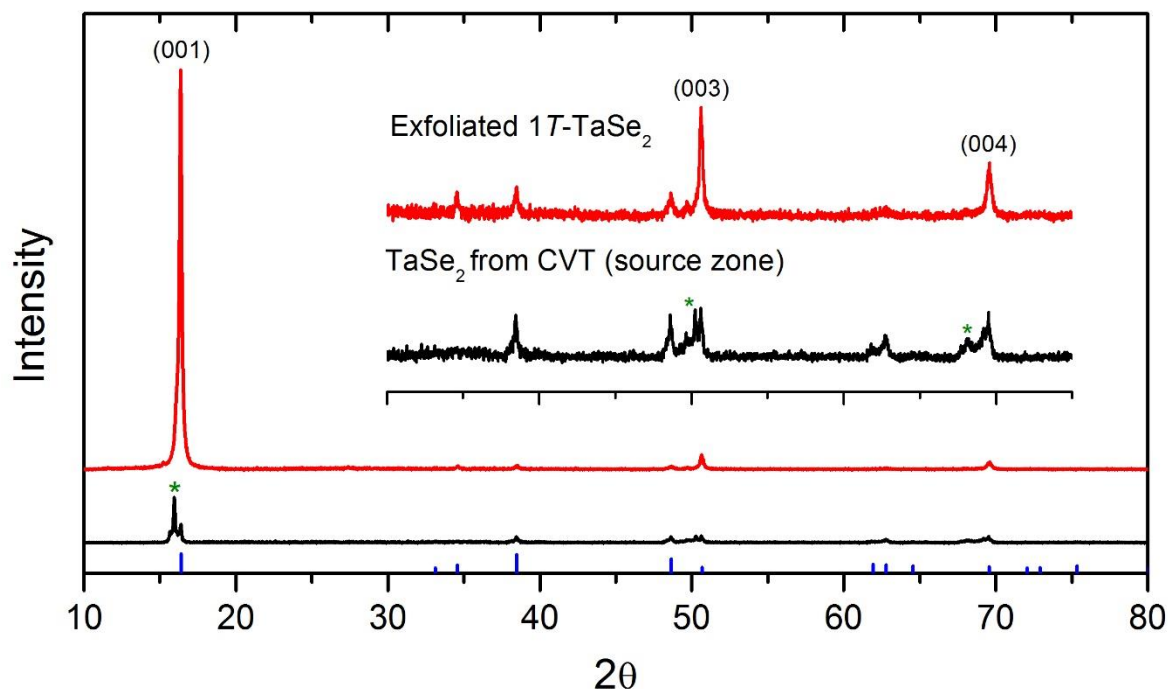


**Figure 4.15.** XRD patterns of 1T-TaSe<sub>2</sub> taken on the large crystal directly after CVT (black trace) and after exfoliation by a modified Coleman method (red trace). Exfoliation occurs preferentially along the (00 $l$ ) plane, as indicated by the large increase in the (001), (003), and (004) peaks. The peaks labeled with \* denote peaks corresponding to the 2H-TaSe<sub>2</sub> polytype.

Nanosheet dispersions can be processed into thin films using methods such as drop casting and layer-by-layer deposition. Once thin films are achieved, the unique nanoscale effects of MX<sub>2</sub> materials can then be explored. The following section discusses projects carried out by our collaborators at the University of California, Riverside, using TaSe<sub>2</sub> grown in our lab and exfoliated or delaminated by some of the methods described above. Because the bulk material is used to create flakes with nanometer-scale thickness, it is important to produce large, pristine, and high-quality bulk crystals in order to obtain high-quality nanosheets. In addition, the different polytypes have different electronic properties, such as varying bandgaps or the absence of a bandgap as well as CDWs that manifest at different temperatures. The quality of such crystals are determined using such analytical methods as PXRD, XPS, and EPMA, which were discussed in the previous sections. In addition, millimeter-sized crystals are desired so that flakes having lateral

dimensions in the micrometer range can be obtained by exfoliation and/or delamination. Micrometer length flakes are necessary in order to easily deposit two separate metal contacts on a single flake to fabricate a working electronic device for fundamental studies. The lateral dimensions and thickness of nanomaterials can be measured by microscopy methods such as SEM, TEM, and AFM. In addition, PXRD can be used to determine the preferred orientation, and thus the exfoliation plane of the nanosheet, as discussed above in the case of free-standing  $2H$ -TaSe<sub>2</sub> nanosheets.

## **Nanoscale Properties and Electrical Devices**

### *Thickness Measurements from Raman Spectroscopy*

With nanoscale materials, the thickness has a large influence on the material's mechanical and electrical properties. Thus, it is useful to have a simple method to measure the thickness. Yan et al. developed a simple nanometrology tool using Raman spectroscopy to quantify sheet thickness by comparing the ratio of peak intensities from the Si substrate (at 522 cm<sup>-1</sup>) and the E<sub>2g</sub> peak of  $2H$ -TaSe<sub>2</sub> (at 207 cm<sup>-1</sup>).<sup>30</sup>

The Raman spectra of nine exfoliated films with thicknesses ranging from a few nanometers to over 250 nm are given in Figure 4.16a. Because the intensity of the Si peak is proportional to the penetration of the electron beam (interaction volume), the Si peak intensity increases with decreasing thickness of the  $2H$ -TaSe<sub>2</sub> film because a larger proportion of the electron beam penetrates through to the Si substrate. The ratio of the intensity of the Si peak to that of the E<sub>2g</sub> peak of  $2H$ -TaSe<sub>2</sub>,  $I_{Si}/I_{E_{2g}}$ , provides information about the exfoliated film thickness if a calibration curve is first determined by measuring the thickness by atomic force microscopy (AFM). As shown in Figure 4.16b,  $I_{Si}/I_{E_{2g}}$  exponentially decreased as the film thickness increased,

and the following equation was established by fitting the data:  $I_{\text{Si}}/I_{\text{E}_{2\text{g}}} = 11.2 \exp(-H/54.9) - 0.11$ , where  $H$  is the thickness in nanometers. This equation can be used as a calibration curve for future measurements of the thickness of  $2H$ -TaSe<sub>2</sub> films on Si substrates.

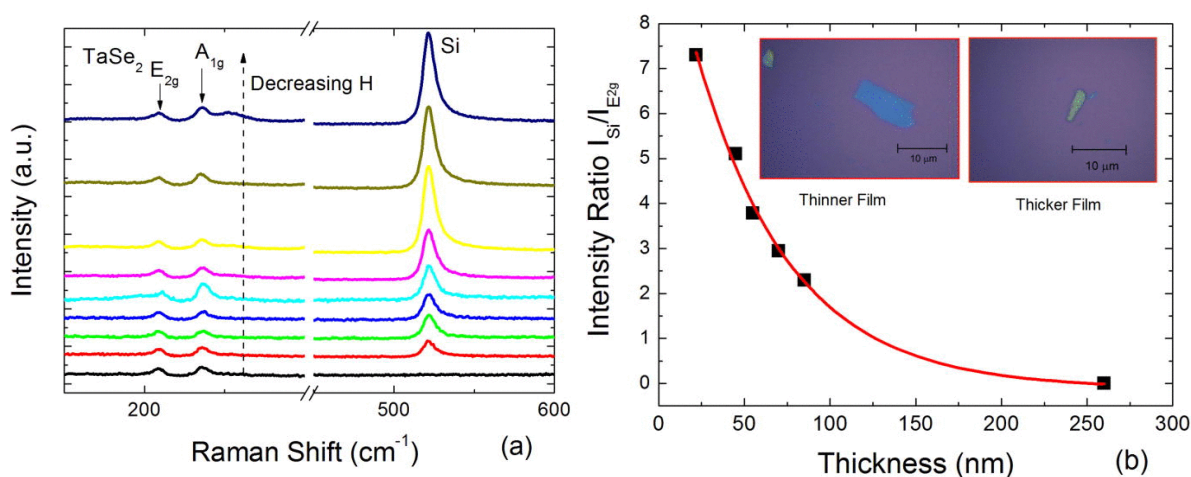


**Figure 4.16.** Raman spectra of exfoliated thin films of  $2H$ -TaSe<sub>2</sub> with thicknesses ranging from 30–260 nm on Si substrates (left). Plot of the ratios of the intensity of the Si peak to that of the  $2H$ -TaSe<sub>2</sub> E<sub>2g</sub> peak for the various film thicknesses (right). The insets show optical microscopy images of two flakes of  $2H$ -TaSe<sub>2</sub> with substantially different thickness. The thinner flakes appear blue in color whereas the thicker flakes appear yellow. Reprinted with permission from *J. Appl. Phys.* **114**, 204301 (2013). Copyright 2013, AIP Publishing LLC.

### *Temperature Effects and Thermal Conductivity*

Yan et al. also showed that temperature-dependent Raman spectroscopy is a facile method to determine the thermal conductivity of  $2H$ -TaSe<sub>2</sub> films,<sup>30</sup> which is important to consider when designing electronic devices. As the temperature increased, the peak positions of both the E<sub>2g</sub><sup>1</sup> and A<sub>1g</sub> modes shifted to lower wavenumbers. Plotting the Raman peak shifts against the various temperatures resulted in a linear dependency that allowed for the determination of first-order temperature coefficients ( $\Gamma$ ). The temperature coefficients  $\Gamma$  for the A<sub>1g</sub> and E<sub>2g</sub><sup>1</sup> modes were

determined to be  $-0.013 \text{ cm}^{-1}/^\circ\text{C}$  and  $-0.0097 \text{ cm}^{-1}/^\circ\text{C}$ , respectively, which qualitatively match those obtained for bulk  $2H\text{-TaSe}_2$ .<sup>49</sup>

The origin of heat conduction (phonon- or electron-based) was then determined using a field-effect transistor with  $2H\text{-TaSe}_2$  channels.<sup>30</sup> Figure 4.17 shows the channel of an 80 nm film of  $2H\text{-TaSe}_2$  connected by titanium and gold metal contacts, along with the corresponding current-voltage (I-V) curve. The thermal conductivity of the  $2H\text{-TaSe}_2$  channel was  $0.365 \text{ 1}/\Omega\text{m}$  while the contribution from electrons was only  $3 \times 10^{-6} \text{ W/mK}$ , which implies that heat conduction is dominated by phonons.

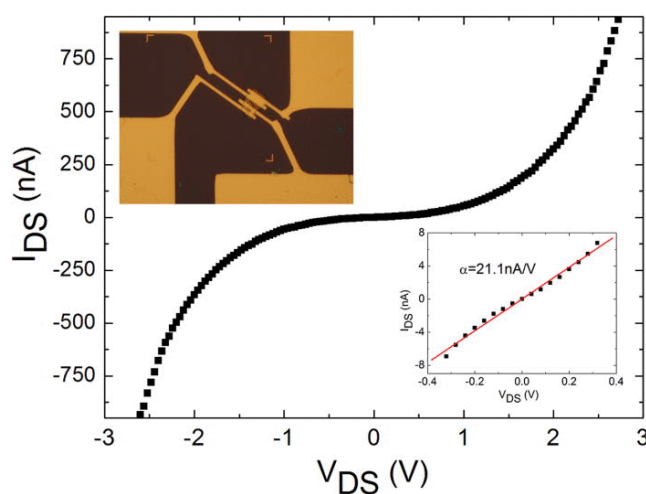


**Figure 4.17.** Current-voltage characteristic of a two-terminal device with a  $2H\text{-TaSe}_2$  channel. The upper inset shows an optical microscopy image of the device. The lower inset shows the small-bias region of I-V curve used to determine the resistivity of the  $2H\text{-TaSe}_2$  film. Reprinted with permission from J. Appl. Phys. **114**, 204301 (2013). Copyright 2013, AIP Publishing LLC.

### *All-Metallic Devices*

Renteria et al. examined the electrical and optical characteristics of all-metallic devices made from  $2H\text{-TaSe}_2$ , shown in Figure 4.18.<sup>31</sup> The  $2H\text{-TaSe}_2$  polytype was used since, like graphene, this material has no bandgap.<sup>68</sup> Thus, the I-V characteristics of such devices are different

from the characteristics of semiconductor-based transistors. Devices made from  $2H$ -TaSe<sub>2</sub> showed strong gating effects, low leakage currents, and transconductance near the voltage threshold. Even at room temperature, the devices acted as switches due to the well-defined on/off transition from near-zero current to high current. At low temperature (100 K), the on/off transition was even more pronounced.

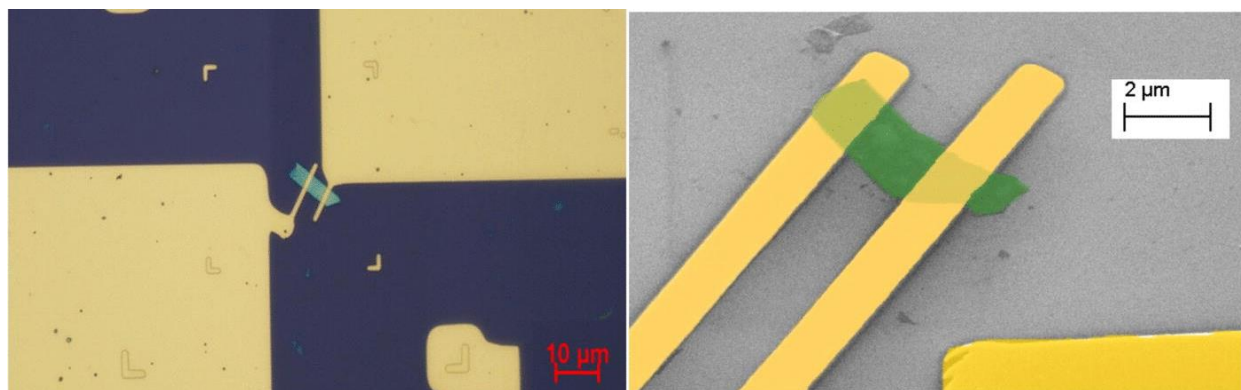


**Figure 4.18.** Optical (left) and SEM (right) images of representative all-metallic devices with  $2H$ -TaSe<sub>2</sub> thin-film channels and Ti/Au source and drain contacts. The pseudo colors in the SEM image were used for clarity: yellow corresponds to metal contacts and green corresponds to  $2H$ -TaSe<sub>2</sub>. Reprinted with permission from J. Appl. Phys. **115**, 034305 (2014). Copyright 2014, AIP Publishing LLC.

The I-V characteristics of the devices were also affected by exposure to light, where the on/off transition was more pronounced under light than in the dark and the conduction onset shifted to a higher voltage. This is in contrast with conventional photoresistors where exciton generation under light typically induces an increase in current. However, this behavior is not unprecedented. Ogawa and Miyano have reported charge density wave devices that also shifted to larger voltage thresholds under light.<sup>69</sup> In addition, the size of the  $2H$ -TaSe<sub>2</sub> channel (the active area of  $2H$ -TaSe<sub>2</sub> in between the source and drain electrodes) was found to shift the on/off threshold. The sharp on/off transition and increase in threshold voltage in response to light illustrates how thin

films of  $2H$ -TaSe<sub>2</sub> could potentially be used in optoelectronic devices. Furthermore, future devices could use the thickness-dependent threshold shift to control the on/off voltage, possibly allowing for a complementary logic pair by using two different sized channels.

### *Charge Density Waves*

Samnakay et al. used temperature-dependent Raman spectroscopy to probe the commensurate to incommensurate CDW transition in  $1T$ -TaSe<sub>2</sub> thin films in by examining any new peaks arising at higher temperatures.<sup>37</sup> Using the aforementioned Raman nanometrology technique, the thickness of the sample was determined by comparing the intensity of the Si substrate peak to that of the  $A_{1g}$  peak of  $1T$ -TaSe<sub>2</sub>. Figure 4.19 shows the Raman spectra of a 150 nm  $1T$ -TaSe<sub>2</sub> film over a temperature range of 213 to 493 K. At room temperature prominent peaks were observed at  $\sim 187\text{ cm}^{-1}$  ( $A_{1g}$ ) and  $\sim 177\text{ cm}^{-1}$  ( $E_{2g}$ ). Peaks at  $210\text{ cm}^{-1}$  and  $236\text{ cm}^{-1}$  were also observed due to minor impurities of  $2H$ -TaSe<sub>2</sub> present in the sample. The peak at  $154\text{ cm}^{-1}$  corresponds to phonon modes, i.e. periodic vibrations in the crystal lattice.

At 473 K, the  $A_{1g}$  and  $E_{2g}$   $1T$ -TaSe<sub>2</sub> peaks merged into a single broad peak. At the same time, the peak at  $154\text{ cm}^{-1}$  broadened and decreased in intensity. These spectral changes were due to lattice distortions at the commensurate to incommensurate CDW transition temperature, which disrupted the crystal periodicity. Upon cooling, the spectrum returned to its previous form with the reappearance of distinct peaks at  $154$ ,  $177$ , and  $187\text{ cm}^{-1}$ , proving that the spectral change was due to lattice distortions and not to irreversible events such as surface oxidation or contamination. When the same analysis was conducted on a film with a thickness of 35 nm, an identical spectral transformation was observed upon heating; however, the transition temperature decreased to 413 K. Again, this transformation was reversible.

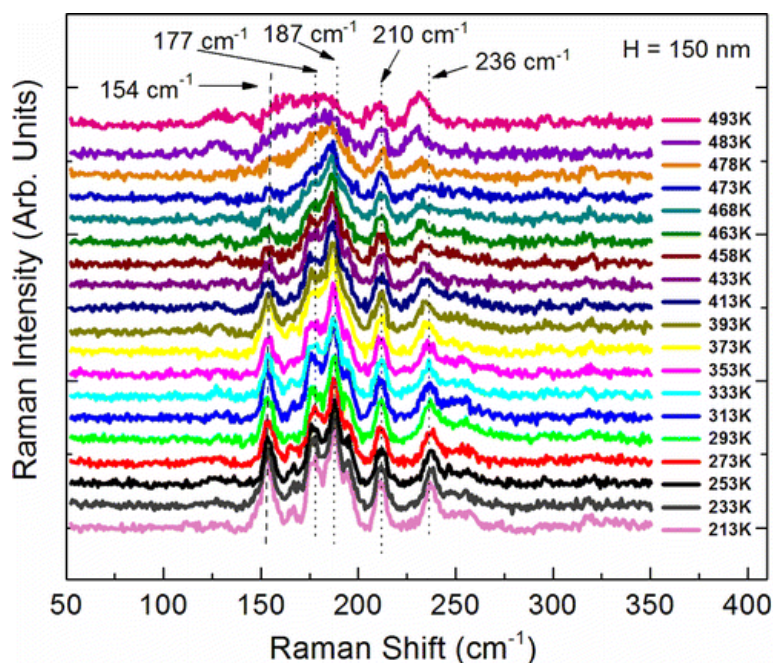


**Figure 4.19.** Raman spectra of the 150 nm thick 1T-TaSe<sub>2</sub> film observed at temperatures between 213–493 K. Note that above  $T_{IC} = 473$  the spectrum is strongly modified owing to the loss of translational symmetry. Reprinted with permission from *Nano Lett.* **15**, 2965 (2015). Copyright 2015 American Chemical Society.

## Conclusion

Transition metal dichalcogenides (MX<sub>2</sub>) display unique mechanical and electrical properties when reduced to the nanoscale regime. In this chapter, particular interest was paid to tantalum diselenide (TaSe<sub>2</sub>). TaSe<sub>2</sub> consists of layered Se-Ta-Se units held together by van der Waals forces, which can be disrupted to separate the layers into individual nanosheets. A variety of methods exist to separate the bulk material into few- or monolayer samples. Sonication with a coordinating solvent produces the largest quantity of pristine nanosheets. In order to obtain nanosheets, TaSe<sub>2</sub> crystals must first be synthesized in bulk by heating stoichiometric amounts of elemental samples. Then, chemical vapor transport is used to produce single crystals suitable for mechanical exfoliation. TaSe<sub>2</sub> can be formed in several polytypes (1T, 2H, or 3R) that have

different coordination environments. The cooling conditions determine which polytype is formed during CVT.

If left in ambient conditions over long periods of time, oxidation will occur on the surface of TaSe<sub>2</sub>. Rapid oxidation occurs upon heating in air at temperatures in excess of 300 °C. In addition, heating at lower temperatures (100 °C and 200 °C) for several hours induces oxidation. Oxidation mainly occurs at edge sites, likely due to the presence of coordinatively unsaturated metal atoms. Additionally, if 1*T*-TaSe<sub>2</sub> crystals are stored in ambient conditions for several months, the surface layer is transformed to the 2*H*-TaSe<sub>2</sub> polytype. However, both surface oxidation and polytype transformation is restricted to the crystal surface and can be removed by delaminating surface layers.

Collaborators at the University of California, Riverside, used our 2*H*-TaSe<sub>2</sub> and 1*T*-TaSe<sub>2</sub> samples in various applications. Yan et al. showed that the film thickness of 2*H*-TaSe<sub>2</sub> can be measured by Raman spectroscopy after setting up a calibration curve.<sup>30</sup> In addition, our collaborators also probed the interesting electronic properties of 2*H*-TaSe<sub>2</sub> thin films. For example, Renteria et al. made electrically gated devices from thin films of 2*H*-TaSe<sub>2</sub> that displayed strongly non-linear current voltage (I-V) characteristics.<sup>31</sup> Furthermore, the gate voltage was tuned to produce an abrupt change from highly resistive to conductive in the drain-source current, indicating potential applications as switches in logic circuits. The on/off voltage transition was found to be dependent on both the channel size and the presence of light. Samnakay et al. used temperature-dependent Raman to study commensurate to incommensurate charge density wave (CDW) transition in thin films of 1*T*-TaSe<sub>2</sub>.<sup>37</sup> As the temperature increased, peaks corresponding to 1*T*-TaSe<sub>2</sub> broadened and decreased in intensity, indicating the CDW transition. The transition

temperature was shown to be dependent on the film thickness, as thinner films resulted in lower transition temperatures.

The thickness of tantalum diselenide influences a number of electronic properties, including the ability to tune both the gate voltage in field-effect transistors and the charge density wave transition temperature. Thus, the thickness must be well defined in optimized device structures. In addition, the material polytype also influences properties, including oxidation behavior. The polytype can be controlled by synthetic parameters or through lithium intercalation. Tuning the polytype, along with the thickness, represents further opportunities for the creation of novel materials for electronic devices. By carefully controlling the material synthesis and exfoliation and obtaining a better understanding of material properties, tantalum diselenide and other transition metal dichalcogenides have the potential to greatly impact the world of electronics.

## References

1. Novoselov, K. S.; Geim, A. K.; Morozov, S. V.; Jiang, D.; Katsnelson, M. I.; Grigorieva, I. V.; Dubonos, S. V.; Firsov, A. A. *Nature* **2005**, 438, (7065), 197-200.
2. Zhang, Y. B.; Tan, Y. W.; Stormer, H. L.; Kim, P. *Nature* **2005**, 438, (7065), 201-204.
3. Schwierz, F. *Nature Nanotechnology* **2010**, 5, (7), 487-496.
4. Liu, G.; Stillman, W.; Romyantsev, S.; Shao, Q.; Shur, M.; Balandin, A. A. *Appl. Phys. Lett.* **2009**, 95, (3).
5. Balandin, A. A. *Nature Nanotechnology* **2013**, 8, (8), 549-555.
6. Novoselov, K. S.; Geim, A. K.; Morozov, S. V.; Jiang, D.; Zhang, Y.; Dubonos, S. V.; Grigorieva, I. V.; Firsov, A. A. *Science* **2004**, 306, (5696), 666-669.
7. Yang, X.; Liu, G.; Balandin, A. A.; Mohanram, K. *Acs Nano* **2010**, 4, (10), 5532-5538.
8. Yang, X.; Liu, G.; Rostami, M.; Balandin, A. A.; Mohanram, K. *Ieee Electron Device Letters* **2011**, 32, (10), 1328-1330.
9. Teweldebrhan, D.; Balandin, A. A. *Appl. Phys. Lett.* **2009**, 94, (1).
10. Hossain, M. Z.; Romyantsev, S. L.; Shahil, K. M. F.; Teweldebrhan, D.; Shur, M.; Balandin, A. A. *Acs Nano* **2011**, 5, (4), 2657-2663.
11. Khan, J.; Nolen, C. M.; Teweldebrhan, D.; Wickramaratne, D.; Lake, R. K.; Balandin, A. A. *Appl. Phys. Lett.* **2012**, 100, (4).
12. Chianelli, R. R.; Siadati, M. H.; De la Rosa, M. P.; Berhault, G.; Wilcoxon, J. P.; Bearden, R.; Abrams, B. L. *Catalysis Reviews* **2006**, 48, (1), 1-41.
13. McBride, K. L.; Head, J. D. *Int. J. Quantum Chem* **2009**, 109, (15), 3570-3582.
14. Lauritsen, J. V.; Bollinger, M. V.; Lægsgaard, E.; Jacobsen, K. W.; Nørskov, J. K.; Clausen, B. S.; Topsøe, H.; Besenbacher, F. *J. Catal.* **2004**, 221, (2), 510-522.

15. Lee, C.; Li, Q.; Kalb, W.; Liu, X.-Z.; Berger, H.; Carpick, R. W.; Hone, J. *Science* **2010**, 328, (5974), 76-80.
16. Eda, G.; Yamaguchi, H.; Voiry, D.; Fujita, T.; Chen, M.; Chhowalla, M. *Nano Lett.* **2011**, 11, (12), 5111-5116.
17. Sundaram, R. S.; Engel, M.; Lombardo, A.; Krupke, R.; Ferrari, A. C.; Avouris, P.; Steiner, M. *Nano Lett.* **2013**, 13, 1416.
18. Radisavljevic, B.; Radenovic, A.; Brivio, J.; Giacometti, V.; Kis, A. *Nature Nanotechnology* **2011**, 6, (3), 147-150.
19. Radisavljevic, B.; Kis, A. *Nat. Mater.* **2013**, 12, 815.
20. Lembke, D.; Kis, A. *ACS Nano* **2012**, 6, 10070.
21. Lembke, D.; Bertolazzi, S.; Kis, A. *Acc. Chem. Res.* **2015**, 48, (1), 100-110.
22. Ataca, C.; Şahin, H.; Ciraci, S. *J. Phys. Chem. C* **2012**, 116, 8983.
23. Bertolazzi, S.; Brivio, J.; Kis, A. *ACS Nano* **2011**, 5, (12), 9703-9709.
24. Liu, X.; Hu, J.; Yue, C.; Della Fera, N.; Ling, Y.; Mao, Z.; Wei, J. *ACS Nano* **2014**, 8, (10), 10396-10402.
25. Luo, H.; Xie, W.; Tao, J.; Inoue, H.; Gyenis, A.; Krizan, J. W.; Yazdani, A.; Zhu, Y.; Cava, R. J. *Proceedings of the National Academy of Sciences* **2015**, 112, (11), E1174-E1180.
26. Dordevic, S. V.; Basov, D. N.; Dynes, R. C.; Ruzicka, B.; Vescoli, V.; Degiorgi, L.; Berger, H.; Gaál, R.; Forró, L.; Bucher, E. *Eur. Phys. J. B* **2003**, 33, (1), 15-23.
27. Lee, H. N. S.; Garcia, M.; McKinzie, H.; Wold, A. *J. Solid State Chem.* **1970**, 1, (2), 190-194.
28. Di Salvo, F. J.; Maines, R. G.; Waszczak, J. V.; Schwall, R. E. *Solid State Commun.* **1974**, 14, (6), 497-501.

29. Moncton, D. E.; Axe, J. D.; Disalvo, F. J. *Phys. Rev. Lett.* **1975**, 34, (12), 734-737.
30. Yan, Z.; Jiang, C.; Pope, T. R.; Tsang, C. F.; Stickney, J. L.; Goli, P.; Renteria, J.; Salguero, T. T.; Balandin, A. A. *J. Appl. Phys.* **2013**, 114, (20), 204301.
31. Renteria, J.; Samnakay, R.; Jiang, C.; Pope, T. R.; Goli, P.; Yan, Z.; Wickramaratne, D.; Salguero, T. T.; Khitun, A. G.; Lake, R. K.; Balandin, A. A. *J. Appl. Phys.* **2014**, 115, (3), 034305.
32. Neal, A. T.; Du, Y.; Liu, H.; Ye, P. D. *ACS Nano* **2014**, 8, (9), 9137-9142.
33. Kanno, T.; Matsumoto, T.; Ichimura, K.; Matsuura, T.; Tanda, S. *Physica B: Condensed Matter* **2015**, 460, (0), 165-167.
34. Morosan, E.; Zandbergen, H. W.; Li, L.; Lee, M.; Checkelsky, J. G.; Heinrich, M.; Siegrist, T.; Ong, N. P.; Cava, R. J. *Physical Review B* **2007**, 75, (10), 104401.
35. Gruner, G. *Reviews of Modern Physics* **1988**, 60, (4), 1129-1182.
36. Lee, P. A.; Rice, T. M. *Physical Review B* **1979**, 19, (8), 3970-3980.
37. Samnakay, R.; Wickramaratne, D.; Pope, T. R.; Lake, R. K.; Salguero, T. T.; Balandin, A. A. *Nano Lett.* **2015**.
38. Chu, C. W.; Testardi, L. R.; Di Salvo, F. J.; Moncton, D. E. *Physical Review B* **1976**, 14, (2), 464-467.
39. Goli, P.; Khan, J.; Wickramaratne, D.; Lake, R. K.; Balandin, A. A. *Nano Lett.* **2012**, 12, (11), 5941-5.
40. Monceau, P. *Advances in Physics* **2012**, 61, (4), 325-581.
41. Yang, J.; Wang, W.; Liu, Y.; Du, H.; Ning, W.; Zheng, G.; Jin, C.; Han, Y.; Wang, N.; Yang, Z.; Tian, M.; Zhang, Y. *Appl. Phys. Lett.* **2014**, 105, (6), 063109.

42. Yoshida, M.; Zhang, Y.; Ye, J.; Suzuki, R.; Imai, Y.; Kimura, S.; Fujiwara, A.; Iwasa, Y. *Sci. Rep.* **2014**, 4.
43. Yu, Y.; Yang, F.; Lu, X. F.; Yan, Y. J.; ChoYong, H.; Ma, L.; Niu, X.; Kim, S.; Son, Y.-W.; Feng, D.; Li, S.; Cheong, S.-W.; Chen, X. H.; Zhang, Y. *Nat Nano* **2015**, 10, (3), 270-276.
44. Monney, C.; Battaglia, C.; Cercellier, H.; Aebi, P.; Beck, H. *Phys. Rev. Lett.* **2011**, 106, (10), 106404.
45. Bovet, M.; Popović, D.; Clerc, F.; Koitzsch, C.; Probst, U.; Bucher, E.; Berger, H.; Naumović, D.; Aebi, P. *Physical Review B* **2004**, 69, (12), 125117.
46. Arguello, C. J.; Chockalingam, S. P.; Rosenthal, E. P.; Zhao, L.; Gutiérrez, C.; Kang, J. H.; Chung, W. C.; Fernandes, R. M.; Jia, S.; Millis, A. J.; Cava, R. J.; Pasupathy, A. N. *Physical Review B* **2014**, 89, (23), 235115.
47. Hajiyev, P.; Cong, C.; Qiu, C.; Yu, T. *Sci. Rep.* **2013**, 3.
48. Sugai, S.; Murase, K. *Physical Review B* **1982**, 25, (4), 2418-2427.
49. Steigmeier, E. F.; Harbeke, G.; Auderset, H.; DiSalvo, F. J. *Solid State Commun.* **1976**, 20, (7), 667-671.
50. Holy, J.; Klein, M.; McMillan, W.; Meyer, S. *Phys. Rev. Lett.* **1976**, 37, (17), 1145-1148.
51. Tsang, J.; Smith, J.; Shafer, M.; Meyer, S. *Physical Review B* **1977**, 16, (10), 4239-4245.
52. Stephenson, T.; Li, Z.; Olsen, B.; Mitlin, D. *Energy & Environmental Science* **2014**, 7, (1), 209-231.
53. Ambrosi, A.; Sofer, Z.; Pumera, M. *Small* **2015**, 11, (5), 605-612.
54. Zheng, J.; Zhang, H.; Dong, S.; Liu, Y.; Tai Nai, C.; Suk Shin, H.; Young Jeong, H.; Liu, B.; Ping Loh, K. *Nat Commun* **2014**, 5.
55. Sharma, S.; Auluck, S.; Khan, M. A. *Pramana - J Phys* **2000**, 54, (3), 431-440.

56. *Preparation and crystal growth of materials with layered structures*. D. Reidel Publishing Company: Dordrecht, Holland, 1977; Vol. 1, p 280.
57. Revelli Jr, J. F.; Phillips, W. A. *J. Solid State Chem.* **1974**, 9, (2), 176–186.
58. Yan, Y.; Xia, B.; Ge, X.; Liu, Z.; Wang, J.-Y.; Wang, X. *ACS Applied Materials & Interfaces* **2013**, 5, (24), 12794-12798.
59. Huisman, R.; Jellinek, F. *Journal of the Less Common Metals* **1969**, 17, (1), 111-117.
60. Lavik, M. T.; Medved, T. M.; Moore, G. D. *A S L E Transactions* **1968**, 11, (1), 44–55.
61. Joseph, C.; Bourson, P.; Fontana, M. D. *Journal of Raman Spectroscopy* **2012**, 43, (8), 1146-1150.
62. Py, M. A.; Haering, R. R. *Can. J. Phys.* **1983**, 61, (1), 76-84.
63. Ganal, P.; Olberding, W.; Butz, T.; Ouvrard, G. *Solid State Ionics* **1993**, 59, (3–4), 313-319.
64. Chhowalla, M.; Shin, H. S.; Eda, G.; Li, L.-J.; Loh, K. P.; Zhang, H. *Nat Chem* **2013**, 5, (4), 263-275.
65. Coleman, J. N.; Lotya, M.; O'Neill, A.; Bergin, S. D.; King, P. J.; Khan, U.; Young, K.; Gaucher, A.; De, S.; Smith, R. J.; Shvets, I. V.; Arora, S. K.; Stanton, G.; Kim, H.-Y.; Lee, K.; Kim, G. T.; Duesberg, G. S.; Hallam, T.; Boland, J. J.; Wang, J. J.; Donegan, J. F.; Grunlan, J. C.; Moriarty, G.; Shmeliov, A.; Nicholls, R. J.; Perkins, J. M.; Grieveson, E. M.; Theuwissen, K.; McComb, D. W.; Nellist, P. D.; Nicolosi, V. *Science* **2011**, 331, (6017), 568-571.
66. Smith, R. J.; King, P. J.; Lotya, M.; Wirtz, C.; Khan, U.; De, S.; O'Neill, A.; Duesberg, G. S.; Grunlan, J. C.; Moriarty, G.; Chen, J.; Wang, J. Z.; Minett, A. I.; Nicolosi, V.; Coleman, J. N. *Adv. Mater.* **2011**, 23, (34), 3944-+.

67. Cunningham, G.; Lotya, M.; Cucinotta, C. S.; Sanvito, S.; Bergin, S. D.; Menzel, R.; Shaffer, M. S. P.; Coleman, J. N. *ACS Nano* **2012**, 6, (4), 3468-3480.
68. Rossnagel, K.; Smith, N. V. *Physical Review B* **2007**, 76, (7).
69. Ogawa, N.; Miyano, K. *Physical Review B* **2004**, 70, (7).

## CHAPTER 5

### CONCLUSIONS

#### Conclusions

Nanosheets have high surface area, which can be exploited to enhance catalysis through the presence of additional surface sites.<sup>1</sup> Moreover, nanosheets can have interesting thickness-dependent properties that are sometimes different than that of the bulk form of the material. Quantum confinement effects, generated by the confinement of excitons to two dimensions, leads to interesting electron phenomena, such as increased photoluminescence, metallic/insulating on/off switching, ultrahigh current density, and temperature-dependent conductivity.<sup>2-6</sup>

Metal oxides are one such class of materials with interesting nanoscale properties. These materials are catalysts for the photodegradation of organic pollutants, such as chloroform, acetaldehyde, and rhodamine B.<sup>7-9</sup> Nanoscale structuring of such photocatalytic materials has been shown to enhance the photocatalytic activity.<sup>1, 10, 11</sup> For example, the photodegradation of Rhodamine B by nanoscale  $\text{Bi}_2\text{WO}_6$  is 8–10 times higher than photodegradation by bulk  $\text{Bi}_2\text{WO}_6$ .<sup>12</sup> In addition to catalytic properties, some metal oxides also have interesting electronic properties, such as piezoelectricity, and can be used as dielectric materials in capacitors.<sup>13</sup>

Bismuth tungstate ( $\text{Bi}_2\text{WO}_6$ ) is a high-temperature ferroelectric metal oxide suitable for high-temperature piezoelectric applications that displays spontaneous polarization and has a high electromechanical coupling coefficient.<sup>14, 15</sup>  $\text{Bi}_2\text{WO}_6$  crystals also displayed interesting reversible chromism effects after both UV irradiation in specific solvents and upon lithium ion

intercalation.<sup>16</sup> Nanostructured  $\text{Bi}_2\text{WO}_6$  can be attained by hydrothermal conditions; however, three-dimensional flower-like morphologies are typically achieved.<sup>10, 17</sup> Therefore, we set out to form  $\text{Bi}_2\text{WO}_6$  with a nanosheet morphology through the use of a lateral template precursor. Chapters II and III discussed the synthesis of  $\text{Bi}_2\text{WO}_6$  nanosheets.

In Chapter II,  $\text{Bi}_2\text{WO}_6$  nanosheets were formed under hydrothermal conditions using a  $\text{Cs}_4\text{W}_{11}\text{O}_{36}^{2-}$  nanosheet precursor as both the tungsten oxide source and as a lateral template.<sup>16</sup> The hydrothermal reaction was monitored by powder X-ray diffraction. During the first hour of hydrothermal synthesis, two bismuth oxide intermediates were formed:  $[\text{Bi}_6\text{O}_5(\text{OH})_3](\text{NO}_3)_5 \cdot 3\text{H}_2\text{O}$  and  $[\text{Bi}_6\text{O}_6(\text{OH})_3](\text{NO}_3)_3 \cdot 1.5\text{H}_2\text{O}$ . After two hours,  $\text{Bi}_2\text{WO}_6$  nanosheets began to form. The reaction was complete after five hours. Powder X-ray diffraction, Raman spectroscopy, scanning electron microscopy, and atomic force microscopy were used to characterize the product and confirm that  $\text{Bi}_2\text{WO}_6$  nanosheets were formed. The  $\text{Bi}_2\text{WO}_6$  nanosheets had lateral dimensions of 1–2  $\mu\text{m}$  and thicknesses of 5–15 nm. The optical bandgap of the  $\text{Bi}_2\text{WO}_6$  nanosheets was measured by UV-vis diffuse reflectance to be  $\sim 3.1$  eV, which is consistent with the bandgap of other  $\text{Bi}_2\text{WO}_6$  nanostructures reported previously.<sup>18, 19</sup> We also showed that  $\text{Bi}_2\text{WO}_6$  nanosheets showed photochromism effects from UV irradiation and chromism effects due to lithium intercalation. Overall, hydrothermal synthesis using a  $\text{Cs}_4\text{W}_{11}\text{O}_{36}^{2-}$  nanosheet precursor as a lateral template was found to be an effective method for the preparation of large, isolable  $\text{Bi}_2\text{WO}_6$  nanosheets.

Chapter III also discusses the hydrothermal synthesis of  $\text{Bi}_2\text{WO}_6$  nanosheets. In this case further elucidation of the templating effect was accomplished by using a  $\text{Bi}_2\text{O}_2[\text{BO}_2(\text{OH})]$  nanosheet precursor as the bismuth oxide source alongside the  $\text{Cs}_4\text{W}_{11}\text{O}_{36}^{2-}$  nanosheet lateral template used in Chapter II.  $\text{Bi}_2\text{O}_2[\text{BO}_2(\text{OH})]$  is a relatively new material, first synthesized in 2011,

and can be formed by hydrothermal synthesis using  $\text{H}_3\text{BO}_3$  and  $\text{Bi}(\text{NO}_3)_3$ .<sup>20-22</sup> However, we found it necessary to alter the previously reported procedures in order to produce a homogenous nanosheet product. Thus, the pH of the reaction solution and the stoichiometric ratio of  $\text{H}_3\text{BO}_3$  to  $\text{Bi}_3(\text{NO}_3)_3$  were optimized at 8 and 4:1, respectively, to produce pure  $\text{Bi}_2\text{O}_2[\text{BO}_2(\text{OH})]$  nanosheets with lateral dimensions in the micrometer range and thicknesses of 5–40 nm. If other pH values were used, altogether different bismuth oxide products were produced. If the stoichiometric ratio was altered, different morphologies of  $\text{Bi}_2\text{O}_2[\text{BO}_2(\text{OH})]$  were produced. Further studies were carried out to test the templating effect of  $\text{Bi}_2\text{O}_2[\text{BO}_2(\text{OH})]$  nanosheets.  $\text{Bi}_2\text{O}_2[\text{BO}_2(\text{OH})]$  nanosheets were reacted hydrothermally with  $\text{Na}_2\text{WO}_6$ , a soluble tungsten oxide precursor used in place of the  $\text{Cs}_4\text{W}_{11}\text{O}_{36}^{2-}$  nanosheet precursor, which produced aggregates of platelets that were multiple micrometers in lateral dimension and hundreds of nanometers in thickness. The platelet aggregates are distinct from the flower-like aggregates that are formed from the reaction with two soluble precursors. The reaction of  $\text{Bi}_2\text{O}_2[\text{BO}_2(\text{OH})]$  nanosheets with the same  $\text{Cs}_4\text{W}_{11}\text{O}_{36}^{2-}$  nanosheets used in Chapter II formed  $\text{Bi}_2\text{WO}_6$  nanosheets with lateral dimensions in the micrometer range and thicknesses of 5–40 nm. With this work, we affirm that  $\text{Cs}_4\text{W}_{11}\text{O}_{36}^{2-}$  nanosheet templating through hydrothermal synthesis is the most important factor in the preparation of isolated  $\text{Bi}_2\text{WO}_6$  nanosheets.

Another noteworthy material in nanosheet form is transition metal dichalcogenides, which have the general formula  $\text{MX}_2$  where M is a transition metal and X is a chalcogenide. These materials are layered structures where the neighboring  $\text{MX}_2$  layers are held together by van der Waals forces. Delamination or exfoliation can overcome these weak interactions easily to produce isolable nanosheets, which range from a single monolayer to several monolayers thick.

Transition metal dichalcogenides can be synthesized in bulk through high temperature reactions between elemental precursors.<sup>23,24</sup> The bulk crystals can then be formed into millimeter-sized crystals, suitable for exfoliation into nanosheets, through the use of chemical vapor transport (CVT).<sup>25,26</sup> Nanosheets are then obtained by a variety of methods. Most notably are the Scotch tape method and chemical exfoliation,<sup>27-30</sup> where exfoliation can be achieved by intercalating small molecules such as organolithium compounds or through sonication in a coordinating solvent.<sup>28,30</sup> Sonication in a coordinating solvent produces very thin sheets with lateral dimensions reaching several hundred nanometers and does not alter the material's polytype.<sup>30</sup> It is important that the original polytype is retained because different polytypes can have different electrical properties.<sup>31</sup>

Chapter IV discusses transition metal dichalcogenides, with a special focus on tantalum diselenide ( $\text{TaSe}_2$ ). The three different polytypes of  $\text{TaSe}_2$  are discussed, with details on how to obtain each polytype. Large, pristine crystals of  $\text{TaSe}_2$  were grown using CVT with an  $\text{I}_2$  transport agent. The growth temperature and speed at which the reaction is cooled determines the polytype that is formed. Rapidly quenching from growth temperatures of  $>900$  °C produces  $1T$ - $\text{TaSe}_2$ , which is primarily a high temperature polytype. Rapid quenching from lower growth temperatures (500–850 °C) results in  $3R$ - $\text{TaSe}_2$  with a small amount of  $2H$ - $\text{TaSe}_2$ . A slow cooling rate after transport forms  $2H$ - $\text{TaSe}_2$ . In addition, an excessive amount of  $\text{I}_2$  transport agent was found to lead to the formation of iodine-doped  $\text{TaSe}_2$  crystals on the crystal step edges.

We also studied the oxidation of bulk crystals exposed to both ambient conditions and elevated temperature. Heating  $1T$ - $\text{TaSe}_2$  crystals at 300 °C for an hour produced tantalum oxide ( $\text{Ta}_2\text{O}_5$ ) on the surface of the crystals. However, six hours of heating the crystals at 200 °C led to oxidation on the surface and edge sites.  $3R,2H$ - $\text{TaSe}_2$  crystals were also susceptible to oxidation when heated at elevated temperatures in air. After six hours of heating at 200 °C, surface oxidation

was observed at edge and defect sites. Nevertheless, for all polytypes, any oxides on the surface can be removed by delaminating the top layer of the crystal using the Scotch tape method,<sup>32</sup> which indicates that oxidation does not penetrate through the crystal and only resides on the surface. Interestingly, when  $1T$ -TaSe<sub>2</sub> crystals are stored under ambient conditions for several months, the surface layers transform to the  $2H$ -TaSe<sub>2</sub> polytype. Again, this transformation was restricted to the surface, and thus can be removed to expose the  $1T$ -TaSe<sub>2</sub> polytype in the crystal interior.

Methods of exfoliation of TaSe<sub>2</sub> crystals into nanosheets were also discussed. Of particular interest is the solution exfoliation method developed by Coleman et al.<sup>30</sup> In our modified version of the Coleman method, bulk TaSe<sub>2</sub> crystals were dispersed in a coordination solvent, typically *N*-methylpyrrolidone or *N*-vinylpyrrolidone, then probe ultrasonicated for an hour to exfoliate the bulk material into nanosheets. The nanosheets produced by this method have nanometer thicknesses with lateral dimensions in the hundreds of nanometers.

After optimizing the synthesis of different polytypes of TaSe<sub>2</sub>, samples were sent to collaborators at the University of California, Riverside, to study the properties of TaSe<sub>2</sub> nanosheets and create electronic devices for fundamental studies of the nanosheets. Yan et al. used Raman spectroscopy as a metrology tool to easily measure the film thickness, as well as determining the crystal polytype.<sup>32</sup> Samnakay et al. showed that Raman spectroscopy can also be used to determine the commensurate to incommensurate charge density wave transition in  $1T$ -TaSe<sub>2</sub>, which was 473 K for a 150 nm thick film and 413 K for a 35 nm thick film.<sup>33</sup> Finally, Renteria et al. fabricated an all-metallic field-effect transistor from  $2H$ -TaSe<sub>2</sub>, which showed an ability for metallic/insulating on/off switching voltage that was dependent on both the channel size and presence of light.<sup>26</sup>

The work presented in this dissertation has shown that nanosheets with interesting properties can be easily obtained using bottom up and top down approaches. The formation of

bismuth metal oxide nanosheets requires a bottom up approach, directly forming large, free-standing nanosheets through scalable and relatively low temperature hydrothermal syntheses. Transition metal dichalcogenides, specifically TaSe<sub>2</sub> in this dissertation, employ a top down approach, beginning with pristine bulk crystals and exfoliating the material into free-standing nanosheets. By using known methods as well as developing new routes to form such materials on the two dimensional scale, the unique electrical properties of nanosheets can be further explored.

## References

1. Zhang, L.; Zhu, Y. *Catalysis Science & Technology* **2012**, 2, (4), 694-706.
2. Mak, K. F.; Lee, C.; Hone, J.; Shan, J.; Heinz, T. F. *Phys. Rev. Lett.* **2010**, 105, 136805.
3. Splendiani, A.; Sun, L.; Zhang, Y.; Li, T.; Kim, J.; Chim, C.-Y.; Galli, G.; Wang, F. *Nano Lett.* **2010**, 10, (4), 1271-1275.
4. Radisavljevic, B.; Radenovic, A.; Brivio, J.; Giacometti, V.; Kis, A. *Nature Nanotechnology* **2011**, 6, (3), 147-150.
5. Lembke, D.; Kis, A. *ACS Nano* **2012**, 6, 10070.
6. Radisavljevic, B.; Kis, A. *Nat. Mater.* **2013**, 12, 815.
7. Tang, J.; Zou, Z.; Ye, J. *Catal. Lett.* **2004**, 92, (1), 53-56.
8. Fu, H.; Pan, C.; Yao, W.; Zhu, Y. *J. Phys. Chem. B* **2005**, 109, (47), 22432-22439.
9. Zhang, L.; Wang, H.; Chen, Z.; Wong, P. K.; Liu, J. *Applied Catalysis B: Environmental* **2011**, 106, (1-2), 1-13.
10. Zhang, L.; Wang, W.; Chen, Z.; Zhou, L.; Xu, H.; Zhu, W. *J. Mater. Chem.* **2007**, 17, (24), 2526-2532.
11. Zhang, C.; Zhu, Y. *Chem. Mater.* **2005**, 17, (13), 3537-3545.
12. Shang, M.; Wang, W.; Sun, S.; Zhou, L.; Zhang, L. *Journal of Physical Chemistry C* **2008**, 112, (28), 10407-10411.
13. Shi, Z. Q.; Jia, Q. X.; Anderson, W. A. *J. Electron. Mater.* **1991**, 20, (11), 939-944.
14. Noguchi, Y.; Miyayama, M., Defect Control and Properties in Bismuth Layer Structured Ferroelectric Single Crystals. In *Lead-Free Piezoelectrics*, Priya, S.; Nahm, S., Eds. Springer New York: 2012; pp 405-459.

15. Yoneda, Y.; Kohara, S.; Takeda, H.; Tsurumi, T. *Japanese Journal of Applied Physics* **2012**, 51, 09LE06.
16. Pope, T. R.; Lassig, M. N.; Neher, G.; Weimar III, R. D.; Salguero, T. T. *Journal of Materials Chemistry C* **2014**, 2, (17), 3223.
17. Xia, J.; Li, H.; Luo, Z.; Xu, H.; Wang, K.; Yin, S.; Yan, Y. *Mater. Chem. Phys.* **2010**, 121, (1–2), 6-9.
18. Xu, C.; Wei, X.; Guo, Y.; Wu, H.; Ren, Z.; Xu, G.; Shen, G.; Han, G. *Mater. Res. Bull.* **2009**, 44, (8), 1635-1641.
19. Zhou, Y.; Antonova, E.; Bensch, W.; Patzke, G. R. *Nanoscale* **2010**, 2, (11), 2412-7.
20. Cong, R.; Sun, J.; Yang, T.; Li, M.; Liao, F.; Wang, Y.; Lin, J. *Inorg. Chem.* **2011**, 50, (11), 5098-5104.
21. Zhang, R.; Dai, Y.; Lou, Z.; Li, Z.; Wang, Z.; Yang, Y.; Qin, X.; Zhang, X.; Huang, B. *CrystEngComm* **2014**, 16, (23), 4931.
22. Huang, H.; He, Y.; Lin, Z.; Kang, L.; Zhang, Y. *The Journal of Physical Chemistry C* **2013**, 117, (44), 22986-22994.
23. *Preparation and crystal growth of materials with layered structures*. D. Reidel Publishing Company: Dordrecht, Holland, 1977; Vol. 1, p 280.
24. Revelli Jr, J. F.; Phillips, W. A. *J. Solid State Chem.* **1974**, 9, (2), 176–186.
25. Yan, Y.; Xia, B.; Ge, X.; Liu, Z.; Wang, J.-Y.; Wang, X. *ACS Applied Materials & Interfaces* **2013**, 5, (24), 12794-12798.
26. Renteria, J.; Samnakay, R.; Jiang, C.; Pope, T. R.; Goli, P.; Yan, Z.; Wickramaratne, D.; Salguero, T. T.; Khitun, A. G.; Lake, R. K.; Balandin, A. A. *J. Appl. Phys.* **2014**, 115, (3), 034305.

27. Novoselov, K. S.; Jiang, D.; Schedin, F.; Booth, T. J.; Khotkevich, V. V.; Morozov, S. V.; Geim, A. K. *Proc. Natl. Acad. Sci. U.S.A.* **2005**, 102, 10451.
28. Ambrosi, A.; Sofer, Z.; Pumera, M. *Small* **2015**, 11, (5), 605-612.
29. Zheng, J.; Zhang, H.; Dong, S.; Liu, Y.; Tai Nai, C.; Suk Shin, H.; Young Jeong, H.; Liu, B.; Ping Loh, K. *Nat Commun* **2014**, 5.
30. Coleman, J. N.; Lotya, M.; O'Neill, A.; Bergin, S. D.; King, P. J.; Khan, U.; Young, K.; Gaucher, A.; De, S.; Smith, R. J.; Shvets, I. V.; Arora, S. K.; Stanton, G.; Kim, H.-Y.; Lee, K.; Kim, G. T.; Duesberg, G. S.; Hallam, T.; Boland, J. J.; Wang, J. J.; Donegan, J. F.; Grunlan, J. C.; Moriarty, G.; Shmeliov, A.; Nicholls, R. J.; Perkins, J. M.; Grieveson, E. M.; Theuwissen, K.; McComb, D. W.; Nellist, P. D.; Nicolosi, V. *Science* **2011**, 331, (6017), 568-571.
31. Chhowalla, M.; Shin, H. S.; Eda, G.; Li, L.-J.; Loh, K. P.; Zhang, H. *Nat Chem* **2013**, 5, (4), 263-275.
32. Yan, Z.; Jiang, C.; Pope, T. R.; Tsang, C. F.; Stickney, J. L.; Goli, P.; Renteria, J.; Salguero, T. T.; Balandin, A. A. *J. Appl. Phys.* **2013**, 114, (20), 204301.
33. Samnakay, R.; Wickramaratne, D.; Pope, T. R.; Lake, R. K.; Salguero, T. T.; Balandin, A. A. *Nano Lett.* **2015**.